NASA Contractor Report 165908

NASA-CR-165908
19830007777

Investigation of Multilayer Magnetic Domain Lattice File

E. J. Torok, M. Kamin, C. H. Tolman

SPERRY UNIVAC CORPORATION
St. Paul, MN 55165

CONTRACT NAS1-15007
AUGUST 1982

National Aeronautics and
Space Administration

Langley Research Center
Hampton, Virginia 23665

NASA Contractor Report 165908

Investigation of Multilayer Magnetic Domain Lattice File

E. J. Torok, M. Kamin, C. H. Tolman

SPERRY UNIVAC CORPORATION
St. Paul, MN 55165

CONTRACT NAS1-15007
AUGUST 1982

National Aeronautics and
Space Administration

Langley Research Center
Hampton, Virginia 23665

CONTENTS

1. Introduction

1.1 Justification and Requirements

Magnetic bubble technology is essentially capable of higher bit densities than is currently available. The resolution of lithography employed for circuit fabrication limits the devices presently in use. A variety of modified technologies have been studied which would relax the lithographic resolution requirements, such as semi-disks, contiguous disks, and bubble lattices. In a multilayer self-structured bubble design, domain structures in one layer replace all or part of the control circuitry for the data bubbles in a second layer. This design reduces the technology restrictions imposed by the lithographic process, thereby allowing the full capability of the magnetic material to be utilized.

1.2 Multilayer Structures

Multilayered garnet structures offer a new degree of freedom, which promises to eliminate many problems assoicated with present-day devices. These structures, by allowing tailoring of the material properties of two or more layers, can optimize the parameters of each layer to serve a specific function. A periodic domain configuration can be generated in one layer and used to structure the data in a second layer. This implies that all structuring circuitry can conceivably be removed from the storage area. As the memory chip becomes larger, the reduction of circuit complexity becomes dramatic if the storage area circuitry is eliminated. Stable periodic domain configurations can be made to propagate coherently, thereby propagating bubbles in a data layer. This use of periodic domain configurations allow bubbles to move in a potential well of nearly constant depth, thereby improving device operating margins and upper frequency limitations. The use of natural garnet magnetic domain phenomena in place of lithographically configured features for structuring and propagating implies higher yields and lower costs for these devices.

1.3 Purpose of Report

This report describes the research leading to a practical multilayer self-structured memory device concept. Initially, the reasoning is presented leading to device selection. The theory of various concepts is described next, followed by experimental investigations of several current accessed circuits. Subsequently, the test vehicle design and evaluation are reported, in addition to a recommended memory storage area configuration.

2. Multilayer Self-Structured Lattice File

2.1 Definition

Multilayered self-structured lattice files have two or more coupled magnetic garnets grown on a common substrate. One layer, referred to as the data layer, supports data bubbles. One or more garnet layers, the carrier layers, contain arrays of stripe domains or bubble domains, and also determine the position of bubbles in the data layer. Propagation of the data is accomplished by moving the domain arrays in the carrier layers. Structuring can be accomplished by employing confinement rails or channels in the garnet, and/or a lattice of carrier bubbles.

Through incorporation of self-structured multilayer designs, the goals are to greatly reduce the total number of propagating elements, and to make the minimum feature size of the propagating elements consistent with conventional photolithography, while maintaining high bit density.

2.2 Matrix of Possible Multilayer Structures

A list of self-structured multilayer bubble file designs was prepared for device consideration. This list is most easily represented in a five dimensional matrix, figure 2.1, because there are five different independent characteristics for classification. These are (1) the type of carrier used to convey the data bubbles (e.g., stripe carrier, wavy wall carrier, or bubble carrier), (2) the means by which the carrier is propelled (e.g., T-bars, etc.), (3) the type of fences or guidance channels, (4) the type of coupling between carrier film and the data film (e.g., exchange, etc.) and (5) the type of bias field used. The total number of combinations is 540. This is too large to be represented in a two dimensional matrix. A reduced two dimensional matrix has been constructed, figure 2.2, and contains only 120 items. The different methods of bias are not represented on this list for simplicity, because for most structures the bias type will be determined by the requirements of bubble stability and stripe stability, and therefore, there will be little freedom of choice.

2.3 Design Feature Evaluation

The two dimensional matrix of figure 2.2 still contains too many candidates to be experimentally evaluated for a self-structured multilayer memory system. The candidates in each of the sections for carrier type, means of propulsion, and coupling type must be individually evaluated, and objective decisions made whether they are a viable technology for device application.

CARRIER	PROPULSION	FENCES OR GUIDANCE CHANNELS	COUPLING	BIAS
BUBBLE	ANGEL-FISH	PERMALLOY	EXCHANGE	EXTERNAL
	AUTOMOTION	ION IMPLANTED		
		ETCHED GROOVE	EXCHANGE TYPE II	
STRIPE CARRIER	ROTATING IN-PLANE FIELD (T-BARS etc.			SELF-BIASED
		MAGNETIC DOMAIN FENCE	MAGNETO-STATIC	
WAVY WALL-CARRIER	CONDUCTOR PROPELLED	NO FENCE		MIXED

FIGURE 2.1. MATRIX OF POSSIBLE MULTILAYER STRUCTURES

		Bubble Carrier				Stripe Carrier				Wavy Wall Carrier			
		Anglefish	Rotating Field	Automotion	Conductor Accessed	Anglefish	Rotating Field	Automotion	Conductor Accessed	Anglefish	Rotating Field	Automotion	Conductor Accessed
Exchange Coupling Type I or Type II	NiFe Fence												
	Ion Implanted Fence												
	Etched Groove												
	Magnetic Domain Fence												
	No Fence												
Magnetostatic Coupling	NiFe Fence												
	Ion Implanted Fence												
	Etched Groove												
	Magnetic Domain Fence												
	No Fence												

Figure 2.2 Reduced Matrix of Possible Multilayer Structures.

The wavy wall application for carrier propagation does not appear to be a serious candidate. Since its description in the literature, there has been very little interest or work throughout the industry associated with its development or application. The bubble carrier and the stripe carrier remain as excellent candidates.

Angelfish and T-bar type propagators place strigent requirements on the photo-lightography processing of devices. Since successful propagation of bubbles requires a complete array of propagation features, this limits both the element density and device yield. Control of stripe or bubble propagation by automation proved to be most difficult because of irregular displacement.

Conventional bubble memories employ a rotating magnetic field for access purposes, generated by externally mounted field coils. Field access requires the excitation of a large volume of the memory, requiring high voltage at the coils, and results in a system penalty for power. The memory operating frequency is limited by the inductance of the coils, which require excessive power at high drive frequencies. These coils also represent a significant fraction of the total weight and total cost of the memory. Through incorporation of current accessed techniques, the coils can be eliminated.

Table 2.1 lists the advantages and disadvantages of a current accessed bubble memory, as compared to a field accessed memory. For these reasons, an effort has been placed in investigating current accessed techniques for domain propagation.

Exchange coupling between multiple layers of magnetic material generally requires intimate contact of these layers for adequate interaction. Variation of the coupling strength can be accomplished with very thin non-magnetic intermediate layers, but the results are very difficult to control accurately. Magnetostatic coupling between layers appears as a suitable candidate, since its magnitude can be controlled quite easily by geometrical considerations.

Structuring of the memory design can be accomplished in one of the two directions by providing an energy barrier to the bubble or stripe domains. Barriers such as a magnetic rail on the garnet surface, an ion implanted region of the garnet, or a groove etched in the garnet will provide an energy well to restrict domain location. All three of these barriers appear to be acceptable candidates, and their specific application will depend on the individual circuit requirements and physical layout. A magnetic domain fence is less desirable, since it is not a permanent feature of the device, and can contribute to device failure if eradicated.

TABLE 2.1 CURRENT ACCESSED BUBBLE MEMORY FEATURES

		Advantage	Disadvantage
1.	current access	x	
2.	large propagation features	x	
3.	multilayer construction		x
4.	self-structured	x	
5.	coherent propagation	x	
6.	high density	x	
7.	high frequency operation	x	
8.	propagation circuitry connections		x
9.	no wall state storage	x	
10.	medium Q materials	x	
11.	heat generated by current lines		x
12.	low access time	x	

The number of combinations that are serious candidates for the multilayer self-structured memory design has, therefore, been reduced to six. Current access; bubble or stripe carrier propagation; and barriers of magnetic rails, ion implanted areas, or an etched groove are the salient design features.

2.4 Device Design

Based on the above reasoning, a theoretical and experimental effort was initiated on a self-structured memory device. The design consisted of a multiple layer garnet with the magnetic layers coupled by magnetostatic interaction, magnetically-assisted current accessed stripe domain propagators, current accessed bubble and stripe domain generators, and magnetic bars for stripe domain end pinning. Propagation of bubbles in the data layer is controlled by current accessed domain propagation in the carrier layer. Detection and readout of data were not necessarily included in the device design.

3. Theoretical Investigations

3.1 Objectives

The behavior of bubble domains and stripe domains in single layer garnet materials, and their interaction in multiple layer garnet materials, depends upon many geometrical and material properties. It is the object of the following theoretical investigations to describe these interactions and couplings, and to employ the results in selecting device designs for development of a multilayer lattice file. These calculations, and the resultant formulas, allow prediction of bubble and stripe behavior before fabrication of test circuits.

3.2 Coupling Between Multiple Layers of Bubble Domains

3.2.1 Interaction Between Bubbles in Adjacent Layers

Bubbles in different layers exert forces on each other. These forces are exerted by the stray field emanating from a bubble, which affects the bubbles in the adjacent layer in two ways; 1) it exerts a force tending to move the bubble directly over the center of the first bubble; and 2) it opposes the bias field and tends to increase the size of the bubble. To evaluate the interactions between bubbles, it is necessary to calculate this stray field. This can be done exactly[1] for both the radial component $H_r(r,z)$ and the normal component, $H_z(r,z)$. See Table 3.1 for symbol definition.

(3.1)

$$H_r(r,z) = \left\{ \frac{2}{\pi}\left(\frac{r_o}{r}\right)^{\frac{1}{2}} \left(\frac{(1 - \frac{1}{2}K_1^2)\,K(K_1) - E(K_1)}{K_1} \right) - \frac{(1 - \frac{1}{2}K_2^2)K(K_2) - E(K_2)}{K_2} \right\} 4\pi M$$

$$\frac{H_z(r,z)}{4\pi M} = - \frac{1}{2\pi r_o (r r_o)^{\frac{1}{2}}} [zK_1K(K_1) - (h + z)K_2K(K_2)] - \frac{\Lambda_o(\alpha_1,\beta_1) - \Lambda_o(\alpha_2,\beta_2)}{2r_o} \qquad \text{for } r < r_o$$

$$= - \frac{1}{2\pi r_o (r r_o)^{\frac{1}{2}}} [zK_1K(K_1) - (h + z)K_2K(K_2)] + \frac{\Lambda_o(\alpha_1,\beta_1) - \Lambda_o(\alpha_2,\beta_2)}{2r_o} \qquad \text{for } r > r_o$$

$$= -\frac{1}{2\pi r_o^2}\left[zK_1K(K_1) - (h+z)K_2K(K_2)\right] \quad \text{for } r = r_o$$

where $K(K)$, $E(K)$, and $\Lambda_o(\alpha,\beta)$ are the complete elliptic integrals of the first, second, and third kinds, respectively, with

$$K_1^2 = 4rr_o\left[z^2 + (r+r_o)^2\right]^{-1} \tag{3.2}$$

$$K_2^2 = 4rr_o\left[(h+z)^2 + (r+r_o)^2\right]^{-1}$$

$$\alpha_1 = \sin^{-1} K_1,$$

$$\alpha_2 = \sin^{-1} K_2,$$

$$\beta_1 = \sin^{-1}\left\{z\left[(h+z)^2 + (r-r_o)^2\right]^{-\frac{1}{2}}\right\}, \text{ and}$$

$$\beta_2 = \sin^{-1}\left\{(h+z)\left[(h+z)^2 + (r-r_o)^2\right]^{-\frac{1}{2}}\right\}$$

Equations 3.1 and 3.2 are plotted in Figures 3.1 and 3.2. Note that the field is a large fraction of $4\pi M$; the coupling field is more than enough to trap and move bubbles, which has been observed experimentally. Note also that the coupling field extends beyond the radius of the bubble when the spacing between layers is significant, so that the cluster of trapped bubbles can even extend somewhat beyond the outside a bubble. The coupling field is (1) larger for thicker bubbles, (2) larger for larger diameter bubbles, and (3) large when the distance from the bubble is small compared to the radius of the bubble. These three observations show that while the large bubble in the bottom layer has a large effect on the small bubbles in the upper layer, the bubbles in the upper layer have almost no effect on the large bubble. This simplifies the investigation considerably.

Table 3.1 presents a list of definition of symbols used in this section.

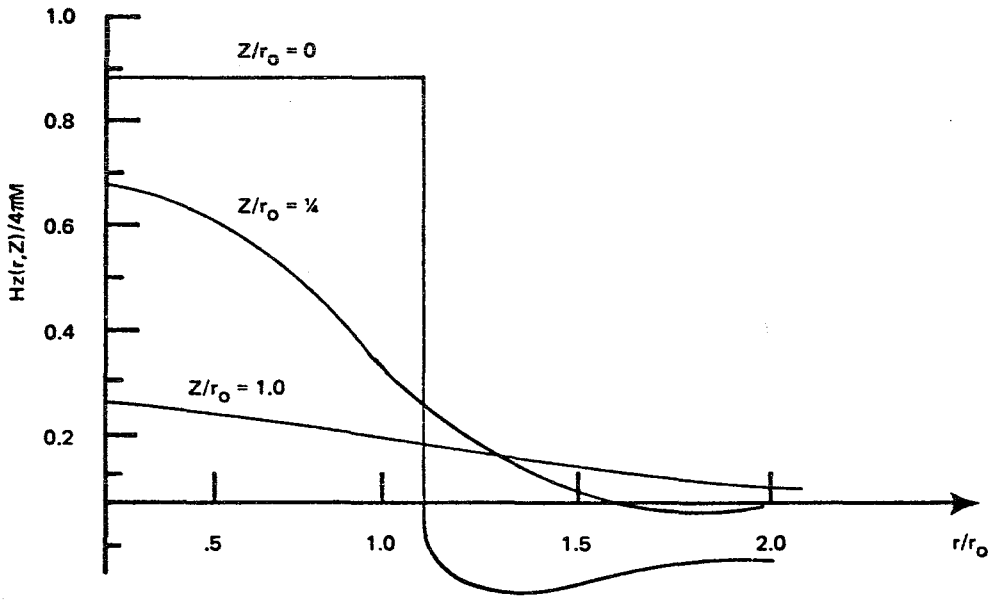

Figure 3.1 Radial Dependence of the Normal Field from a Bubble of Radius r_o and Thickness 2 r_o at Various Heights.

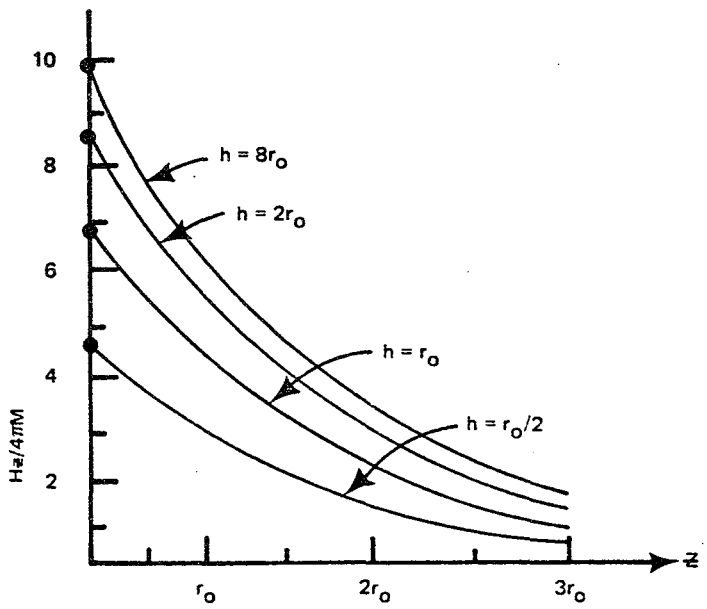

Figure 3.2 Normal Field from a Bubble as a Function of Height for Various Thicknesses.

TABLE 3.1. DEFINITIONS OF SYMBOLS

A	Exchange constant, ERG/CM
D	Width of an isolated stripe domain, m
H	Magnetic field normal to film surface, OE
$\hat{H}$	Normalized normal magnetic field, $H/4\pi M$
H_c	Coercive force, OE
H_k	Anisotropy field, 2K/M, OE $= (4\pi M\ell)^2 M/(2A)$
H_o	Bubble collapse field threshold, OE
$\hat{H}_o$	Normalized collapse field, $H_o/4\pi M$
H_{RO}	Run-out field threshold, or strip-out field threshold, OE
$\hat{H}_{RO}$	Normalized run-out field, $H_{RO}/4\pi M$
H_D	Stray field on the wall of an infinitely long isolated stripe, averaged over film thickness, OE
$\bar{H}_D$	Stray field on the wall of an infinitely long isolated stripe, averaged over film thickness and strip width, OE
$\bar{H}_{TIP}$	Stray field at the tip of a rectangular isolated stripe, averaged over film thickness and stripe width, OE
h	Film thickness, m
K	Uniaxial anistropy constant, $\frac{1}{2}MH_k$, ERG/CM^3
L	Length of an isolated stripe domain, m
ℓ	Characteristic length of garnet, $T_w/4\pi M^2$, m
λ	Normalized characteristic length, ℓ/h
M	Magnetic moment, EMU, GAUSS
r	Bubble domain radius, m
X	Normalized bubble domain radius, r/h
r_o	Bubble domain radius at collapse threshold, m
X_o	Normalized Bubble domain radius at collapse threshold, r_o/h
Q	Normalized anisotropy field, $H_k/4\pi M = K/2\pi M^2$
T_w	Wall energy per unit length and thickness $4\sqrt{AK}$, ERG/CM^2

3.2.2 Material Parameters for Multiple Layers of Bubbles

Multiple layers of bubble supporting materials provide increased flexibility in design considerations for self-structured applications. Listed below is a set of equations which relate the material parameters, bubble size, and various magnetic fields to each other.

(reference number)

$$X = \frac{1 - 3\lambda/4 - \mathcal{H}}{3\mathcal{H}} + \left[\left(\frac{1 - 3\lambda/4 - \mathcal{H}}{3\mathcal{H}}\right)^2 - \frac{\lambda}{3\mathcal{H}}\right]^{1/2} \quad (2) \quad (3.3)$$

$$\mathcal{H}_o = 1 + 3\lambda/4 - (3\lambda)^{1/2} \quad (2) \quad (3.4)$$

$$X_o = \left((3\lambda)^{1/2} - 3/2\right)^{-1} \quad (2) \quad (3.5)$$

$$\lambda = (4/3)\ (1 - 2\mathcal{H}_o^{1/2} + \mathcal{H}_o) \quad (3.6)$$

(Inversion of equation 3.4)

$$\mathcal{H}_{RO} = \exp -\ (1 + \pi\lambda - \mathcal{H}_{RO}) \quad (3) \quad (3.7)$$

$$\lambda = (\mathcal{H}_{RO} - \ln\mathcal{H}_{RO} - 1)/\pi \quad (3.8)$$

(Inversion of equation 3.7)

$$\ell = \left(\frac{106.7}{4\pi M}\right)^{1.231} = 313.8(4\pi M)^{-1.231} \quad (3.9)$$

Equation 3.9 is an empirical relation found to hold true for large and small bubble garnets, both Ga and CaGe garnets (see section 4.5.2). There may be garnets for which equation 3.9 is not true, but garnets can be found that fit equation 3.9 over the full range of ℓ and M.

In one type of multilayer self-structured bubble memory, a large diameter carrier bubble domain in one layer carries along with itself a number of small data bubbles in a second layer. Both the large bubbles and the small bubbles, in their own layer, must have wide operating regions that overlap. The run-out, or strip-out, field of one layer must not be higher than the collapse field of the other, and vice-versa. The following calculation

generates the proper parameters of the two layers so that the bubble sizes are different, yet the collapse field is the same.

As an example, consider the application of two magnetic layers with $4\pi M$ = 125 Oe and 300 Oe, with a bubble collapse threshold H_o = 83 Oe for both layers.

To convert Oersteds into ampere turns per meter, multiply by $1000/4\pi$, which equals 79.5775. What is the proper thickness, h, for each layer, and what are the values of ℓ, λ, X_o, r_o, H_{Ro}?

From equation 3.9, the characteristic length ℓ is 0.823μm for $4\pi M$ = 125 Oe, and .2804μm for $4\pi M$ = 300 Oe. From the definition $H_o = H_o/4\pi M$, H_o = 0.6639 for $4\pi M$ = 125 Oe, and 0.2767 for $4\pi M$ = 300 Oe. From equation 3.6, λ = 0.04572 and 0.2996 for $4\pi M$ = 125 Oe and 300 Oe, respectively. From the definition $\lambda = \ell/h$, the thickness of the layer with $4\pi M$ = 125 Oe must be 18μm, and the thickness of the other layer must be 0.9359μm. From equation 3.5, X_o is 0.1515 and 0.6008, respectively. From the definition $X_o = r_o/h$, r_o is 2.727 m and 0.5623μm, respectively. From equation 3.7, the normalized run-out field is 0.5552 and 0.5623, respectively, so that H_{Ro} = 69.4 Oe and 51 Oe, respectively. If the operating bias field H = 76 Oe, from equation 3.3, X is 0.2118 and 0.9651, which corresponds to a bubble radius of 5.61μm for the large bubble film and 0.903μm for the small bubble film. This procedure illustrates how such calculations can be performed, for a variety of values of $4\pi M$ and H_o.

Figures 3.3, 3.4, and 3.5 are graphs of the proper film thickness as a function of $4\pi M$ for layers having a collapse threshold of 83 Oe, 57 Oe, and 198 Oe, respectively. The radius r_o of the bubble at the collapse threshold is also plotted, as is the radius at a suitable operating bias.

To illustrate the use of figures 3.3, 3.4, and 3.5, assume a two layer bubble memory. The carrier bubbles have a chosen diameter of 7μm and operate at a bias field of 76 Oe. Figure 3.3 indicates that the $4\pi M$ of the carrier layer should be 150 Gauss, and that the thickness of the carrier layer should be 7.5μm. If the diameter of the data bubbles is to be one fourth of the carrier bubbles, or 1.75μm, then each carrier bubble may carry up to seven data bubbles. Figure 3.3 indicates that the $4\pi M$ of the data layer should be 315 Gauss, and the thickness of the data film should be 0.88μm. In actual practice this data film would be made by gradually thinning a thicker layer, monitoring the bubble collapse threshold between thinnings until the operating regions of the two films coincide.

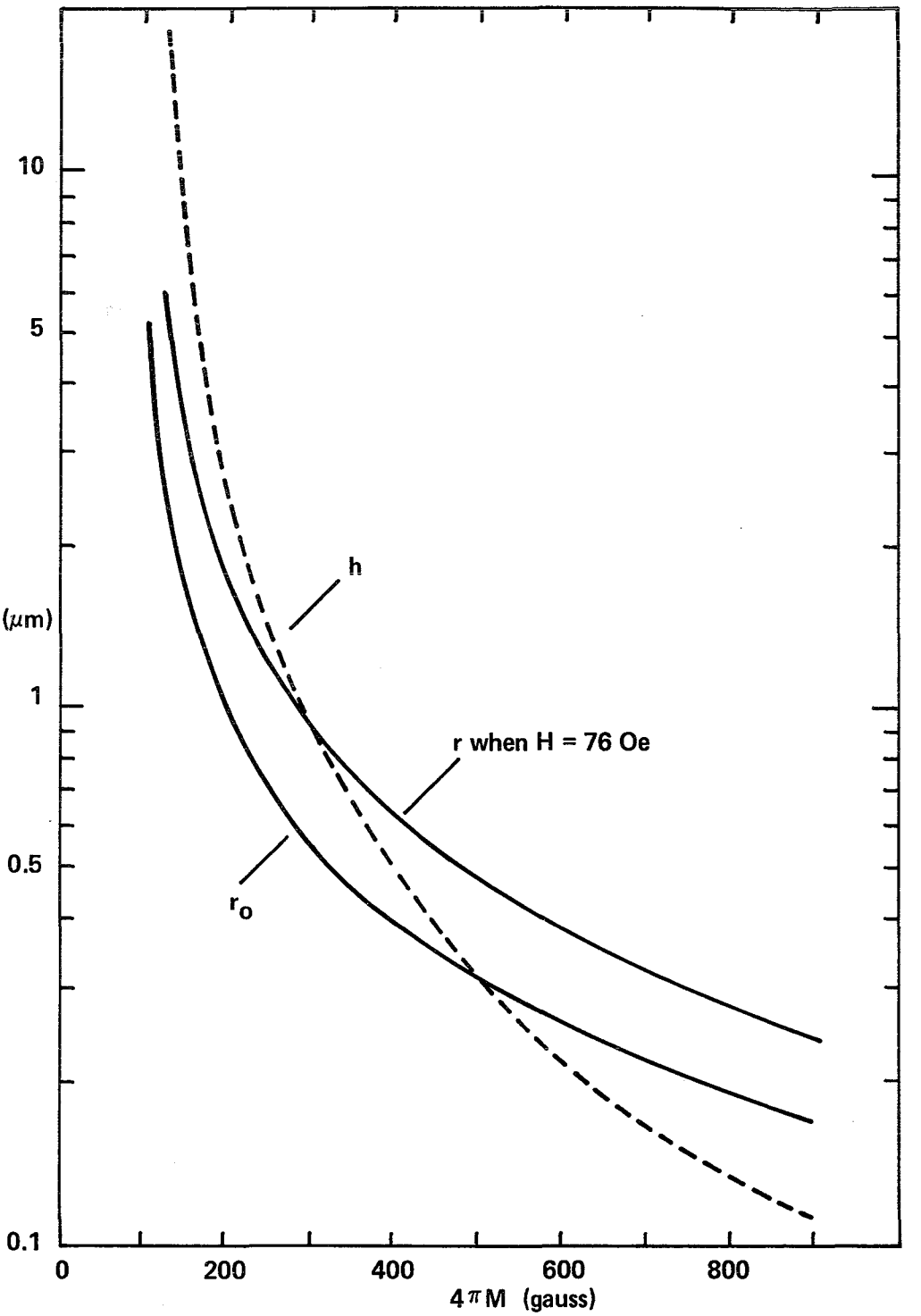

Figure 3.3 Bubble Radius r_o and Film Thickness h vs. $4\pi M$, with Collapse Threshold H_o = 83 Oe.

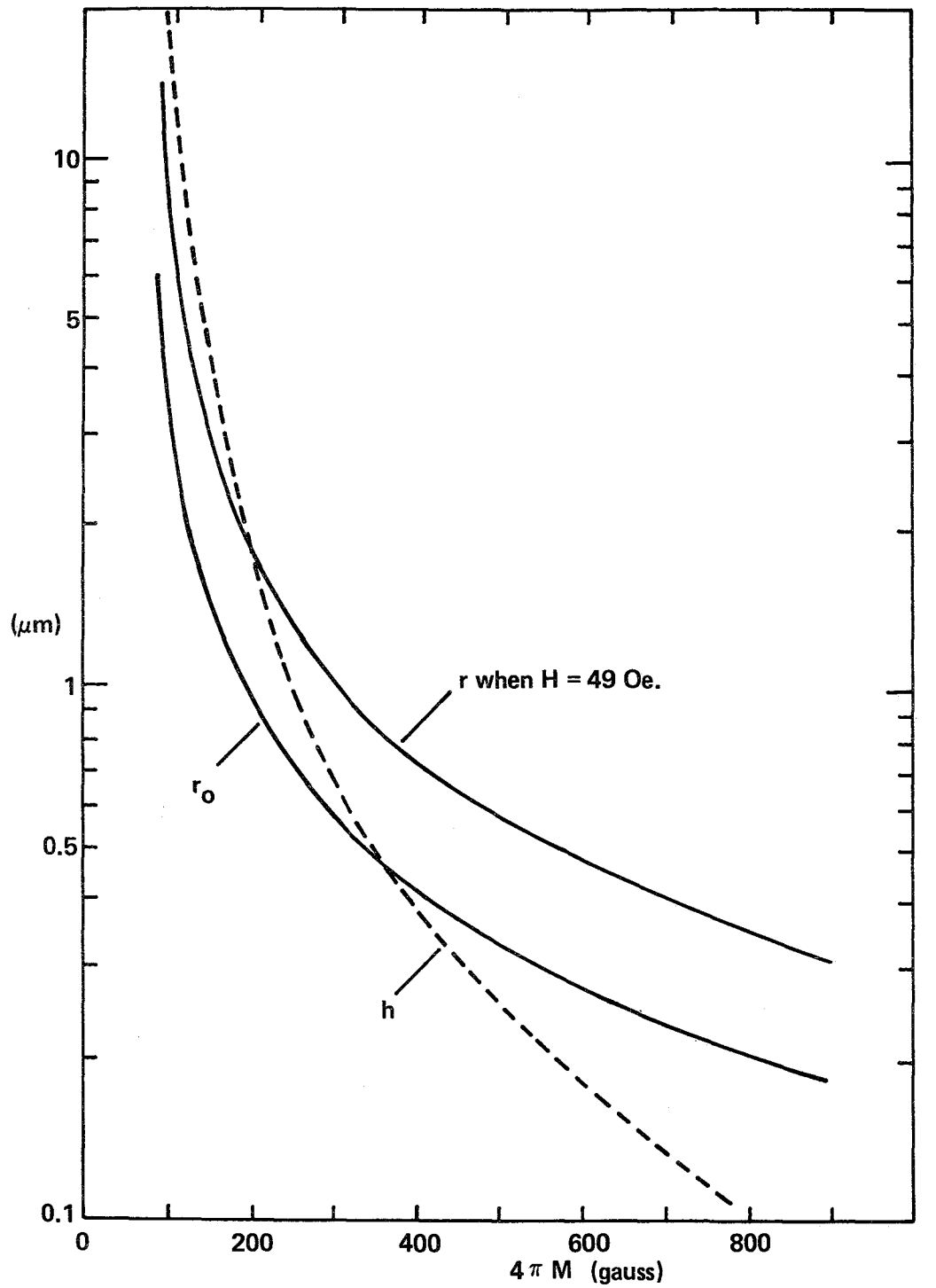

Figure 3.4 Bubble Radius r_o and Film Thickness h vs. $4\pi M$, with Collapse Threshold H_o = 57 Oe.

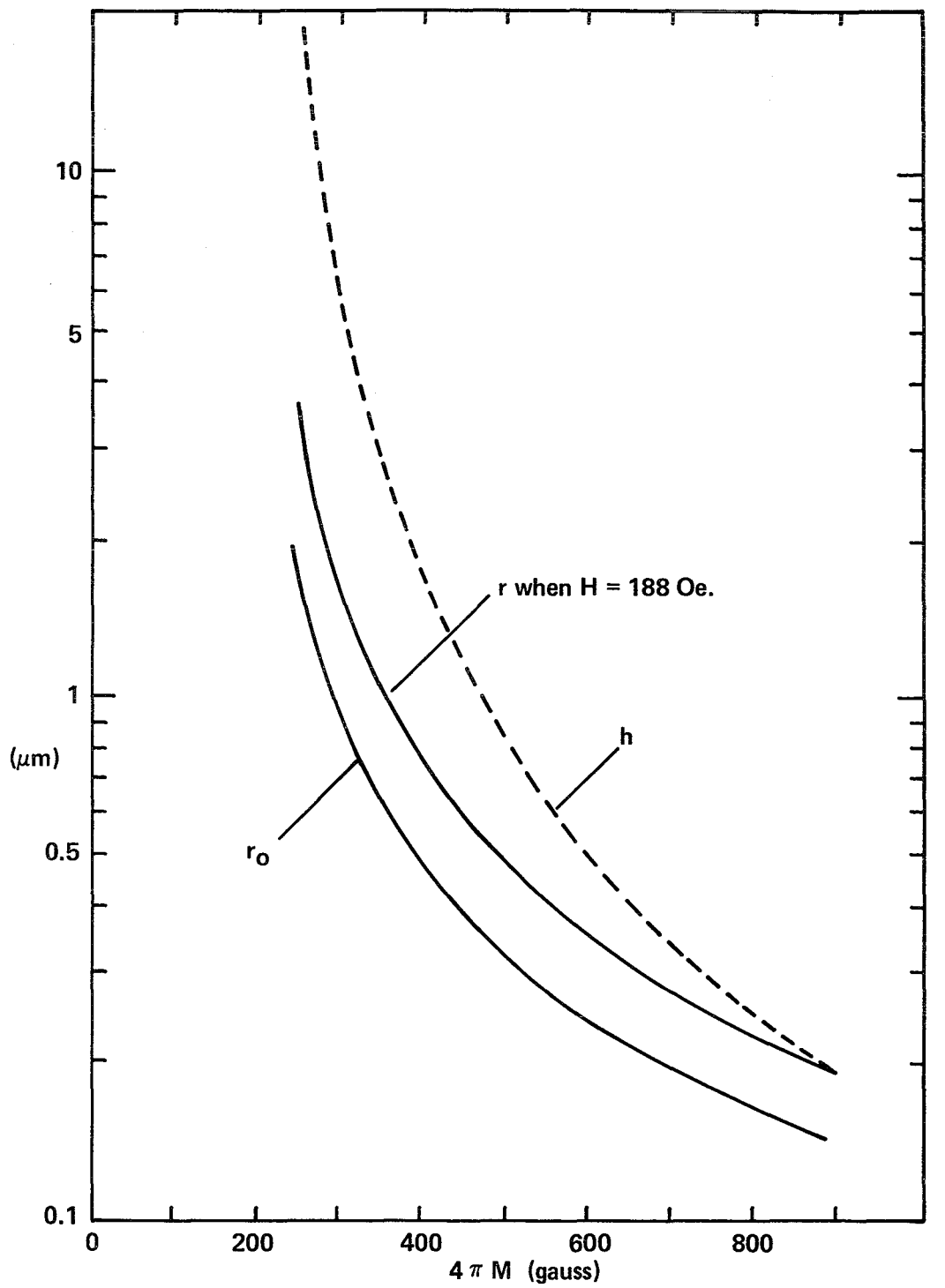

Figure 3.5 Bubble Radius r_o and Film Thickness h vs. $4\pi M$, with Collapse Threshold H_o = 198 Oe.

From these figures we see that large variations in bubble radius, a factor of 20 or more, can be obtained with compatible operating ranges. A practical difficulty is that the small bubbles require the films to be very thin. This, in turn, presents two problems which all small bubble memories have: a fabrication problem and a read-out problem. The fabrication problem is to grow thin enough layers. Using the usual lead oxide flux, initial growth rate is exceedingly fast, so that a one micron film grows when one just dips the film into the melt and pulls the film out. The problem can be solved either by using a lithium molybdate melt in which films have a very slow growth rate, or by thinning a film grown in the conventional lead melt by ion milling or chemical etching. The read-out problem is ameliorated somewhat by the fact that the small bubble films have higher $4\pi M$; however, read-out is still a problem for all small bubble memories and not just multilayer structures.

3.3 Coupling Between Stripe and Bubble Layers

One class of multilayer bubble lattice file uses stripe domains in one layer to propagate bubbles in a second layer. A calculation of the coupling strength due to both the exchange force and the magnetostatic field is presented herein.

Because the stripe films that respond best to in-plane fields have high $4\pi M$ values and very narrow stripes, a mismatch in size between bubbles and stripes is likely. The calculations show that the coupling strength decreases in a non-monotonic fashion as the stripe width decreases, relative to the bubble diameter. The coupling is never zero unless the stripe width is zero, and therefore, stripes can be used to propagate bubbles even though they are not matched in size.

Exchange coupling and magnetostatic coupling are roughly of equal importance if no separating layer is used. Magnetostatic coupling decreases as the thickness of the bubble layer increases, decreases as the width of stripes decreases, and, if a separating layer is used, decreases as the separation increases.

3.3.1 Exchange Coupling

Exchange coupled double layer garnet films are made by epitaxially growing a magnetic garnet layer directly on another magnetic garnet layer with different properties. There is no non-magnetic layer between them.

In the past, such double layer garnet films have been grown for the purpose of having one layer replace the external normal bias field required to sustain bubbles. For this application, one

layer is always saturated, while the other layer contains bubbles. Exchange energy causes the saturated layer to exert a torque on the spins of the bubble layer that tends to saturate the second layer, and thereby emulate a bias field. The magnetostatic field from the saturated film is negligible for the same reason that the electrostatic field of a parallel plate capacitor is negligible outside the capacitor.

The strength of the exchange coupling is experimentally measured by measuring the difference in the bubble collapse field in one layer with the other layer saturated in two opposite states. Half of the difference between the two collapse fields is the coupling strength in Oersteds. It is conventional to report the strength of the exchange coupling in Oersteds for that reason, although the exchange coupling is not a magnetic field. The experimental value obtained will depend strongly on the thickness and aspect ratio of the bubble. An exchange bias of 31 Oersteds on a 1.6μm thick bubble film of $(YSm)_3$ GaIG exerted by a bias layer of $(EuEr)_3$ GaIG has been reported.[4] Therefore, for the theoretical calculations, an exchange coupling of 31 Oersteds is assumed. It is also assumed that there is no domain closure structure.

3.3.2 Mismatch Between Stripe Width and Bubble Diameter

When the diameter of a bubble is equal to or less than the width of a stripe in a double layer structure, the bubble will be held by the exchange force over the area of the surface of the bubble that is in contact with the stripe. When the bubble diameter is larger than the stripe width, the bubble will intersect two or more stripes. Those stripes in which the spins in the iron sublattice are parallel to those in the bubble will attract the bubble; those with oppositely oriented spins in the iron sublattice, repel. The net exchange attraction is proportional to the difference in area of those portions of attracting and repelling stripes enclosed by the bubble.

The bubble will position itself in order to maximize the area of contact with attracting stripes and minimize the area of contact with repelling stripes. Figure 3.6.a shows the equilibrium position when the diameter of the bubble is only slightly larger than the width of the stripe. Figure 3.6.b shows the equilibrium position when the width of the stripes is decreased further. Note that the bubble is non-symmetrically arranged with respect to the stripes. Equilibrium occurs when the condition

$$h_1 - h_2 + h_3 = 0$$

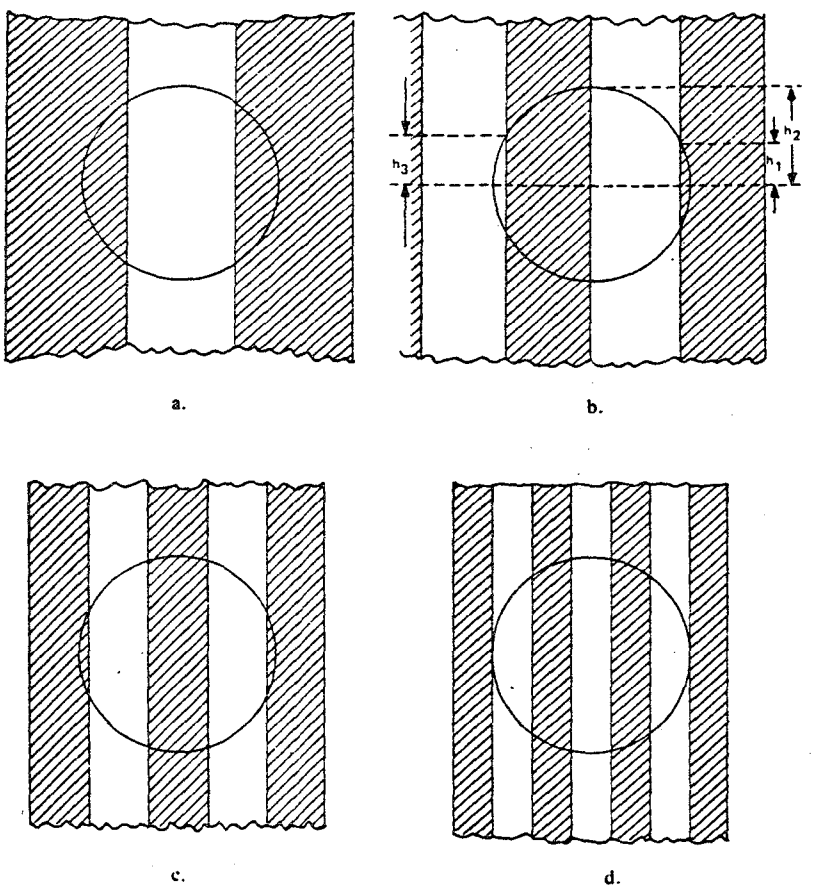

Figure 3.6 Equilibrium Configurations of Stripe and Bubble Domains.

is fulfilled, with h_1, h_2, and h_3 defined as in figure 3.6.b. Regardless of the width of the stripe, there is always some position where the bubble has lower energy; that is, there is always a positive coupling. Figures 3.6.c and d show stable configurations in which the stripe width is decreased further.

The strength of the coupling is easily determined by calculating the difference in area of those portions of attracting and repelling stripes enclosed by the bubble. The result is shown in figure 3.7. Coupling strength decreases in a non-monotonic fashion as the stripe width decreases, and is zero only when the stripe width is zero.

It is necessary to determine how much coupling is required for propagation. Conventional garnet bubble films for memories have coercivity of approximately one tenth of one Oersted. Thus, a coupling field greater than one tenth of one Oersted should be sufficient to propagate a bubble.

3.3.3 Magnetostatic Coupling

Coupling between stripes and bubbles also occurs by magnetostatic interaction. If stripes are of equal width, the dependence of magnetostatic coupling upon the relative stripe/bubble size is similar to that of exchange coupling, as shown in figure 3.7. The "full scale" magnitude of the magnetostatic coupling, the magnitude of coupling when the width of the stripe is larger than the bubble diameter, depends strongly on the thickness of the bubble film and on the intensity of magnetization $4\pi M$ of the stripe field.

The field from a stripe domain is calculated by considering a stripe domain layer of thickness h. Let the wavelength of the stripes by λ, let the distance parallel to the film surface and perpendicular to the stripes be x, let the point $x = 0$ be in the middle of a stripe, and let the distance above the top surface of the film be z. Starting with div $\vec{B} = 0$ and $\vec{B} = \vec{H} + 4\pi\vec{M}$,

$$\text{div } (\vec{H} + 4\pi\vec{M}) = 0 \tag{3.10}$$

$$\text{div } H = -4\pi(\nabla \cdot M) \equiv 4\pi p_m \tag{3.11}$$

where $p_m = \nabla \cdot M$ is the magnetic charge per unit volume. Consider a narrow strip, running along a stripe at the film surface, uniformly charged. Surrounding this with a Gaussian surface, the result is

$$H = \frac{2\lambda_m \hat{S}}{S} \tag{3.12}$$

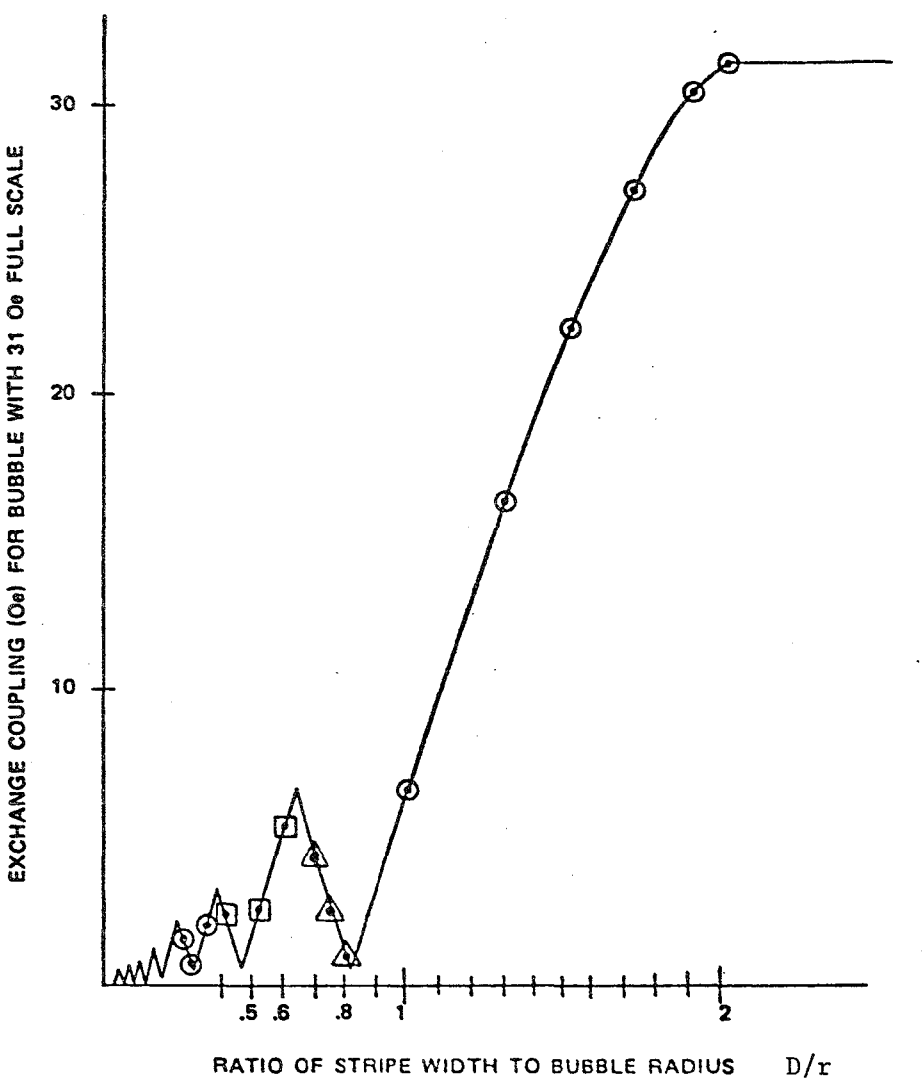

Figure 3.7 Exchange Coupling vs. Ratio of Stripe Width to Bubble Radius.

where s is the distance from the narrow strip, λ_m is the magnetic charge per unit length, and $\hat{s}$ is a unit vector. The stripe domain garnets under consideration have a low anistropy field H_k so that they may be aligned with a magnetic field. If the average z component of magnetization in the stripe film is assumed to be given by

$$M_z = M \cos \frac{2\pi x}{\lambda} \tag{3.13}$$

then the z component of the stray field is given by

$$H_z = 2M\cos \frac{2\pi x}{\lambda} \int_{-\infty}^{\infty} \left\{ \frac{\cos \frac{2\pi x}{\lambda} z}{z^2 + x^2} - \frac{\cos \frac{2\pi x}{\lambda}(z + h)}{(z + h)^2 + x^2} \right\} dx \tag{3.14}$$

This equation yields

$$H_z = 2\pi M \left[\exp\left(\frac{-2\pi z}{\lambda}\right) - \exp\left(\frac{-2\pi(z + h)}{\lambda}\right) \right] \cos \frac{2\pi x}{\lambda} \tag{3.15}$$

Let the thickness of the bubble film by h_B and let the spacing between the bubble film and the stripe film be h_G. The full scale magnetostatic coupling field, H_{FS}, from the stripe film to the bubble film is found by averaging equation 3.15 between the limits h_G and $h_G + h_B$:

$$H_{FS} = \frac{M\lambda}{h_B} \left[\exp\left(\frac{-2\pi h_G}{\lambda}\right) - \exp\left(\frac{-2\pi(h_G + h_B)}{\lambda}\right) + \exp\left(\frac{-2\pi(h_G + h_B + h)}{\lambda}\right) - \exp\left(\frac{-2\pi(h_G + h)}{\lambda}\right) \right] \tag{3.16}$$

When the thickness of the spacer layer is zero and when the thickness of the stripe film is greater than the stripe wavelength λ, equation 3.16 reduces to

$$H_{FS} \simeq \frac{M\lambda}{h_B} \left[1 - \exp\left(\frac{-2\pi h_B}{\lambda}\right) \right] \tag{3.17}$$

Figures 3.8 and 3.9 show how this full scale coupling depends on the thickness of the bubble film, the wavelength of the stripes, and the thickness of the Gadolinium Galium Garnet (GGG) layer

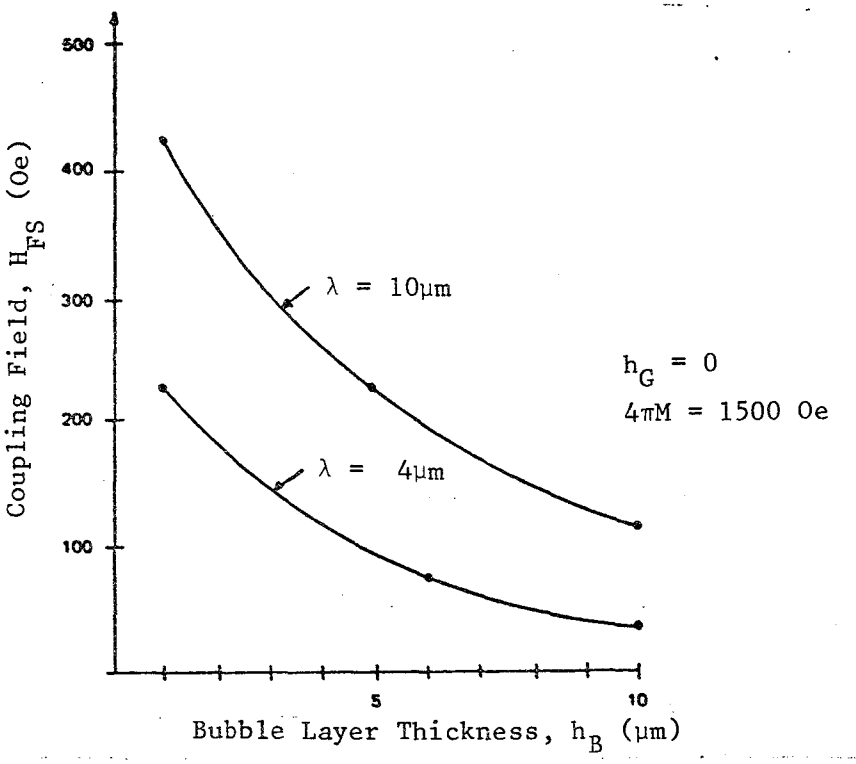

Figure 3.8 Magnetostatic Coupling vs. Bubble Layer Thickness with Zero Separation for Two Stripe Wavelengths.

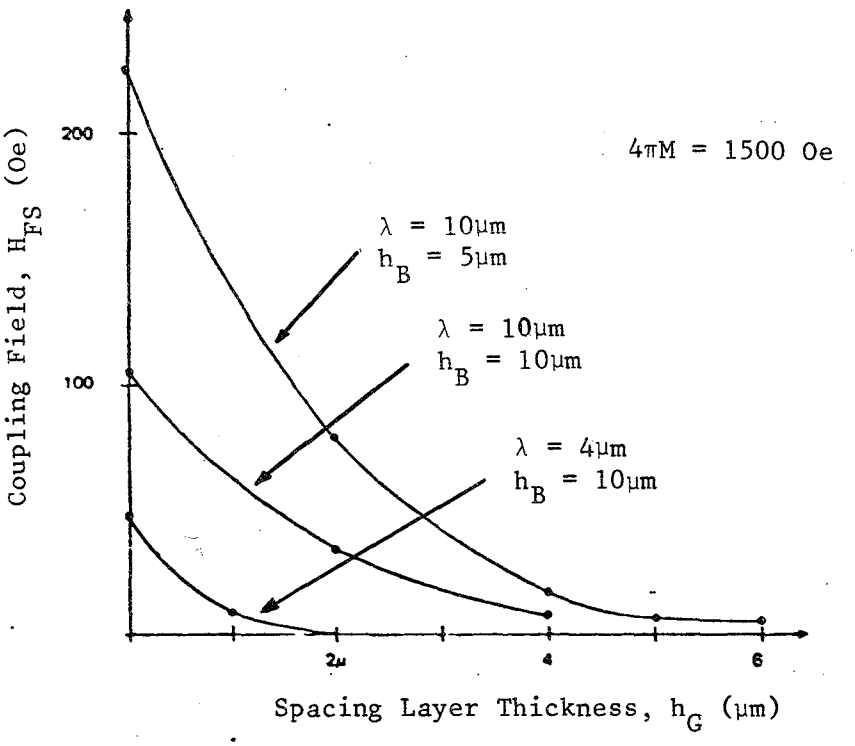

Figure 3.9 Magnetostatic Coupling vs. Gap Thickness Between Bubble Layer and Stripe Layer.

separating the stripe and bubble films. As thickness of the bubble layer increases, the coupling decreases; as the width of the stripes increases, the coupling increases; and, as the thickness of the separation layer increases, the coupling decreases. A $4\pi M$ value of 1500 Oe was assumed for the stripe film; if gallium is used to substitute for some of the iron, the $4\pi M$ will be less and the coupling proportionately reduced.

3.3.4 Stripe-Bubble Interaction

Stripe domains in one layer can trap bubbles in another layer, so that when the stripes are moved they move the bubbles along with them. The interaction is due to the magnetic stray field from the stripes. Therefore, knowledge of the strength and spatial dependence of that field is of importance for design considerations.

Equation 3.15 is plotted in figure 3.10 as a function of distance above the garnet layer. Note that the interaction can be made as strong as $2\pi M$, which is far more than needed for strong coupling. Also, the stray-field value can be adjusted to whatever value desired simply by choosing the proper spacer thickness. Note that the thickness of the stripe domain film is immaterial for thicknesses greater than the stripe wavelength, λ.

3.3.5 Stripe and Bubble Material Selection

In this section theoretical relationships are derived that provide the crystal grower with knowledge of the proper film parameters for a coupled strip-bubble multilayer.

The stripe layer in a multilayer self-structured bubble memory should have wide, rather than narrow, stripes if chevrons or current conductors are used to move the stripes. The properties of the stripe film and the bubble film should be similar, but since both must operate in the same external bias field, their characteristics must be different enough so that one is above the run-out threshold and the other is below. Explicit relationships are derived for the % change in run-out threshold due to a % change in: (1) thickness, (2) magnetization, (3) characteristic length, (4) anisotropy constant, and (5) exchange constant. Various stray field formulas for isolated stripes are also given.

Consider a double layer film in which one layer supports stripes and the other supports bubbles. The purpose of such a structure is to move the bubbles by moving the stripes. Since most stripe propagation schemes being investigated require small structures (conductors, chevrons, etc.), the stripes must be wide. Such wise stripes are found in high Q, low $4\pi M$ films of the type used

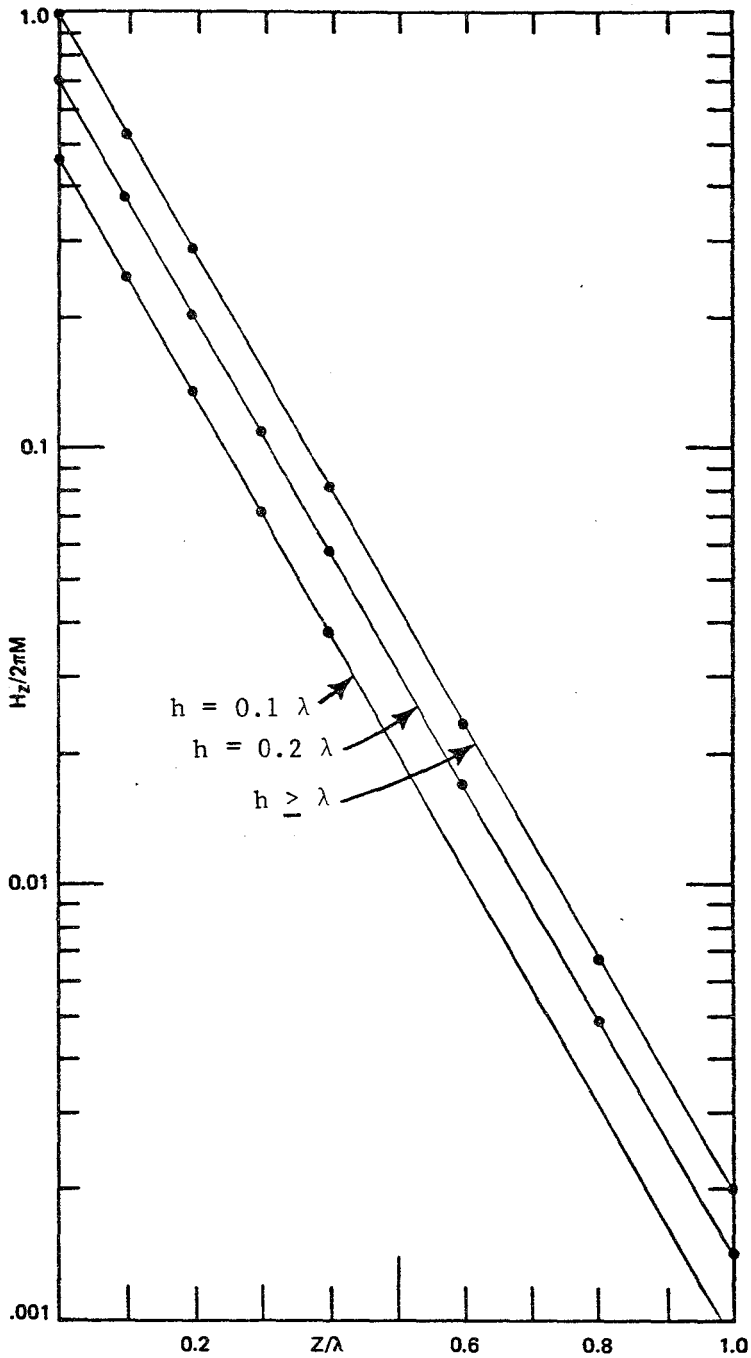

Figure 3.10 Normal Component of Stray Field vs. Height Above a Stripe Domain of Thickness h and Wavelength λ.

for bubbles rather than in the low Q, high $4\pi M$ films used for light deflectors. Therefore, the stripe and bubble films should be not too dissimilar.

3.4 Stripe Domain and Material Parameters

At the edge of an infinitely long stripe, the normal component of the stray field averaged over thickness was first derived by Kooy and Enz:[5]

$$\frac{H_w}{M} = \frac{2}{\pi}\left[\tan^{-1}\left(\frac{h}{w}\right) - \frac{w}{2h}\ln\left(1 + \frac{h^2}{w^2}\right)\right] \tag{3.18}$$

where w is the width of a stripe.

A useful approximation to equation 3.18 is given by O'Dell:[6]

$$\frac{H_w}{M} = \frac{4\pi}{1 + \pi W/h} \tag{3.19}$$

Let the x-axis lie in the film plane and let the walls of the stripe domain be at $x = 0$ and $x = W$. The z component of the stray field, $H(x)$ at the point x, can be calculated from H_W by considering the field to be due to two stripe domains, one of width x and the other of width $W - x$:

$$H(x) = H_W(x) + H_W(W - x) - 4\pi M.$$

Note that $4\pi M$ has been subtracted so as not to add twice the field from the saturated film in which the stripe is superposed. The average field over the whole domain is

$$\bar{H}_W = \frac{1}{W}\int_0^W H(x)dx. \tag{3.20}$$

When the O'Dell approximation, equation 3.19, is used, the result is:

$$\frac{\bar{H}_W}{M} = -4\pi + \frac{8h}{W}\ln\left(1 + \frac{\pi W}{h}\right) \tag{3.21}$$

Derivation of the field at the tip of an isolated rectangular stripe, averaged over both x and thickness, is similar to the derivation of equation 3.20, except that two rectangular strips joined end to end are considered:

$$\bar{H}_{tip} = \frac{1}{2}(\bar{H}_W + 4\pi M). \tag{3.22}$$

If the O'Dell approximation, equation 3.19, is used, then

$$\bar{H}_{tip} \simeq \frac{4h}{W} \ln\left(1 + \frac{\pi W}{h}\right) \tag{3.23}$$

Note that from equations 3.19 and 3.21 the following relationship holds:

$$\frac{1}{2}\left[\bar{H}_W + W\frac{\partial \bar{H}_W}{\partial W} + 4\pi M\right] = H_W \tag{3.24}$$

3.4.1 Run-Out Threshold

Consider an isolated stripe domain of width W and length L in a film of thickness h. The total energy is the sum of the applied field energy, the stray field energy, and the wall energy:

$$E = E_A + E_o + E_W$$

$$= 2WhLMH + WhL(\bar{H}_W - 4\pi M) + 2(L + W)\,\sigma_W h.$$

Assuming that L>>W, and requiring that at the run-out threshold the domain neither shrinks or grows, so that $\partial E/\partial L = 0$, leads to

$$0 = H - \frac{1}{2}(\bar{H}_W + 4\pi M) + \sigma_W M^{-1}{}_W{}^{-1}. \tag{3.25}$$

The condition $\partial E/\partial W = 0$ results in a second equation:

$$0 = 2H - \bar{H} - W\frac{\partial \bar{H}_D}{\partial W} - 4\pi M. \tag{3.26}$$

From equation 3.24, equation 3.26 becomes:

$$0 = H - H_W \tag{3.27}$$

and with equation 3.19 this becomes:

$$H = \frac{4\pi M}{1 + \pi W/h} \text{ , or } 1 + \frac{\pi W}{h} = \frac{4\pi M}{H} \tag{3.28}$$

Substituting equation 3.21 into equation 3.25 gives:

$$0 = H - \frac{4h}{W} \ln\left(1 + \frac{\pi W}{h}\right) + \frac{\sigma_W}{MW} \tag{3.29}$$

Using equation 3.28 to substitute for $(1 + \pi D/h)$ in equation 3.29 yields:

$$0 = H - \frac{4h}{W} \ln\left(\frac{4\pi M}{H}\right) - \frac{\sigma_W \pi}{Mh}\left[\frac{H}{4\pi M - H}\right] \tag{3.30}$$

Rewriting equation 3.30, using

$$\lambda \equiv \frac{\sigma_W}{4\pi M^2 h} = \frac{\ell}{h} \tag{3.31}$$

and noting that, by definition, when $\partial E/\partial L = 0$, the applied bias field, H, is the run-out field, gives:

$$\frac{H_{RO}}{4\pi M} = 1 + \pi\lambda - \ln\left(\frac{4\pi M}{H_{RO}}\right) \tag{3.32}$$

3.4.2 Layer Thickness

The percent change in run-out threshold as a result of changing the thickness, h, by one percent is presented below. Taking the partial derivative of equation 3.32 with respect to h gives:

$$\frac{\delta H_{RO}}{4\pi M} = \frac{\pi \delta\lambda}{\delta h}\,\delta h + \frac{\delta H_{RO}}{H_{RO}} \text{ .} \tag{3.33}$$

Differentiation of equation 3.31 yields:

$$\frac{\delta\lambda}{\delta h} = -\frac{\lambda}{h} \tag{3.34}$$

Substituting equation 3.34 in equation 3.33 gives:

$$\frac{\partial H_{RO}}{H_{RO}} \Big/ \frac{\partial h}{h} = \frac{\pi\lambda}{1 - H_{RO}/4\pi M} \cdot \tag{3.35}$$

When equation 3.32 is used to remove λ from the equation 3.35, the result is:

$$\frac{\partial H_{RO}}{H_{RO}} \Big/ \frac{\partial h}{h} = \frac{\ln\left(\frac{4\pi M}{H_{RO}}\right)}{1 - H_{RO}/4\pi M} - 1 \tag{3.36}$$

Equation 3.36 is plotted in figures 3.11 and 3.12. Note that the right hand side of equation 3.36 is always positive, which means that as film thickness increases the run-out threshold increases.

3.4.3 Magnetization

The derivation of the ratio of the percent change in run-out field to the percent change in $4\pi M$ is similar to the derivation of the thickness dependence in the previous section. The assumption is made when $4\pi M$ is changed (for example, by the substitution of more iron oxide for gallium oxide), K, the anistropy constant, remains unchanged. The result is:

$$\frac{\partial H_{RO}}{H_{RO}} \Big/ \frac{\partial M}{M} = \frac{2}{1 - H_{RO}/4\pi M} \ln\left(\frac{4\pi M}{H_{RO}}\right) \tag{3.37}$$

Equation 3.37 is always positive, so increasing $4\pi M$ always increases the run-out threshold. Moreover, the change is very large. Equation 3.37 is plotted in figures 3.13 and 3.14.

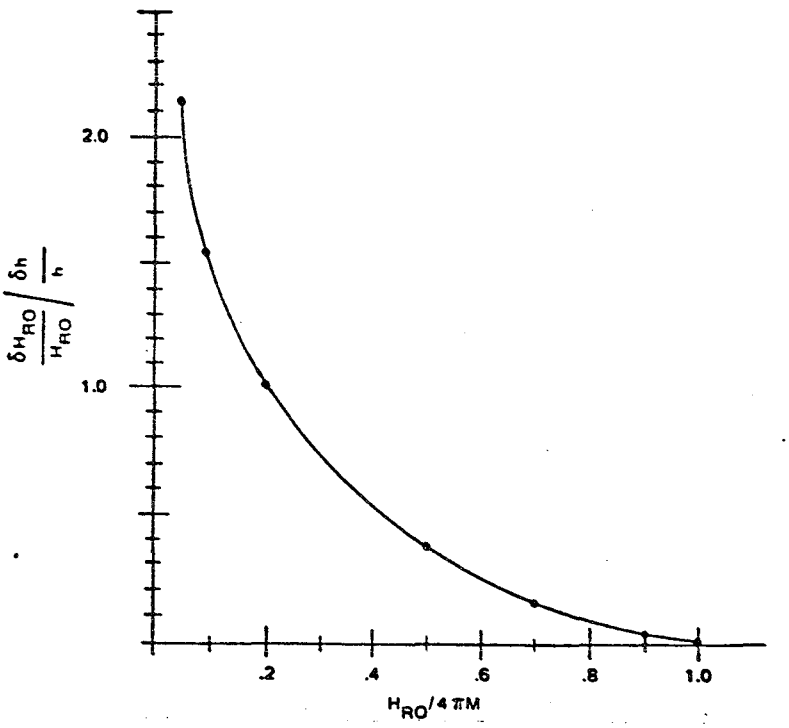

Figure 3.11 Ratio of the Percentage Change in Run-Out Field to the Percentage Change in Film Thickness vs. Run-Out Field.

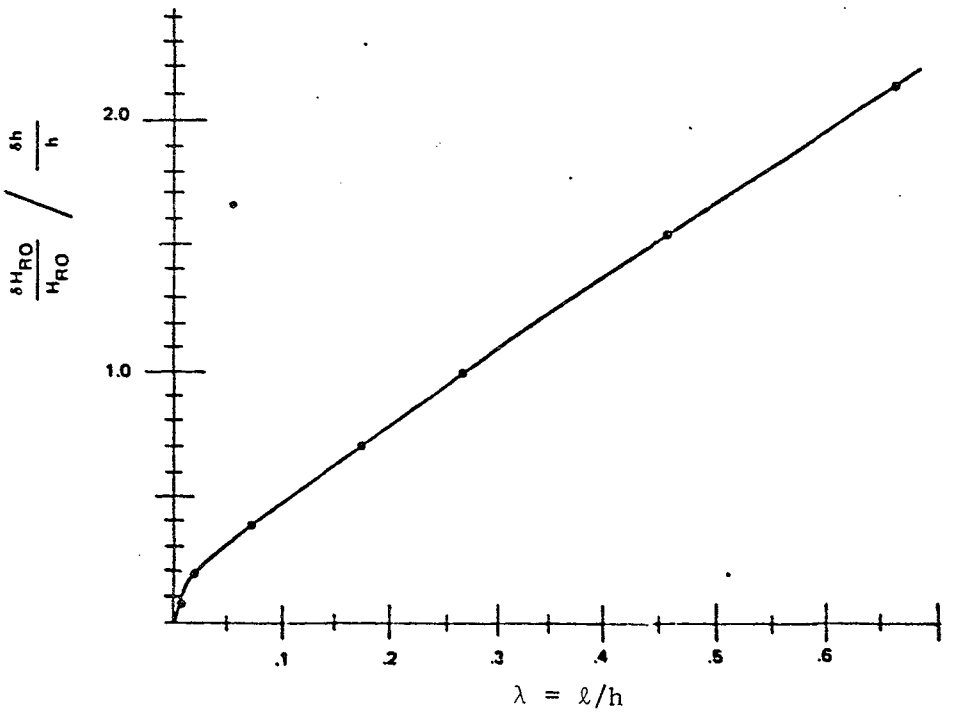

Figure 3.12 Ratio of the Percentage Change in Run-Out Field to the Percentage in Film Thickness vs. Characteristic Length.

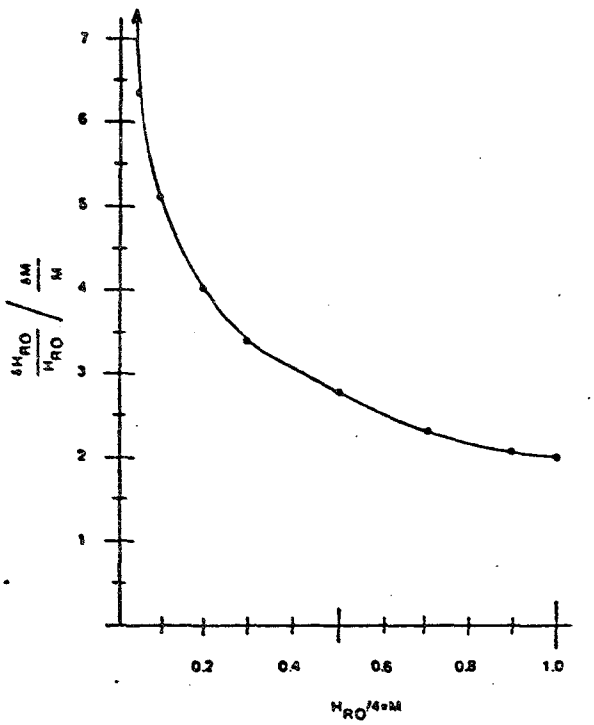

Figure 3.13 Ratio of the Percentage Change in Run-Out Field to the Percentage Change in Magnetization vs. Run-Out Field.

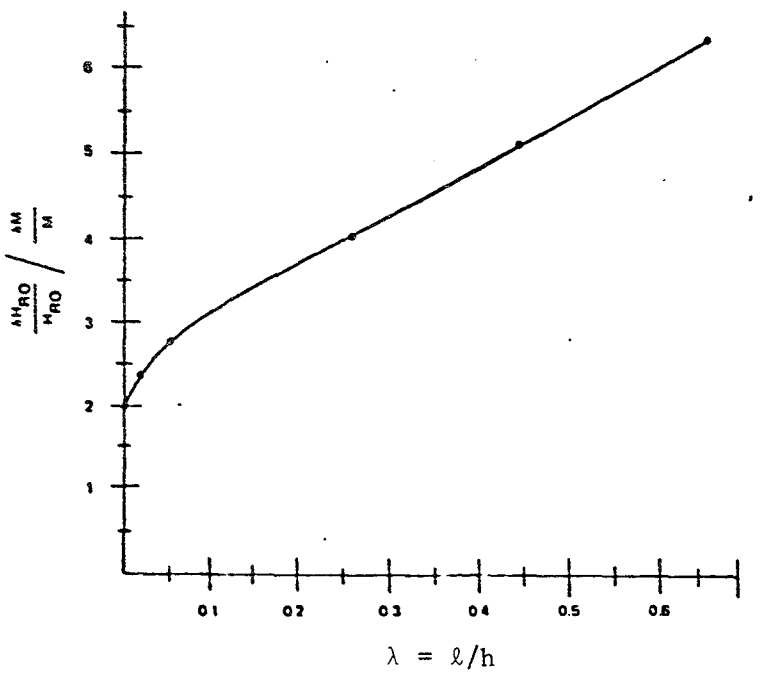

Figure 3.14 Ratio of the Percentage Change in Run-Out Field to the Percentage Change in Magnetization vs. Characteristic Length.

3.4.4 Characteristic Length

The characteristic length, ℓ, is one of the fundamental parameters measured in garnets, and is defined as $\sigma_w/4\pi M^2$. The percent change in run-out threshold due to a one percent change in characteristic length (for example, due to a change in wall energy) is given by:

$$\frac{\partial H_{RO}}{H_{RO}} \Big/ \frac{\partial \ell}{\ell} = \frac{H_{RO}/4\pi M}{1 - H_{RO}/4\pi M} \ln\left(\frac{4\pi M}{H_{RO}}\right) \tag{3.38}$$

This is plotted in figures 3.15 and 3.16.

3.4.5 Uniaxial Anisotropy and Exchange Constant

The wall energy per unit length and thickness is $\sigma_W = 2A^{\frac{1}{2}}K^{\frac{1}{2}}$. The dependence of the run-out field on exchange constant and anisotropy constant can be calculated as in the preceding section knowing that

$$\frac{\partial \sigma_W}{\sigma} = \frac{1}{2}\frac{\partial K}{K} \text{ and } \frac{\partial \sigma_W}{\sigma} = \frac{1}{2}\frac{\partial A}{A}$$

The resulting equations are:

$$\frac{\partial H_{RO}}{H_{RO}} \Big/ \frac{\partial A}{A} = -\frac{1}{2}\left(\frac{H_{RO}/4\pi M}{1 - H_{RO}/4\pi M}\right) \ln\left(\frac{4\pi M}{H_{RO}}\right) \tag{3.39}$$

and

$$\frac{\partial H_{RO}}{H_{RO}} \Big/ \frac{\partial K}{K} = -\frac{1}{2}\left(\frac{H_{RO}/4\pi M}{1 - H_{RO}/4\pi M}\right) \ln\left(\frac{4\pi M}{H_{RO}}\right) \tag{3.40}$$

These are plotted in figures 3.17 and 3.18.

The most important film parameter affecting the run-out threshold is magnetization, followed by film thickness, characteristic length, and exchange energy and anisotropy constant, in that order. For example, in a film with $H_{RO}/4\pi M = 0.2$, a 10% change in $4\pi M$ causes a 40% change in run-out threshold, a 10% change in

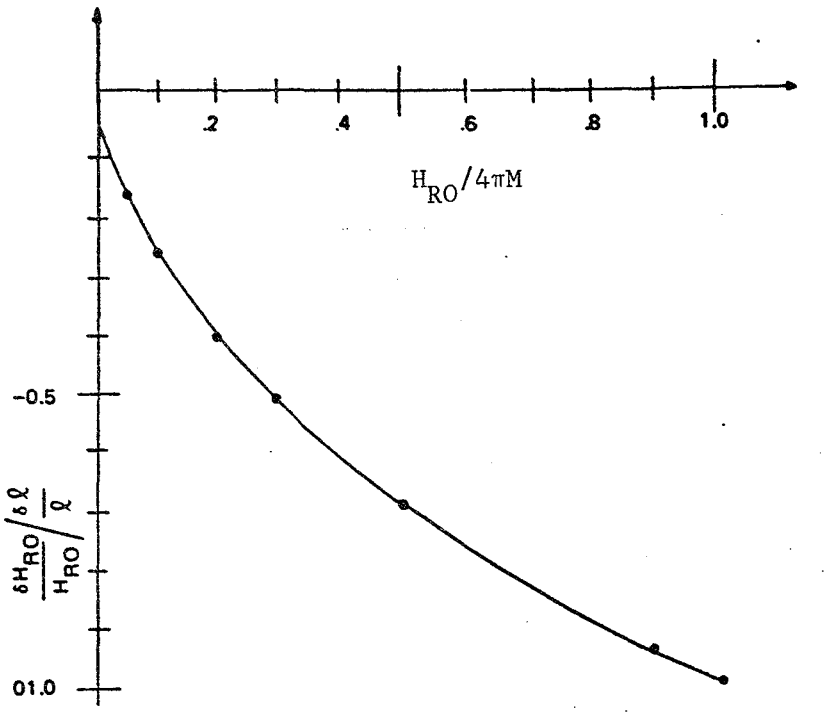

Figure 3.15 Ratio of the Percentage Change in Run-Out Field to the Percentage Change in Characteristic Length vs. Run-Out Field.

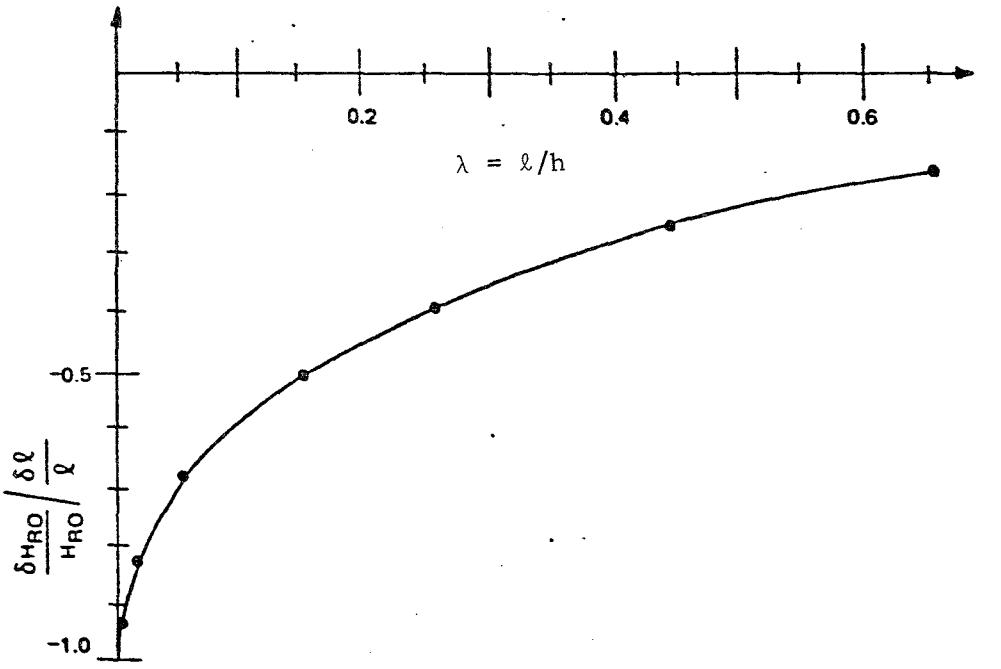

Figure 3.16 Ratio of the Percentage Change in Run-Out Field to the Percentage Change in Characteristic Length vs. Characteristic Length.

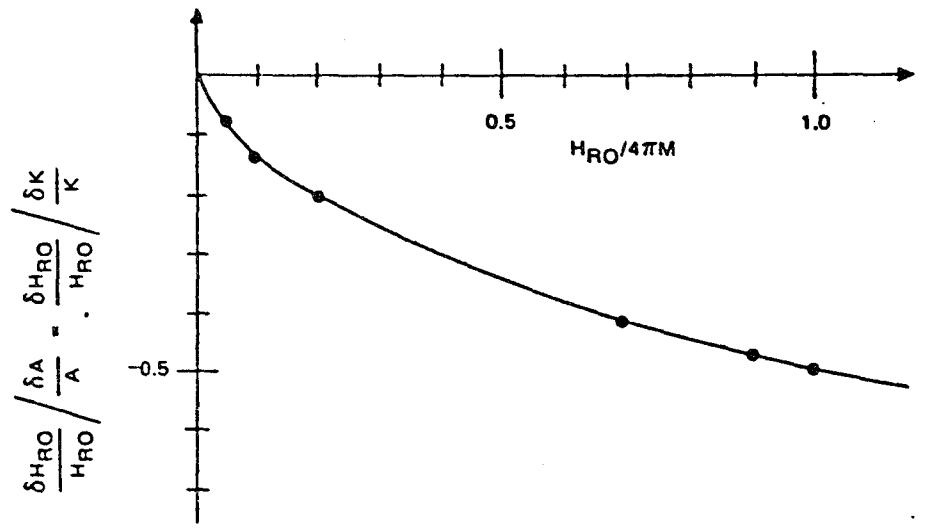

Figure 3.17 Ratio of the Percentage Change in Run-Out Field to the Percentage Change in Both the Anisotropy Constant and Exchange Constant vs. Run-Out Field.

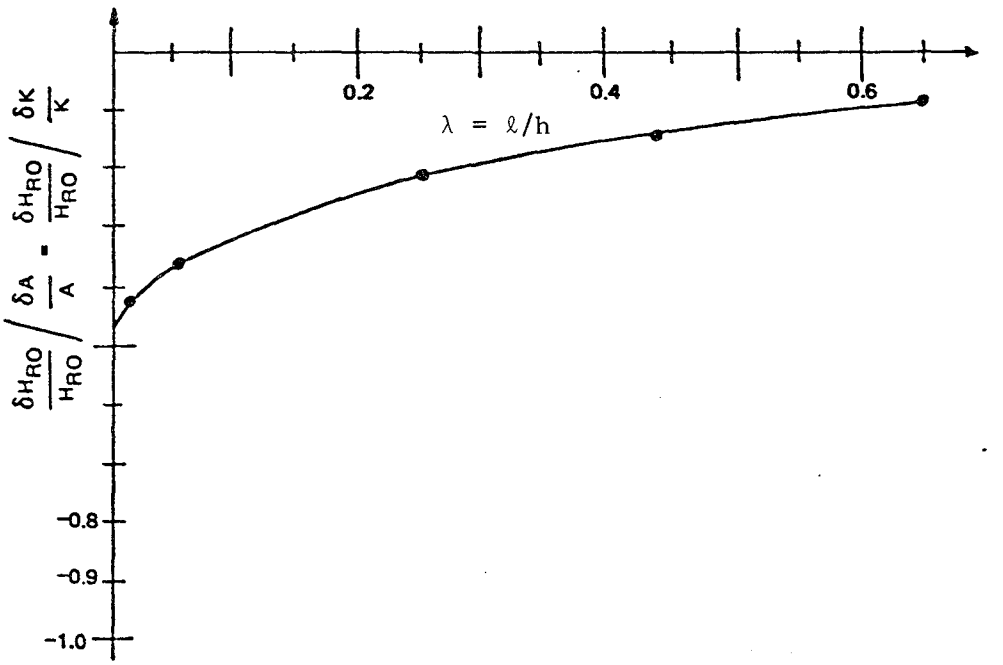

Figure 3.18 Ratio of the Percentage Change in Run-Out Field to the Percentage Change in Both the Anisotropy Constant and Exchange Constant vs. Characteristic Length.

thickness causes a 10% change in run-out threshold, a 10% change in characteristic length causes a -4% change in run-out field, and a 10% change in either anisotropy constant or exchange constant causes a -2% change in run-out threshold.

One of the intriguing possibilities emerging from this treatment is that a magnetostatically coupled stripe-bubble combination is possible in which the bubble and stripe films have the same composition but different thicknesses.

3.4.6 Stripe Domain Curvature

When a group of stripe domains are propagated between two rows of chevrons or other structures, they bow or curve backwards. Figure 3.19 displays the case of an isolated stripe. When an oscillating normal field commonly called a tickle field, is applied, the stripes straighten out. The bowing is caused by coercivity; the straightening out is caused by three factors: (1) The coercivity is effectively reduced because the oscillating normal field causes the width of each stripe domain to oscillate somewhat, helping that stripe to move past micro-defects, (2) The stripes repel each other magnetostatically, and (3) The oscillating field plus the bias field exceeds the strip-out threshold at least part of the time, causing the stripes to be in tension. If the ends of the stripes were not pinned to the chevrons, the stripes would contract to bubbles when the strip-out threshold is exceeded. However, when the ends are pinned, the stripes can only reduce their length, and therefore, lower their energy by straightening out. This third cause is the subject of this section. Note that a stripe near other stripes may see a local field higher than the strip-out field, although the external applied field is less than the strip-out threshold for an isolated strip, because of the stray field from nearby stripes. Therefore, this section will consider the case of an isolated stripe only.

Figure 3.19 shows an isolated stripe domain contracting under the influence of an applied field H that exceeds the strip-out or run-out threshold, H_{RO}. The stripe is in the form of an arc, with height Z and width Y. The question to be solved is the mathematical dependence of Z on H, H_{RO}, Y, and W, the width of the stripe.

Consider an isolated non-pinned stripe of length L. Let the applied normal field, H, be equal to the strip-out threshold, H_{RO}. At this field the stripe is free to contract or expand without loss of energy. However, when the bias field is raised so that it is higher than the strip-out field, the stripe contracts. When the stripe becomes shorter by a length ΔL, the energy per unit thickness changes by an amount ΔE_1:

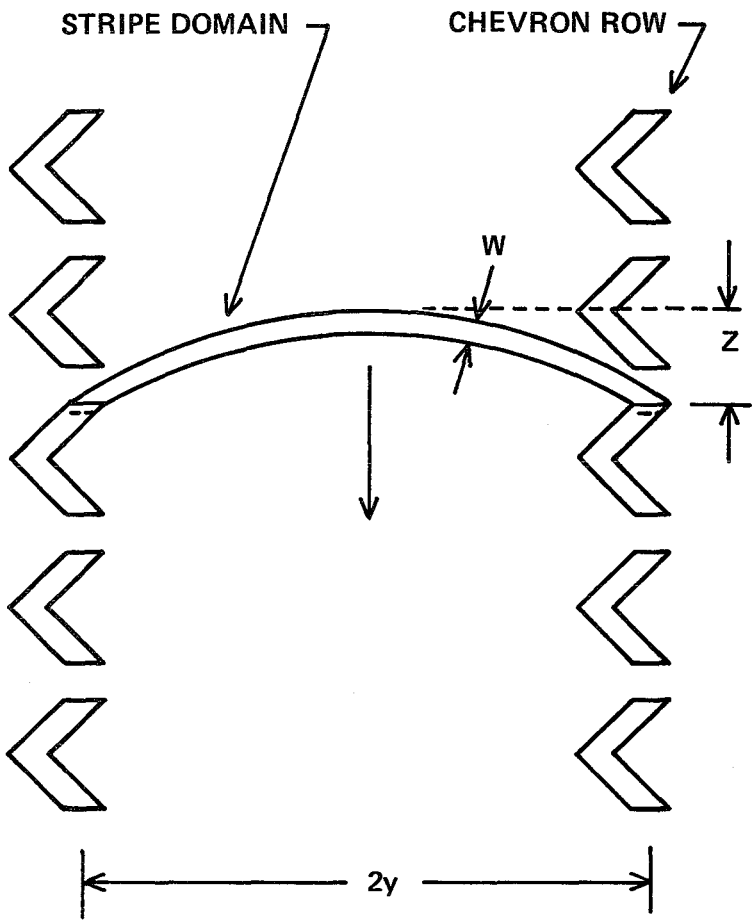

Figure 3.19 Isolated Pinned Stripe Domain Propagation by Chevron Rows.

$$\Delta E_1 = 2M\ (H-H_{RO})\ W \cdot \Delta L \qquad (3.41)$$

To determine the domain energy associated with a curved stripe, consider the case of a stripe that forms a circle, as shown in figure 3.20. When the applied normal field H exceeds the strip-out field, the radius of the circle becomes smaller. The change in energy is ΔE_2, which in analogy to equation 3.41, is given by:

$$\Delta E_2 = 2M\ (H-H_{RO})\ W \cdot (2\pi\delta R) \qquad (3.42)$$

This change in radius is resisted by the coercivity. Each moving wall of a stripe domain has to overcome the coercive field, H_c. The corresponding change in energy is ΔE_3:

$$\Delta E_3 = 2\ M\ H_c\ (2\pi r)\ \delta R \cdot 2 \qquad (3.43)$$

where the last factor of two is included because there are two walls that move. Set the two energies equal for the case of equilibrium:

$$\Delta E_2 = \Delta E_3$$

$$(H-H_{RO})\ W\ (2\pi\delta R) = H_c\ (2\pi r)\ \delta R \cdot 2$$

$$\frac{H - H_{RO}}{H_c} = \frac{2R}{W} \qquad (3.44)$$

The case of interest is that of figure 3.19, where the stripe forms an arc rather than a full circle. The radius of curvature, R, of the arc can be shown to be given by:

$$R = \frac{Y^2 + Z^2}{2Z} \ . \qquad (3.45)$$

When this is inserted into equation 3.44, the result is:

$$\frac{H - H_{RO}}{H_c} = \frac{Y^2 + Z^2}{ZW} \qquad (3.46)$$

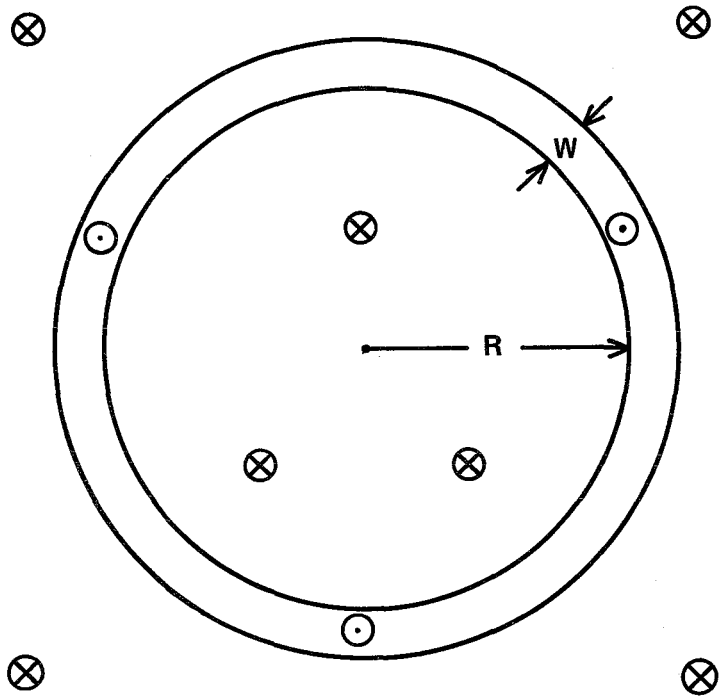

Figure 3.20 Circular Stripe Domain of Width W and Radius R, used as a Model to Calculate the Domain Energy Associated with Stripe Curvature.

Equation 3.44 or equation 3.46 relates the curvature of the stripe to the separation between chevron rows, the bias field, and the coercivity. These equations indicate that the higher the bias field, the smaller the curvature, or the larger the radius of curvature, R, or the smaller the ratio of Z to Y.

As an example, consider a garnet film with stripe width W = 3μm and a coercivity of 0.1 Oe. Let the bias field exceed the strip-out field by 10 Oe. The radius of curvature according to equation 3.44 indicates that R = 150μm. Equation 3.46 indicates that when Z = Y, they both are equal to 150μm.

As a second example, consider that the same garnet film with an applied normal rf tickle field that reduces the coercivity by a factor of 10. The radius of curvature is now 1500μm or 1.5 mm.

As a final example, suppose the chevron rows are placed 1 mm apart. In this case, Y = 500μm and Z = 86μm.

Stripe domains with pinned ends can be made to reduce their curvature by application of a normal field higher than the strip-out field. The curvature becomes much less if a tickle field is used as well. Unless the coercivity is zero the curvature will not be zero; this means that the read out track in a multilayer memory will probably have to be similarly curved.

3.5 Stripe Domain and Magnetic Feature Coupling

In order for stripes in a high Q material to be straight in a multilayer self-structured memory, they must be biased above the run-out threshold. The ends of the stripes must be pinned in order to prevent the stripes from shrinking into bubbles. One method of keeping the ends of the stripe pinned is with a permalloy strip at each end of the stripe, as shown in figure 3.21. The permalloy must supply enough normal field so that the end of the stripe is below the run-out threshold, otherwise the stripe end will shrink. The purpose of the following calculation is to determine the pinning field from a permalloy strip with no applied horizontal bias field. This field is a function of the separation, Z, between the garnet and the permalloy, as shown in figure 3.22, as well as the thickness of the garnet film, h, and the stripe wavelength.

It is assumed that the permalloy has infinite permeability for horizontal in-plane fields. This implies that the permalloy has zero anisotropy and coercivity, and that when a stripe end extends under the permalloy strip, the magnetization configuration in the permalloy sets up a stray field that, inside the permalloy, exactly cancels the horizontal component of the field from the

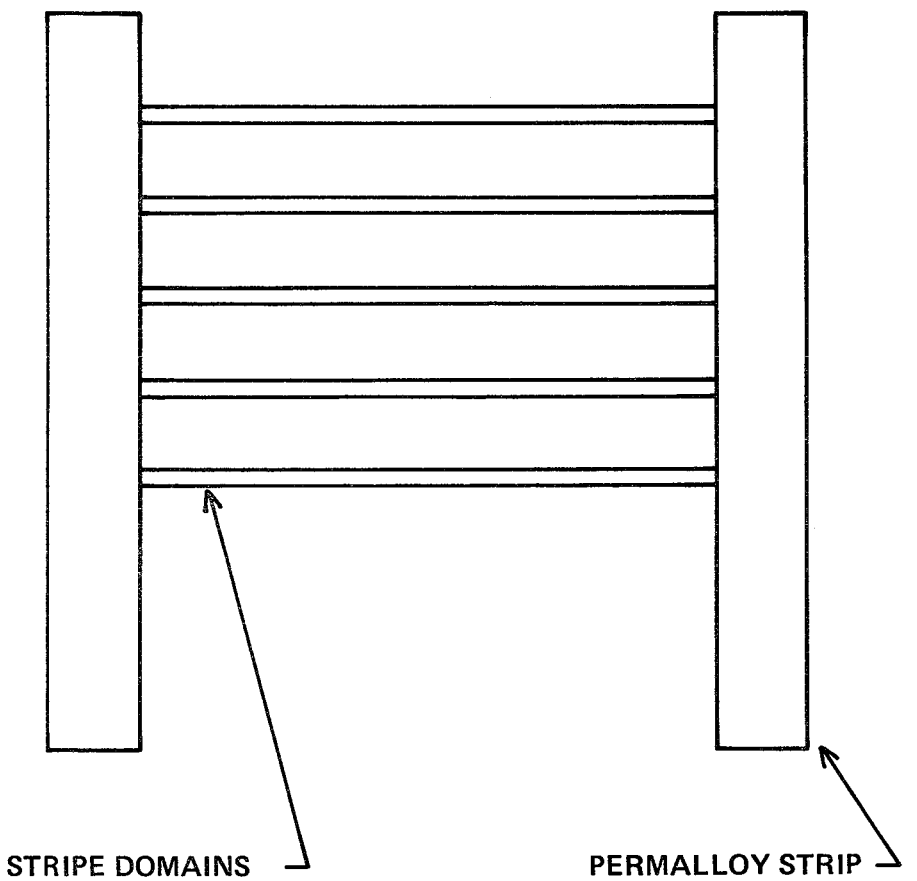

Figure 3.21 Stripe Domains with Ends Pinned by Permalloy Strips.

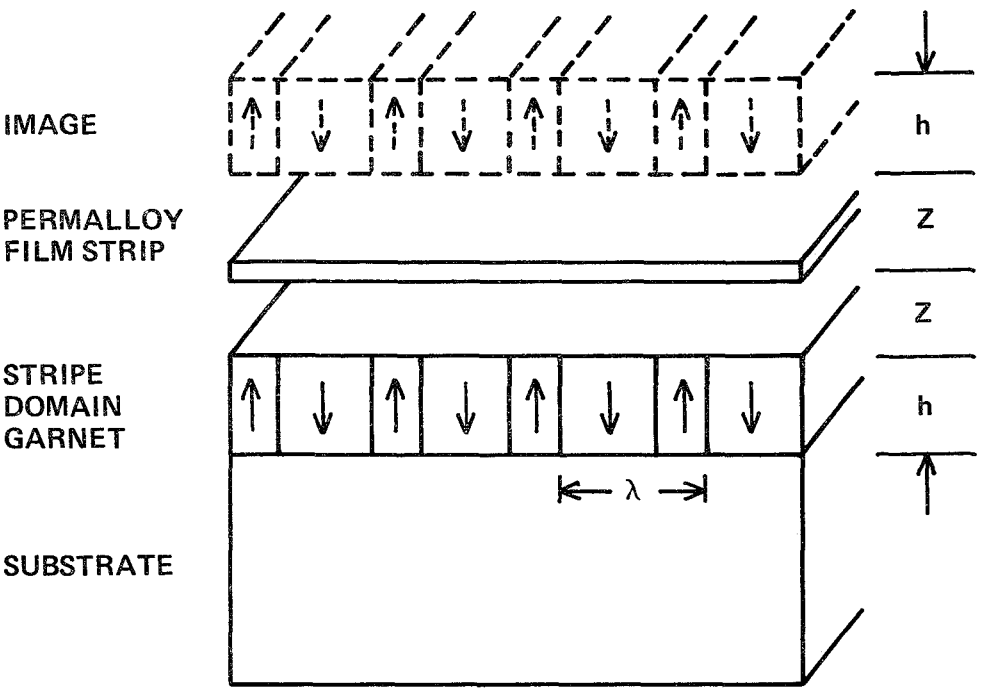

Figure 3.22 Stripe Domain Pattern and Image in a Permalloy Layer.

stripe. The normal field from the permalloy can then be calculated by the method of images. The image shown in figure 3.22 cancels out all stray fields in the plane of the permalloy film. The normal component of the stray field from the permalloy is then calculated by evaluating the normal field from the image.

The normal field from a stripe domain film having

$$M_Z(X) = \sum_{(n=o)}^{\infty} a_n M \cos \frac{2nx}{\lambda} \tag{3.47}$$

was calculated in a Sperry Univac paper presented at the 1978 Conference on Magnetism and Magnetic Materials[7].

The field H_Z from this stripe is given in equation 5 of that paper as

$$H_Z(X) = 2M \sum_{(n=1)}^{\infty} a_n \left\{ \exp \frac{(-2\pi nZ)}{\lambda} - \exp \frac{(-2\pi n(Z+h))}{\lambda} \right\} \cos \frac{2\pi nx}{\lambda} \tag{3.48}$$

where, as shown in figure 3.22, λ is the wavelength of the stripes, and h is the thickness of the stripe film. The distance from the nearest surface of the stripe film is Z.

The normal field from the image is found from equation 3.48, and by noting that the separation between film and image is 2Z. The quantity of interest is the average of the field from the image over the thickness of the stripe domain film, and provides the effective bias from the permalloy. The amplitude of this quantity, H_Z, is found by integrating equation 3.48 and suppressing the X dependence:

$$\overline{H}_Z = \sum_{n=1}^{\infty} \frac{a_n \lambda M}{nh} \left\{ \exp\left(\frac{-4\pi nZ}{\lambda}\right) - 2\exp\left(-4\pi n \frac{(Z + h/2)}{\lambda}\right) + \exp\left(\frac{-4\pi n(Z+h)}{\lambda}\right) \right\} \tag{3.49}$$

3.5.1 Symmetric Stripe Domains

Equation 3.49 is plotted in figure 3.23 for the case $a_1 = 1$ and $a_n = 0$ for $n > 1$. This is the case of symmetrical stripe domains in which the Z component of magnetization varies sinusoidally as a function of distance in the film plane: $M_Z(X) = M \sin 2\pi x/\lambda$.

The physical meaning of $\bar{H}_Z$ is: when the normal bias field is raised above the run-out threshold, all unpinned stripes contract to bubbles. Stripes that are pinned at the ends by the two permalloy stripes do not pull loose and contract to bubbles until the bias field is raised by a value equal to $\bar{H}_Z$ above the run-out threshold. At this point the total field under the stripe, the sum of the field from the permalloy and the bias field, equals the run-out threshold. This is how $\bar{H}_Z$ is measured experimentally.

Figure 3.23 shows several interesting and important relationships:

(1) The pinning field from a permalloy strip, with no in-plane bias, can be as large as 2.55M, where M is the magnetization of the stripe containing garnet. For example, if $4\pi M$ is 200 Oe, then $\bar{H}_Z$ can be as high as 41 Oe.

(2) It is important that the space, A, between the permalloy and the top of the garnet be as small as possible. For example, if $\lambda = 10\mu m$, Z is $1\mu m$, and h = $2\mu m$; then $\bar{H}_Z$ is only 12 Oe instead of 41 Oe, as it would be if Z = 0.

(3) The maximum value of $\bar{H}_Z$ occurs when $h/\lambda = 0.2$. If the film is thicker, $\bar{H}_Z$ is smaller because $\bar{H}_Z$ is the average H_Z over the whole film thickness. If the film is thinner, then $\bar{H}_Z$ is smaller because H_Z is smaller for the same reason as that the electric field outside a parallel plate capacitor is nearly zero.

3.5.2 Asymmetric Stripe Domains

When a normal field is applied to an array of stripes, they become asymmetric, i.e., the even numbered stripes have a different width than the odd numbered stripes. This case is treated mathematically by first finding the Fourier components of the asymmetric magnetization distribution to fit in equation 3.47. These are then inserted into equation 3.49 to yield $\bar{H}_Z$.

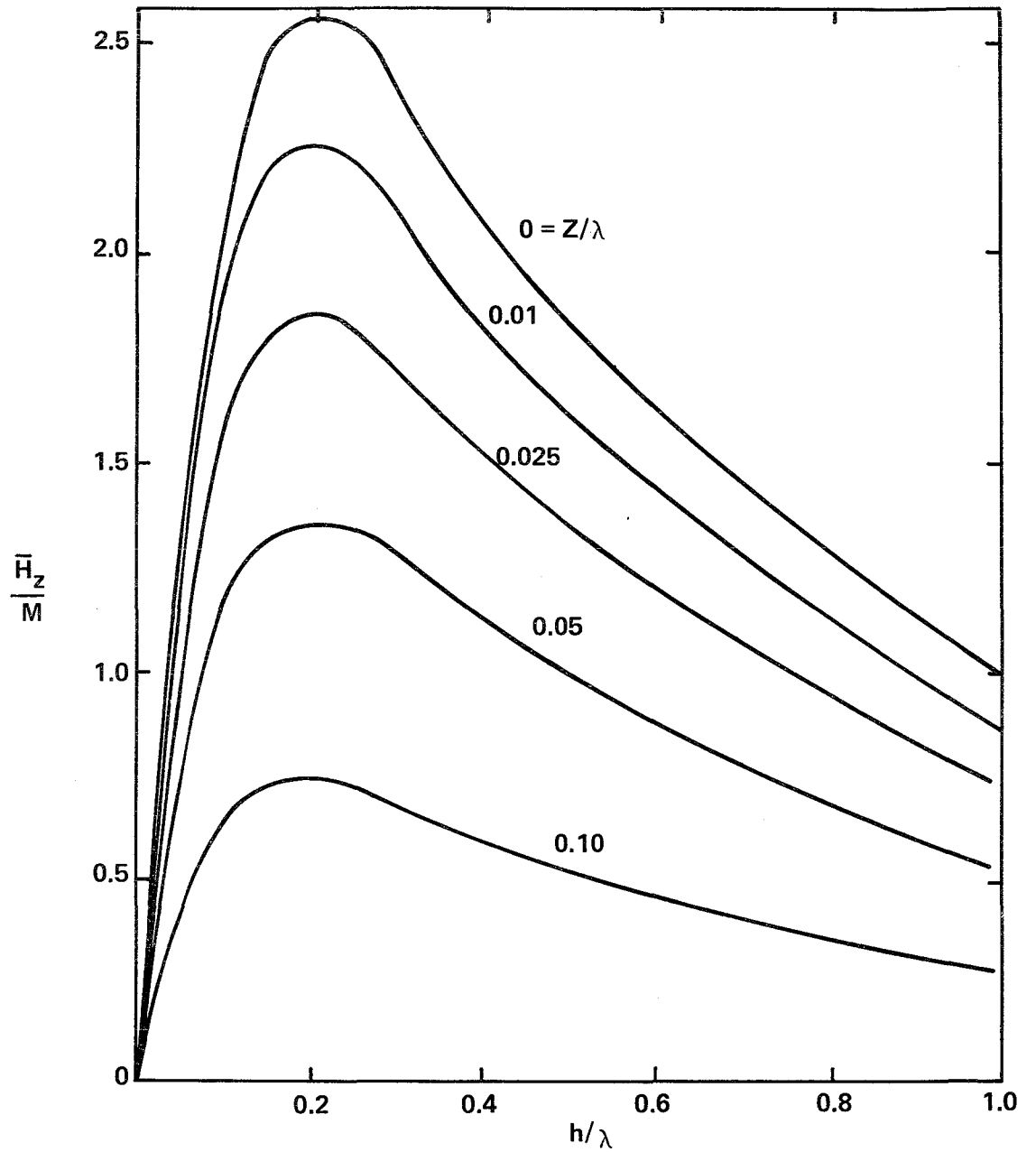

Figure 3.23 Field from a Permalloy Layer Covering an Array of Stripes, as a Function of Garnet Thickness h, Stripe Wavelength λ, and Permalloy to Garnet Spacing Z.

As an example, consider the case in which the stripes are biased so that the width of the odd numbered stripes is $\lambda/4$ and the width of the even numbered stripes is $3\lambda/4$. This is illustrated in figure 3.24. The Fourier components of the magnetization are:

$$a_n = \frac{2}{\pi n} \sin \frac{2\pi n x}{\lambda} \qquad (n \geq 1) \qquad (3.50)$$

The zeroth term does not contribute to $\bar{H}_Z$. Equation 3.50 is inserted into equation 3.49 to yield H_Z. In the case that Z = 0 and $h/\lambda = 0.2$, yielding $H_Z = 1.88$ M. This is lower than the 2.55 M of the symmetric case. The following are numerical examples:

(1) $\lambda = 16\mu m$, $4\pi M = 200$ Oe, Z = 0, h = 3.2μm, stripe width = $\lambda/4$. Then $H_Z = 30$ Oe. This is a case of zero separation between the garnet and permalloy.

(2) $\lambda = 16\mu m$, $4\pi M = 200$ Oe, Z = 0.16μm, h = 3.2μm, stripe width = $\lambda/4$. Then $H_Z = 25.6$ Oe. This is a case of very small separation between the garnet and permalloy.

(3) $\lambda = 16\mu m$, $4\pi M = 200$ Oe, Z = 1.6μm, h = 3.2μm, stripe width = $\lambda/4$. Then $H_Z = 6.15$ Oe. This is a case of large separation between the permalloy and garnet. Here the higher a_n terms in equation 3.50 do not contribute.

(4) $\lambda = 16\mu m$, $4\pi M = 600$ Oe, Z = 1.6μm, h = 3.2μm, stripe width = $\lambda/4$. Then $H_Z = 18.4$ Oe. This is the same as case 3, except that $4\pi M$ has been increased by a factor of three.

(5) $\lambda = 4\mu m$, $4\pi M = 200$ Oe, Z = 0, h = 3.2μm, stripe width = 1μm, then $H_Z = 15$ Oe. This is a case of very high density stripes.

3.6 Bistability of Bubbles in Double Epi-Layer Films

The following investigation was performed to determine if double and single bubbles in exchange coupled layers can be used to store data in bubble lattices in general, and in self-structured bubble lattice files in general.

The first step was a literature search. Exchange coupled layers had been studied by other scientists for self-biasing or as an alternative to ion implantation for the prevention of hard

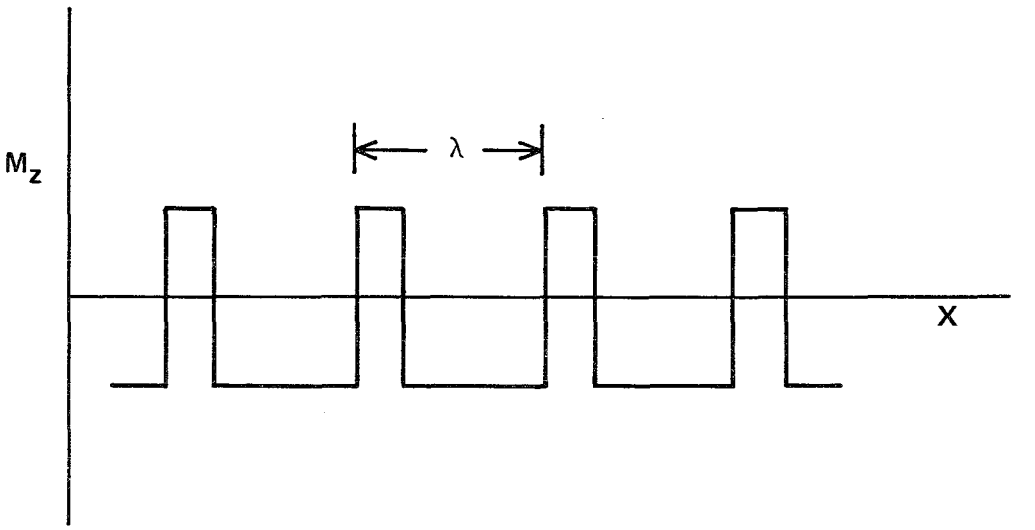

Figure 3.24 Asymmetric Magnetization Distribution in Strips with Stripe Width λ/4.

bubbles, but not for a bubble lattice. No one had even investigated whether half-bubbles (i.e., bubbles in the top layer only) were stable at the same bias field as full bubbles (i.e., bubbles that extend through both layers). Because our previous work was done in triple epi-layer films in which the top and bottom films are magnetostatically coupled through a nonmagnetic separation layer, we sometimes call half and full bubbles, respectively.

The second step was a preliminary calculation that showed that for half bubbles and full bubbles to be stable at the same bias, the buried layer should have a $4\pi M$ that is approximately half that of the outer layer.

The third step was to actually fabricate exchange coupled films. The first films were made under poorly controlled conditions and exhibited widely diverse behavior. Some films exhibited double bubble behavior; some did not. Some of the former had double and single bubbles simultaneously stable; others did not. However, one fascinating and potentially valuable phenomenon was observed; while most of the films that exhibited both double and single bubbles had double bubbles that were large and had more Faraday rotation than single bubbles, some films had, over a certain bias range, double bubbles that had the same size and nearly the same Faraday rotation as single bubbles, and were distinguishable from single bubbles only by lowering the bias field past a certain threshold below which the double bubble would become larger than the single bubble and have a higher Faraday rotation. There are real advantages in having all bubbles in a lattice the same size. Interactions between bubbles in a lattice are extremely important; it is the uniformity of such interactions in a lattice that allow the four-fold increase in density over conventional schemes. Therefore, an understanding of this phenomenon is desirable.

The fourth step was a theoretical study aimed at understanding this bubble behavior. To do this the forces on the capping wall of the half bubble were calculated. This effort was done in three stages. The first stage was the calculation of the equation of a capping wall and its energy. The second was the calculation of the force needed to move a capping wall past the boundary between two exchange coupled films. The third stage was the calculation of the hysteresis loop for a bubble in exchange coupled films. For this the magnetostatic forces on the capping wall from the stray field of the bubble and from the boundary between the two layers of different $4\pi M$ had to be calculated, and the variation in bubble diameter had to be taken into account. The result was the discovery that the desired behavior, in which bubbles are stable with the capping wall on either side of the boundary, occurs when the buried layer has both lower $4\pi M$ and higher anisotropy than the

outer layer. There is an energy barrier that tends to prevent the capping wall from passing through the boundary from either direction. Magnetostatic forces repel a capping wall in the buried layer from the boundary, and wall energy increase repels a capping wall in the outer layer from traversing the boundary. The result is that double and single bubbles look the same under the microscope. One has the capping wall in the buried layer, the other in the outer layer. This makes a uniform, compact lattice. Only when the bias field is lowered past a certain threshold, the double bubbles become large and run out into double stripes.

As a result of these calculations, the crystal growing procedure was changed such that the anisotropy of the buried layer was made larger than that of the outer layer. The result was a set of films suitable for device applications, and a set of test vehicles was fabricated on them. See Section 6 for test results.

3.6.1 Switching Mechanism

Figure 3.25 shows two cases in which there is a bubble in layer 1 and no bubble in layer 2. Figure 3.25a the capping wall lies entirely in layer 1, while in Figure 3.25b the capping layer lies entirely in layer 2. If the capping wall energy is lower in layer 1, the wall will lie in layer 1. If the wall has lower energy in layer 2, it will lie there. If the wall lies in layer 2, it can bulge out as shown in Figure 3.26 due to the nonuniform magnetic stray field from the bubble in layer 1. This mechanism can cause a gradual transition from the single bubble state to the double bubble state. This transition can be smooth and reversible without hysteresis. If this is the case, single and double bubbles cannot exist simultaneously. Therefore, it is important to have the capping wall in layer 1, and for this to be true, the wall energy in layer 1 must be less than the wall energy in layer 2.

3.6.2 Capping Wall Energy

There are three components to the energy of the capping wall: the exchange energy, the anisotropy energy, and the magnetostatic energy. Let ϕ be the angle between the local magnetization vector and the easy axis as shown in Figure 3.27. The exchange energy density is:

$$E_{ex} = A \left(\frac{d\phi}{dz} \right)^2 . \qquad (3.51)$$

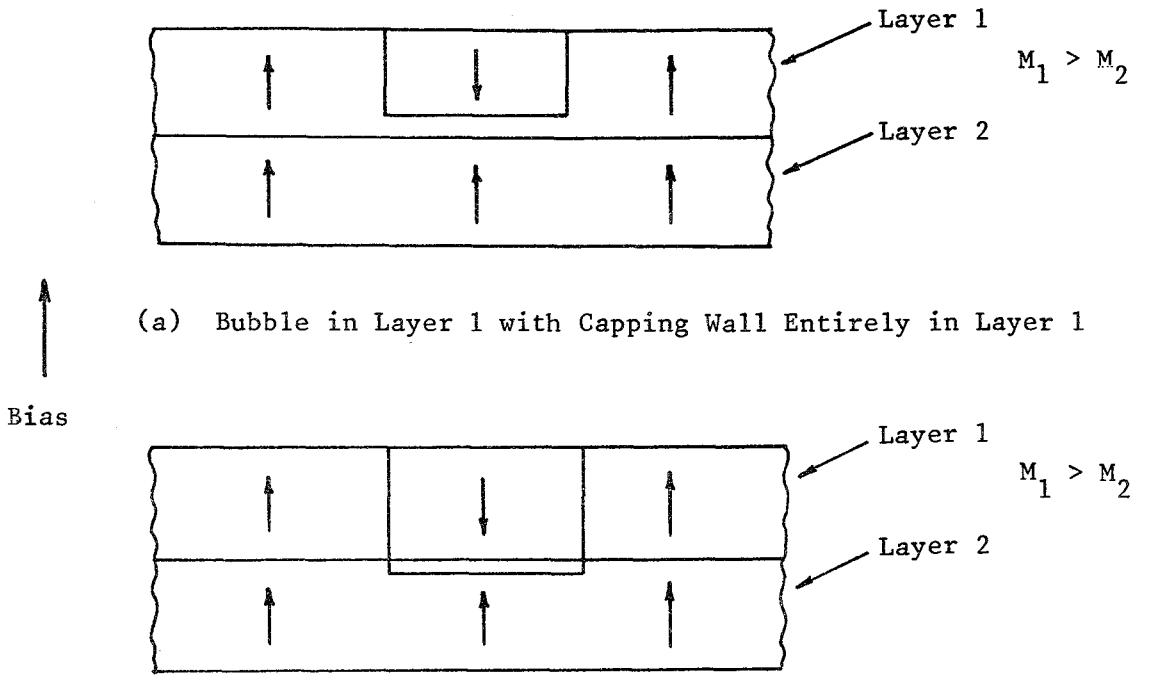

(a) Bubble in Layer 1 with Capping Wall Entirely in Layer 1

(b) Bubble in Layer 1 with Capping Wall Entirely in Layer 2

Figure 3.25 Bubbles in Layer 1 and Not in Layer 2.

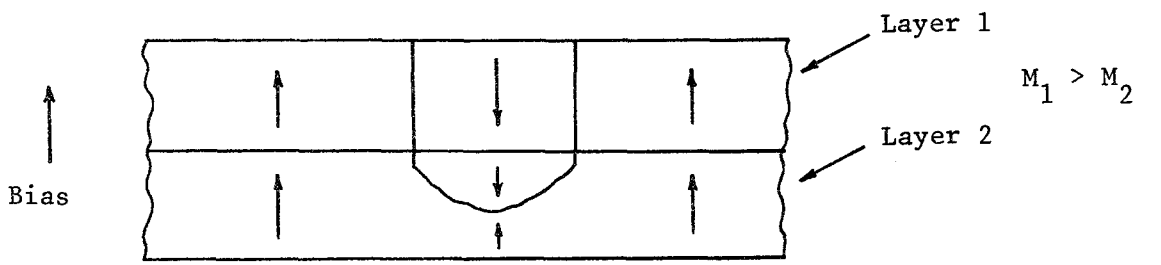

Figure 3.26 Bulge in the Capping Layer.

where A is the exchange constant. The anisotropy energy is

$$E_k = \tfrac{1}{2}MH_k\sin^2\phi \qquad (3.52)$$

where M is the magnetization and H_k is the anisotropy field.

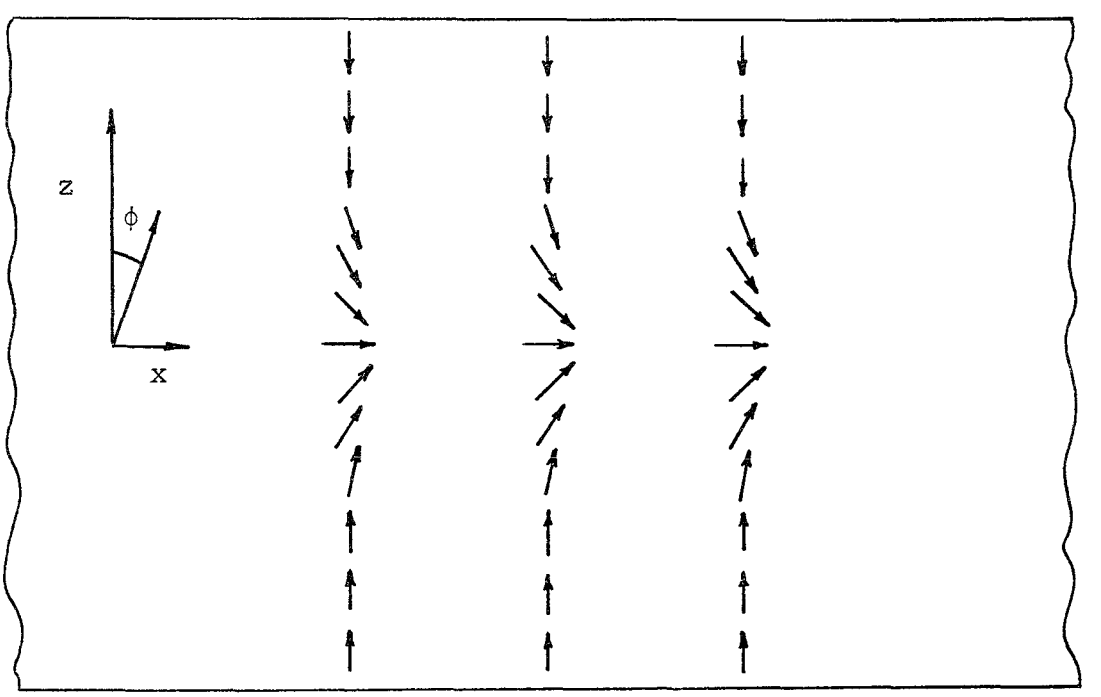

Figure 3.27 Magnetization in a Capping Wall.

If the bubble diameter is assumed much larger than the film thickness, the stray field is:

$$H_s = 4\pi M \cos \phi$$

and the stray field energy is:

$$E_s = 2\pi M^2 \cos^2 \phi \, . \tag{3.53}$$

The static torque equation is found by setting the variation of the total wall energy with respect to ϕ equal to zero:

$$0 = -2A \left(\frac{d^2\phi}{dZ^2} \right) + MH_k \sin \phi \cos \phi - 4\pi M^2 \cos \phi \sin \phi \, . \tag{3.54}$$

If one multiplies each term in the above equation by $d\phi/dZ$ and integrates with respect to Z, the solution is:

$$\phi = 2 \arctan \exp \left\{ - \sqrt{\frac{M(H_k - 4\pi M)}{2A}} \; Z \right\} . \tag{3.55}$$

The total wall energy is found by integrating each of the energy terms, equations 3.51, 3.52, and 3.53 over all Z. The sum of the anisotropy energy and the stray field energy is equal to the exchange energy. Thus, the total wall energy per unit area is:

$$E_w = 2 \int_{-\infty}^{+\infty} A \left(\frac{d\phi}{dZ} \right)^2 dZ = 2 \int_{-\pi}^{0} A \left(\frac{d\phi}{dZ} \right) d\phi \tag{3.56}$$

$$E_w = 2 \sqrt{2AM(H_k - 4\pi M)} \, . \tag{3.57}$$

This is the expression we wanted to derive. Plots of E_w versus M and H_k are given in Figure 3.28.

Discussion - The films of interest for us have the magnetization in layer 1 about twice the magnetization in layer 2. If the H_k is the same in both layers, then bistable bubbles will exist if:

$$\frac{M_1 + M_2}{2} > \frac{H_k}{8\pi} . \tag{3.58}$$

The anisotropy fields of the two layers are in general different. The exchange constant is most likely the same in both layers. Thus, the general criteria for simultaneous stability of single and double bubbles is:

$$M_1 (H_{k_1} - 4\pi M_1) < M_2 (H_{k_2} - 4\pi M_2). \tag{3.59}$$

3.6.3 Coercive Force at the Boundary Between Two Exchange Coupled Layers

In this section the actual field needed to move a wall past the boundary between two exchange coupled layers is calculated. This field may be required for movement in only one direction, or it may be required for movement in both directions. The field will be calculated by setting up the micromagnetic differential equations for the magnetization on both sides of the boundary and finding the field, H, required to join the solution smoothly at the boundary for a given value of ϕ at the boundary.

Consider a cylindrical sample of radius r and length L>>r as shown in Figure 3.29. The magnetization M_1 in region 1 is shown to be larger than M_2, the magnetization in region 2. The angle between the magnetization and the positive Z axis is ϕ (Z). Assume that the wall is parallel to the X axis, i.e., that $d\phi/dx = 0$, and that the wall is near the boundary, i.e., Z<<r. Also assume that the ends of the cylinder are far away compared to the radius, so that the field from the ends can be neglected. This assumption does not change the coercive force due to the boundary; for example, in the case of a bubble in an exchange coupled film, the field from the ends changes only the bias field, not the coercivity due to the interface between the exchange coupled layers.

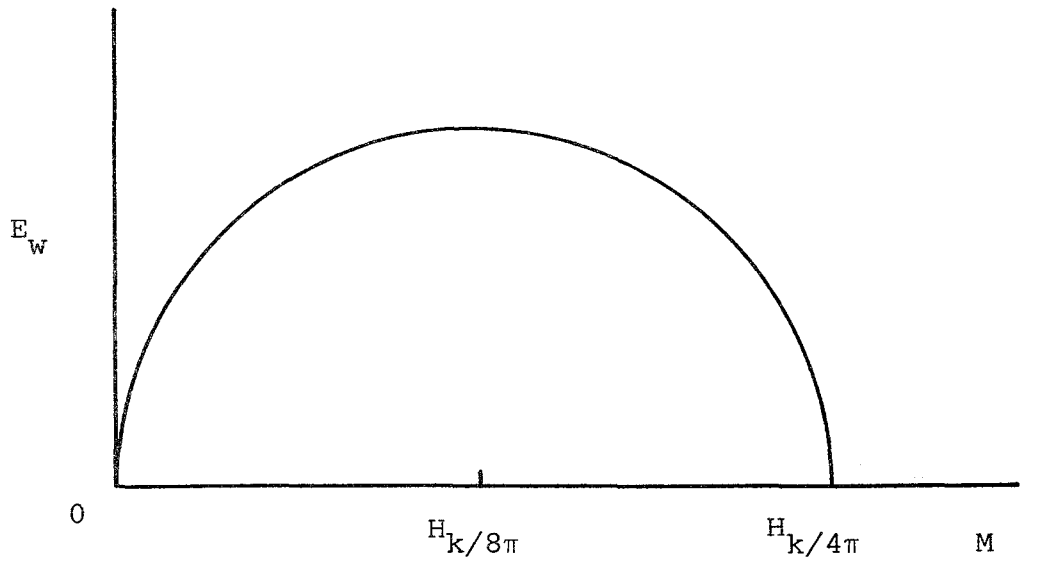

Figure 3.28a Wall Energy E_w as a Function of the Magnetization with H_k Constant.

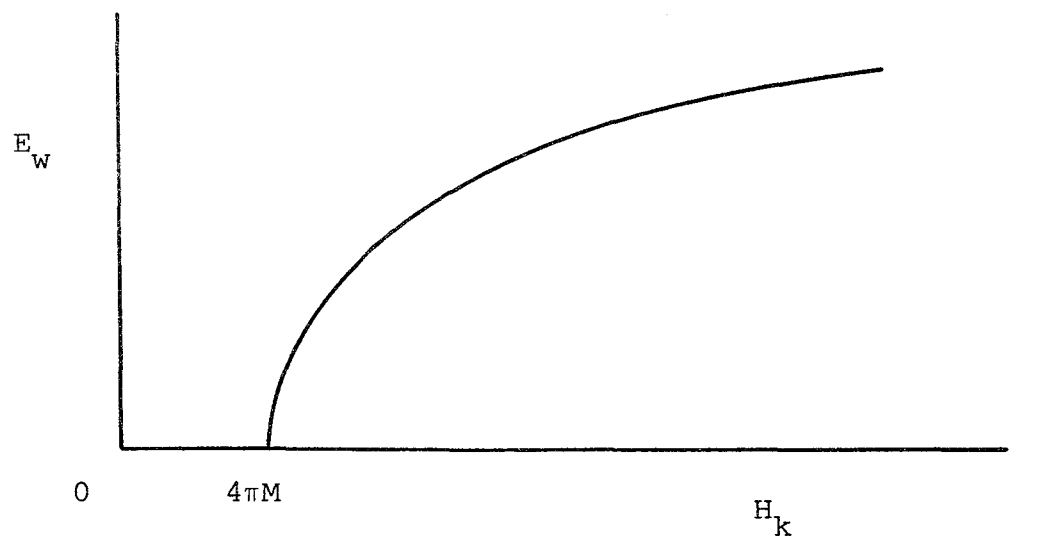

Figure 3.28b Wall Energy E_w as a Function of the Anisotropy Field H_k with M Constant.

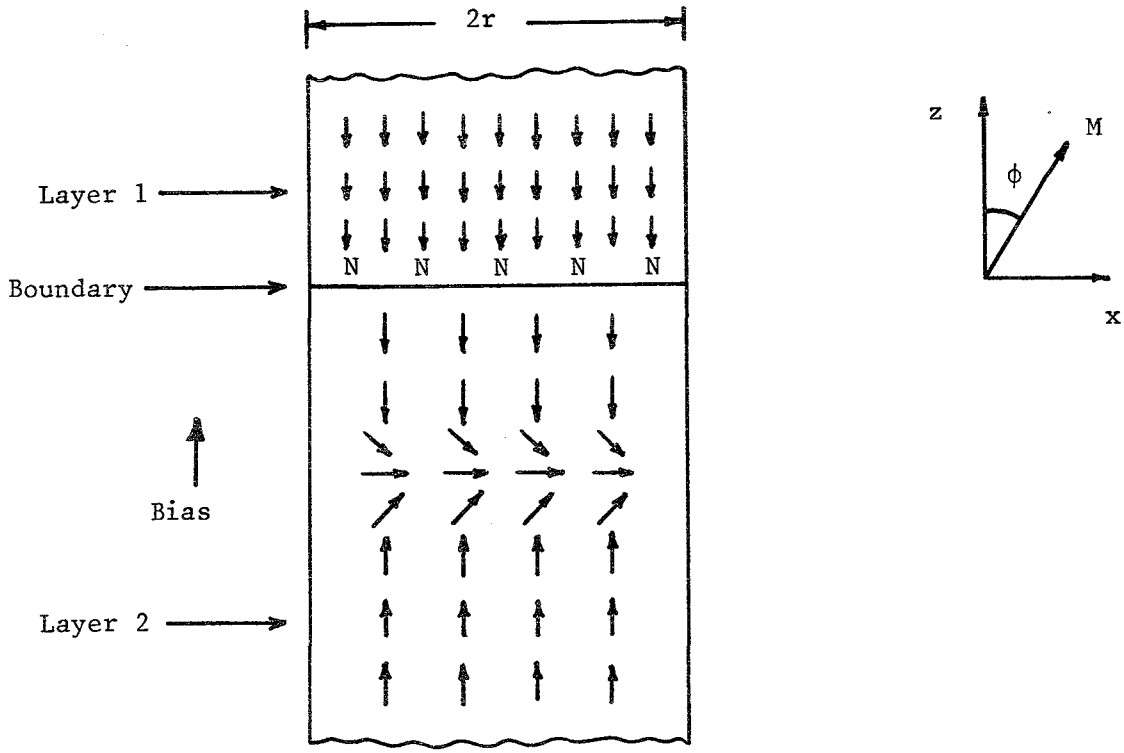

Figure 3.29 Wall in a Cylindrical Sample with Two Exchange Coupled Layers Having Different $4\pi M$

The stray field H_s in region 2 can most easily be found by considering the magnetization in region 1 to be a superposition of $\vec{M}_2$ and $\vec{M}_1-\vec{M}_2$.

In region 2:

$$H_s = -4\pi M_2 \cos\phi(Z) - 2\pi(M_1 - M_2) . \qquad (3.60)$$

In region 1:

$$H_s = -4\pi M_1 \cos\phi(Z) - 2\pi(M_1 - M_2) . \qquad (3.61)$$

Note that if $\cos\phi(0) = 0$, there is a discontinuity in the stray field at the interface between region 1 and region 2.

The differential equation is found by setting the sum of the torques to zero: the anisotropy torque $H_k M \sin\phi \cos\phi$, the stray field torque $MH_s \sin\phi$, the Z axis applied field torque $MH \sin\phi$, and the exchange torque $- 2A(d^2\phi/dZ^2)$.

Requiring $\cos\phi = -1$ when z goes to infinity in region 1, and that $\cos\phi = 1$ and $(d\phi/dz)^2 = 0$ when z goes to infinity in region 2, and requiring that $d\phi/dz$ be continuous at the interface, results in:

$$H = \frac{1/2[M_1(H_{k_1} - 4\pi M_1) - M_2(H_{k_2} - 4\pi M_2)]}{(M_1 - M_2)\cos\phi(0) + (M_1 + M_2)} \sin^2\phi(0)$$

$$+ 2\pi(M_1 - M_2) . \qquad (3.62)$$

The first term is proportional to the difference of the squares of the wall energy in region 1 and region 2. The second term is a magnetostatic term due to the discontinuity of the magnetization at the interface.

Consider several examples:

Case 1: $M_1 = M_2$, $H_{k_1} \neq H_{k_2}$

When the magnetization in region 1 is equal to that in region 2, equation (3.62) reduces to:

$$H = \left(\frac{H_{k_1} - H_{k_2}}{4}\right) \sin^2\phi(0) . \qquad (3.63)$$

The maximum H required occurs when $\sin^2\phi(0)$ is 1, i.e., when the middle of the wall is exactly at the interface. This corresponds to a unidirectional coercivity.

Case 2: $H_{k_1} = H_{k_2}$, $M_1 > M_2$

The maximum H required does not occur when $\cos \phi(0) = 0$ as in case 1, but when $\cos \phi(0) \simeq 1/2\ (M_1 - M_2) / (M_1 + M_2)$. However, for cases of interest ($M_1 \leq 2M_2$) the maximum field is very close (within 3 percent) to the case where $\cos \phi = 0$. With $\cos \phi = 0$, equation (3.62) becomes:

$$H = \left[\frac{(M_1 - M_2)}{(M_1 + M_2)} H_k - 4\pi(M_1 - M_2) \right] \sin^2 \phi(0) + 2\pi(M_1 - M_2) \ . \qquad (3.64)$$

Discussion

Equation 3.62 gives the field required to move a domain wall through the interface between two exchange coupled garnets. There are two terms in equation 3.62: The first term, the coefficient of $\sin^2 \phi\ (0)$, is proportional to the difference of the squares of the wall energy in the two garnets. This term always tends to push the wall from the high wall-energy region into the low wall-energy region. Thus, this term is unidirectional and acts to retard the wall only when the wall is going in one direction. Also, this term is nonzero only when the wall is actually touching the interface. It is largest when the interface is approximately at the wall center.

The second term is purely magnetostatic in nature, and comes from the poles on the surface of the interface. This field is also unidirectional, tending to push the wall in only one direction. Unlike the first term, the second term is nonzero when the wall is not touching the interface.

In this derivation we assumed that the wall was close to the interface so that the field from the poles on the interface is $2\pi(M_1 - M_2)$. However, if the wall is farther away from the interface, the field from those poles is diminished. The second term should be replaced as follows:

$$2\pi(M_1 - M_2) \rightarrow 2\pi(M_1 - M_2)\ (1 - \cos \theta)$$

where $\theta = \arctan \left| r/Z \right|$ and r is the radius of the cylinder.

Thus, both the first term and the second are unidirectional, retarding wall motion in only one direction. One can arrange to have the first term impede wall motion in one direction and the second term impede wall motion in the other direction. This arrangement will have hysteresis even in minor loops.

3.6.4 Bubble Domain in Exchange Coupled Layers

Figure 3.26 shows a bubble domain in an exchange coupled garnet pair of total thickness L. The cap of the bubble is experimentally observed to be in the interior of the layer over a range of bias field. It is the purpose of this section to calculate the position, Z, of the domain tip as a function of bias field.

Let H_{tip} be the stray field at the tip of the bubble. To calculate H_{tip}, use the usual trick of superposing twice the magnetization in the bubble with the magnetization of the saturated films. The field from the poles on the surfaces of the bubbles is found by integration, and is proportional to the solid angle $2\pi(1 - \cos\theta)$ subtended by the horizontal bubble surfaces. H_{tip} is given by:

$$H_{tip} = \begin{cases} 4\pi(M_1 - M_2)\cos\theta_2 - 4\pi M_1 \cos\theta_1 & (Z < 0) \\ -4\pi M_1 \cos\theta_1 & (Z > 0) \end{cases} \tag{3.65}$$

where $\theta_1 = \arctan\left|\frac{r}{\frac{1}{2}L - Z}\right|$ and $\theta_2 = \arctan\left|\frac{r}{Z}\right|$.

There is also a "wall field" due to the energy of the vertical wall of the bubble. The tendency for this wall to save energy by shortening the length of the bubble is proportional to the wall energy, σ, and the circumference of the bubble. The "wall field," H_σ, is given by:

$$H_\sigma = \frac{\sigma_w}{rM} = \frac{4\pi M\ell}{r} . \tag{3.66}$$

The position of the domain tip is given by the equation:

$$H_{bias} + H_{tip} + H_\sigma = 0 . \tag{3.67}$$

There is a second kind of "wall field," $H_{\sigma'}$, which is important when a domain in layer 1 runs out. There is an increase in energy due to the lengthening of the capping wall when the strip runs out. This second kind of wall field is given by:

$$H_{\sigma'} = \frac{\sigma'_w}{rM} = \frac{4\pi M \ell}{r} . \tag{3.66}$$

The position of the domain tip is given by the equation:

$$H_{bias} + H_{tip} + H_{\sigma} = 0 . \tag{3.67}$$

There is a second kind of "wall field," H_{σ} which is important when a domain in layer 1 runs out. There is an increase in energy due to the lengthening of the capping wall when the strip runs out. This second kind of wall field is given by:

$$H_{\sigma'} = \frac{\sigma'}{2Mh} \simeq \frac{4\pi M \ell}{2h} \tag{3.68}$$

where σ' is the energy of the capping wall, h is the thickness of layer 1, and ℓ is the characteristic length. Because the energy of the capping wall, given by equation 3.57 as $2\sqrt{2AM(H_k - 4\pi M)}$, is different from the energy of the wall of the cylindrical side of the bubble, $2\sqrt{2AMH_k}$, σ' is only approximately equal to σ.

Consider the example where layer 1 and layer 2 have the following properties:

	LAYER	
	1	2
$4\pi M$	120 Oe	80 Oe
H_k	600 Oe	1000 Oe
ℓ	0.2704 μm	0.7854 μm
h	5 μm	5 μm
λ	0.0541	0.1571
$(r_{RO})_{FREE}$	2.4 μm	5.6 μm
$(r_o)_{FREE}$	0.835 μm	1.75 μm
$(H_o)_{FREE}$	75 Oe	33.6 Oe
$(H_{RO})_{FREE}$	62.4 Oe	26.4 Oe

Here the subscript "FREE" indicates the value when the layer is isolated, not coupled to another layer. The subscript "o" indicates collapse, the subscript "RO" indicates run-out. All these quantities have been calculated from the standard bubble equations given M, H_k, and h.

When there is a double bubble, i.e., a cylindrical domain extending through layers 1 and 2, the properties might be assumed to be those of a bubble in a single layer whose thickness is the sum of h_1 and h_2 and whose $4\pi M$ is the average of that in layers 1 and 2, and whose characteristic length is the average of that of layers 1 and 2. The characteristics of that double bubble can be calculated from the usual equations: $\bar{\ell}$ = .5275 μm, h = 10 μm, $\bar{\lambda}$ = .05275, $\bar{M}$ = 100 Oe, $\bar{H}_{RO}$ = 52.7 Oe, $\bar{H}_o$ = 64 Oe, $\bar{r}_o$ = 1.63 μm, and $\bar{r}_{RO}$ = 4.6 μm.

Now calculate the position, Z, of the domain tip as a function of bias field, as illustrated in Figure 3.30. Start with the bubble extending completely through both films, as shown in Figure 3.30, and calculate the field required to just barely lift the domain cap from the bottom surface of layer 2.

Field to pull dome from bottom of layer 2 - To calculate this quantity, the radius of the bubble must be known. Assume this radius is the average between the run-out radius and collapse radius of the double bubble, i.e., $\bar{r}$ = 3.1 μm.

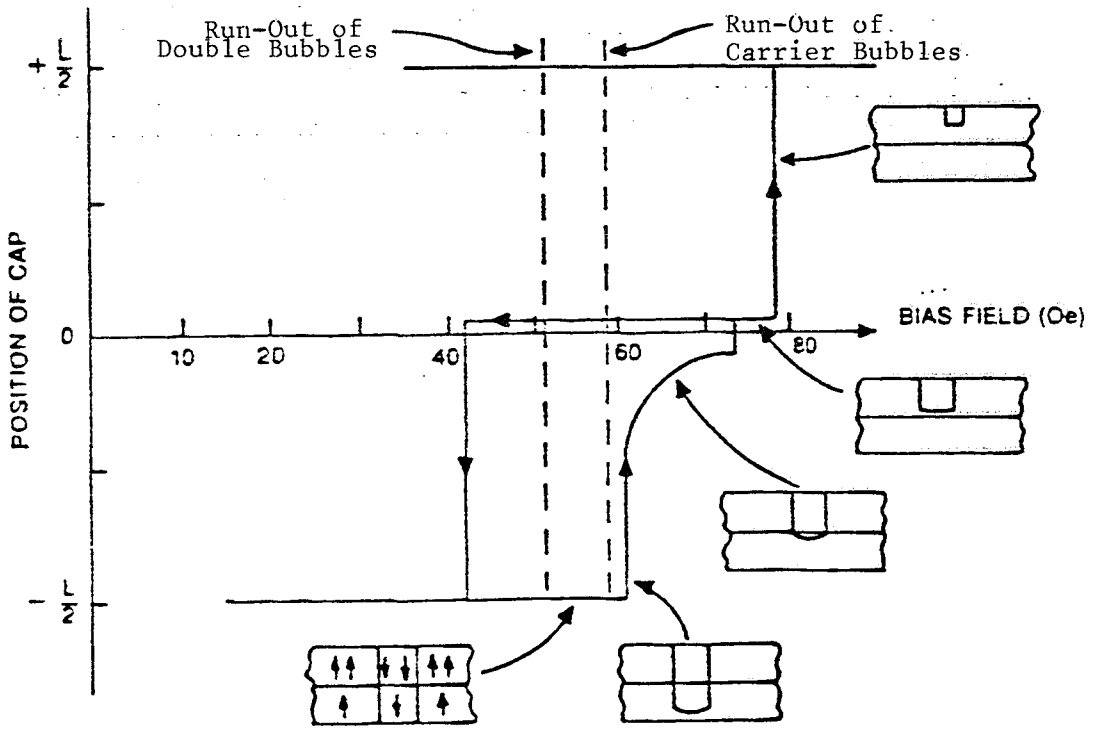

Figure 3.30 Hysteresis in Exchange Coupled Garnet Layers.

$$H = -H_{tip} - H_{\sigma 2}$$

$$= 80.6 - 20.2 = 60.4 \text{ Oe}.$$

Field to pull dome to top of layer 2 - As the bias field is increased, the bubble radius decreases and the dome rises very rapidly, then slowly as the dome nears the interface between layer 1 and layer 2. The domain wall is repelled by the poles on the surface of the interface, and the repelling force becomes greater as the dome nears the interface. Just before the dome breaks through the interface, the bias field is given by:

$$H = -H_{tip} - H_{\sigma 2}$$

$$= 114.9 - 41.8 = 73 \text{ Oe}.$$

Here the value of the bubble radius is assumed to be 1.5 μm, slightly less than the average between r_o and r_{RO} for layer 1.

Field to pull dome from bottom of layer 1 - As soon as the capping wall enters layer 1, there is a decrease in wall energy. This causes an abrupt decrease in H_σ, the "wall field." Consequently, the domain cap does not continue upward, but remains stable in layer 1 until the bias field is increased enough to offset the decrease in "wall field." The capping wall then travels to the top surface of layer 1, erasing the bubble. The radius at this threshold is assumed to be the collapse radius of layer 1, $r_o = 0.835$ μm. The erase field is:

$$H = -H_{tip} - H_{\sigma 1}$$

$$= 118.4 - 38.9 = 79.5 \text{ Oe}.$$

Field to push the capping wall from layer 1 to layer 2 - If instead of erasing the bubble wholly contained in layer 1, we lower the bias field, we can push the capping wall back across the interface into layer 2. Because the capping wall has higher energy in layer 2, there is a barrier to overcome. The amount the bias field must be lowered to overcome this barrier is given by the first term of equation 3.62:

$$H_{barrier} = \frac{M_1 (H_{k_1} - 4\pi M_1) - M_2 (H_{k_2} - 4\pi M_2)}{2(M_1 + M_2)} \qquad (3.69)$$

$$= -40 \text{ Oe} .$$

Thus, the field at which the cap traverses the interface from layer 1 to layer 2 is given by:

$$H = -H_{tip} - H_{\sigma 2} + H_{barrier}$$

$$= 108.1 - 26.2 - 40 = 41.9 \text{ Oe} .$$

Here we have used r = 2.4μm, which is the radius for run-out in layer 1. Actually, this field is below the run-out threshold for a bubble wholly in layer 1.

Run-out threshold for a bubble completely in layer 1 - The run-out threshold for a bubble with cap in layer 1 is not the same as that if the cap were not there. It takes extra energy to lengthen the cap. The difference in field is the second kind of "wall field" given by equation 3.68. Thus, the run-out threshold is:

$$H_{RO} = (H_{RO})_{FREE} - H_{\sigma}' \qquad (3.70)$$

$$= 62.4 - 3.2 = 59.2 \text{ Oe} .$$

The run-out threshold of the double bubble was calculated earlier in this section to be 52.7 Oe.

3.6.5 Conclusions

A theoretical and experimental study has been performed that demonstrates that data can be stored in a bubble lattice in exchange coupled films. The double and single bubbles have the same size, resulting in a uniform lattice. Data is read out by lowering the bias past a threshold at which the double bubble runs out into a double stripe. Theoretical and experimental hysteresis loops agree. Exchange coupled films appear better than the triple epi-layer films formerly considered for the NASA-sponsored effort toward a 10^7 bit/chip current access structured 1.5 Mbit/sec bubble memory.

3.7 Summary and Conclusions of Theoretical Studies

The preceding diverse theoretical studies in this section give information necessary for the design of test circuits and infomation about the behavior of various multilayer devices.

The interaction between bubbles in one layer and stripes or bubbles in another layer was calculated for various geometries. Coupling is found to be sufficient between stripes in one layer and bubbles in another so that moving stripes will cause the bubbles to move along with them. This is true for both magnetostatic and exchange couping, and even when the stripes are much narrower than the bubbles.

Explicit expressions were derived for the change in run-out threshold due to changes in any of the following parameters: thickness, magnetization, characteristic length, anisotropy field, and exchange constant. It was shown that these parameters can be adjusted so that there are large carrier bubbles in one layer magnetostatically coupled to small data bubbles in another, such that both layers have the same run-out threshold.

A particularly important result is the discovery that stripes can be placed in tension when their ends are pinned and when the stripes are biased above the run-out threshold. The stripes can then be propagated by propagating the stripe ends. The stripe curvature was calculated and the maximum track width was found to be more than a millimeter. The pinning force between magnetic features and stripe ends was also calculated, as was the propagating force on stripes due to various current accessed propagation structures.

The theoretical investigations indicate that a self-structured multilayer device with a carrier layer containing stripes or stripes and bubbles magnetostatically or exchange coupled to data bubbles in a second garnet layer are very attractive configurations.

4. Experimental Investigations

4.1 Objectives

Conventional bubble memories require the presence of at least one propagation feature for each bubble domain. As a result, the entire memory area is populated with propagation features, which have a strong influence on device yield. It is an object of the following experimental investigations to reduce the number of propagation features, and to ultimately remove all such features from the memory area. This will allow for higher bubble densities, and higher device yields due to the reduced number of propagation features. A multiplicity of bubbles must, therefore, be moved with each propagation feature, and the experimental investigations reported herein are directed toward this goal. The designs must be compatible with current access techniques, whose advantages over field access methods have been discussed in section 2.3.

4.2 Experimental Equipment and Methods

Equipment employed for the experimental observation of garnet materials and propagation circuits includes a Reichert microscope and a 200 watt mercury arc light source. The light beam is polarized and applied at normal incidence to the sample, where the Faraday and/or the Kerr effect provide for visual observation. A television camera and monitor are utilized for ease of observation. The microscope stage is fitted with several coils to generate magnetic fields; normal dc fields up to 120 Oe, in-plane dc and rotating fields up to 150 Oe, and normal rf fields up to 10 Oe. One Oersted equals $1000/4\pi$ ampere turns per meter. Pulse generators with one amp output and 10 nanosecond risetime are available for testing current accessed circuits. A video tape recorder and a microscope camera are used for visual records of circuit performance and garnet material behavior.

Processing steps in the preparation of experimental circuits on garnet substrates include the thermal evaporation in vacuum of silicon monoxide as an insulating layer, aluminum-copper alloy or gold as a conducting layer, nickel-iron alloy as a magnetic feature layer, and sputtered silicon dioxide also as an insulating layer. Standard photoresist techniques are employed with chrome-on-glass artwork for circuit definition, and selective removal of material is accomplished with argon ion milling. Garnet dicing, mounting, and wire bonding follow standard integrated circuit procedures.

4.3 Experimental Circuits

4.3.1 Early Current Accessed Circuits

The first current access circuit to be evaluated for propagation of stripe domains is shown in figure 4.1. This is a scanning electron micrograph of a serpentine pattern of the type successful in propagating bubbles. Because this has the appearance of a square wave on an oscilloscope, this serpentine structure is also called a square wave conductor. The permalloy bars are located to move the stripes off the regions where the field gradient is insufficient to cause domain motion, and also to determine which direction the stripes are to be propagated. The experiments indicated that a more complete circuit is required to propagate stripes, a circuit that includes a stripe generator, annihilator, a barrier to isolate the stripes from domains outside the propagation area, and possibly means to prevent the stripe domains from collapsing.

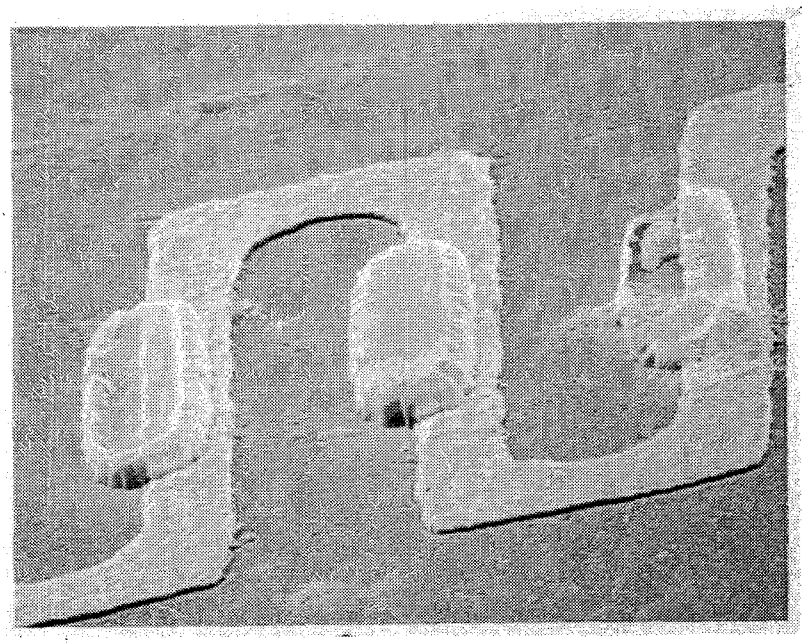

Figure 4.1 Scanning Electron Micrograph of a Serpentine Circuit with Permalloy Bars (x 3600, 65^{o}).

Stripes can be moved by long straight striplines parallel to the stripes. An array of such striplines can be used to propagate stripes, and such an array has been built and demonstrated. However, the first experiments were not conducted with such an array at all, but with a serpentine conductor. This conductor was rotated 90^{o} from the usual orientation so that it ran parallel to the stripes, and the distance a pulse of given emplitude moved a stripe was measured. In this experiment, a high bias stripe was initially set so that it was 12.5μm from the conductor on one side and 62.5μm from an adjacent stripe on the other side. A current pulse was applied to the line and the distance the stripe moved recorded. Another current pulse was applied, and so on, until no further change in position could be observed. After reinitialization, the process was repeated at a different current amplitude. Figure 4.2 is a graph of the maximum distance a stripe moves with multiple pulses as a function of pulse amplitude. Also on the graph are the number of one μsec pulses at each current value required to maximize the distance. As the stripes moves, it eventually encounters the repulsion of the flanking stripe and a competition results. In all cases it was observed that the moving stripe would cause the adjacent stripe to move in the same direction. This shows that pushing on one stripe in a lattice will push other stripes in the lattice.

A two layer conductor array was evaluated for stripe propagation. This is an array of long straight conductors in which the odd numbered conductors are pulsed first, then the even numbered conductors are pulsed, the odd numbered conductor again, and so on. The connections are made externally on this circuit, thus it can be used to study both two phase and three phase propagation.

The circuit was tested with biased stripes. It was found that the stripes could be propagated reliably and repeatedly both forwards and backwards with pulse currents of only 10 mA.

4.3.2 Offset Serpentine Array

A two phase single layer structure involving just a single evaporation is shown in figure 4.3. At one end of the structure is a set of conductors used for generating stripes and for pushing the stripes into the propagation region. Once in the region, the generated stripe is propagated by the offset serpentine structures, pulling on the ends of the stripe. There are four serpentine structures on each side, two of one phase and two oriented one quarter wavelength from that phase. The sets are pulsed alternately. Conductor numbers 1, 3, 5, and 7 are

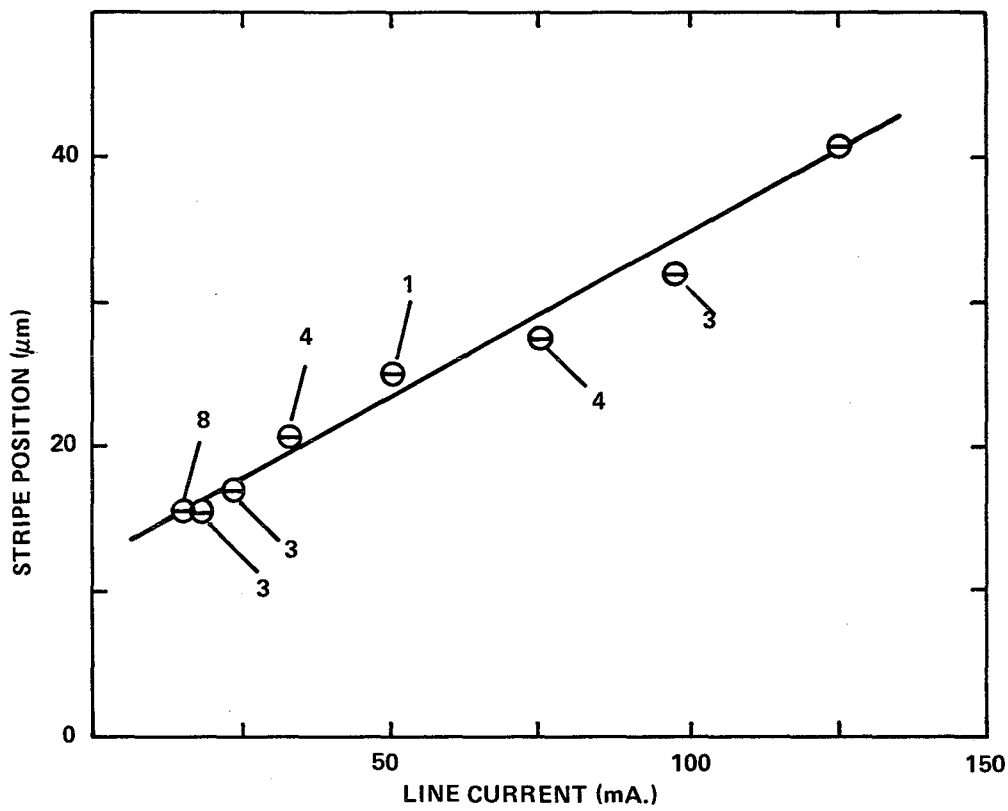

Figure 4.2 Stripe Domain Position Change due to a Conductor Field and an Adjacent Stripe; H = 50 Oe, and $4\pi M$ = 144 Oe.

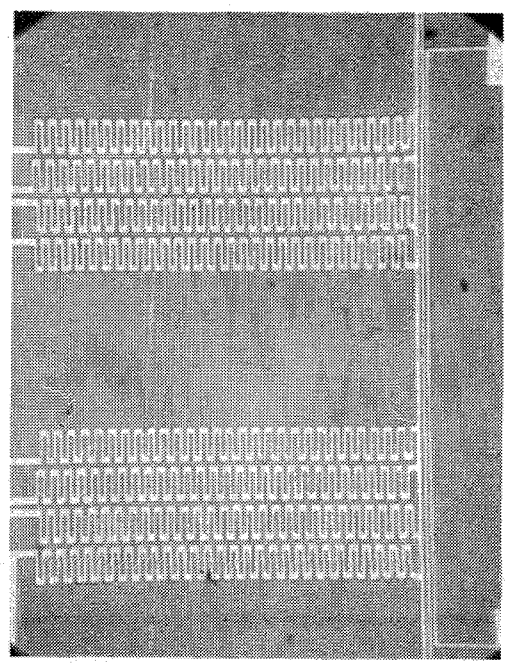

Figure 4.3 Micrograph of a Two Phase Single Layer Conductor Array Involving a Single Vacuum Deposition.

pulsed first; the polarity of the pulses on conductors 3 and 7 is opposite to the polarity of the pulses on conductors 1 and 5, because conductors 3 and 7 have been inverted to avoid current build-up on the bus line at the end. Next, the even numbered conductors are pulsed, and so on. Each pulse should move the stripe one quarter wavelength. To eliminate bowing of the wall, an rf tickle field is superposed on the external normal bias field.

This circuit was fabricated and exercised. The stripe generator at one end generated stripes, and the straight conductors expelled the stripes into the propagation region. The offset serpentine structure on the sides propagated those stripes even though an rf tickle field was not used. The circuit, however, had one important component missing, which created an unanticipated problem. A means for pinning the ends of the stripes was not included, and as the stripes were pushed into a neighborhood containing other domains, the stripes became shorter, contracting into dumbbells and bubbles. This circuit needs permalloy strips along the sides of the circuit to couple to the ends of the stripes and prevent them from contracting in length. A current conductor along the sides is an alternate method of accomplishing the same goal. A prime economical and practical advantage of this circuit is that only one conductor layer is required.

Figure 4.4 shows the test circuit with permalloy strips for the single level two phase serpentine stripe propagator. A single stripe is visible in figure 4.4. The stripe is pushed forward, or backward, one step at a time from alternate serpentine conductors. The ends of the stripe are pinned by permalloy strips at the side. The circuit must be operated at a normal bias field that is greater than the run-out threshold, which is necessary in order that the stripe be under tension and be relatively straight. The higher the bias field, the higher the tension, and the straighter the stripe.

The permalloy strips did an effective job of stripe pinning. The bias field could be raised not only above the run-out threshold, but approximately 10% above the bubble collapse threshold as well, without collapsing the stripe. The margin can be expected to increase as the number of stripes under the permalloy is increased to normal operating levels, and with further improvements in pinning bar design.

Stripe domains are easily and effectively nucleated by a set of three conductors shown at the bottom of figure 4.4. A single 50 nsec 900 mA pulse applied to the bottom conductor nucleates a complete stripe pinned at the permalloy bars, over the normal

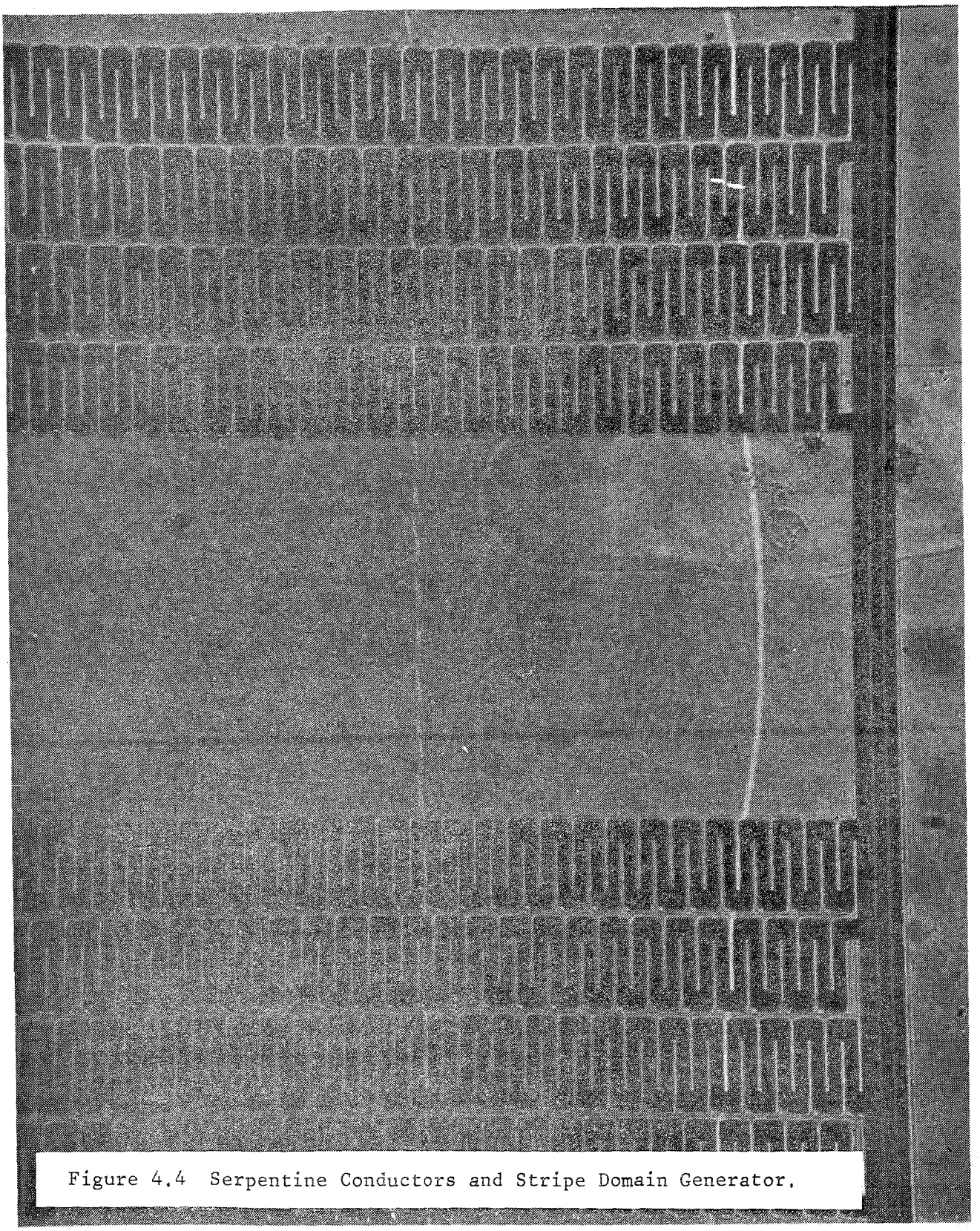

Figure 4.4 Serpentine Conductors and Stripe Domain Generator.

bias field range of 56-66 Oe. This can also be done with two complimentary pulses of lower amplitude on the two bottom conductors. Subsequent pulses on the upper two conductors translate stripes into the propagate test area.

Once into the propagate test area, the stripe is moved piecewise by the serpentine conductors. A current threshold of 5 to 10 mA is required in a serpentine circuit to reliably move a short segment of the stripe to a new equilibrium position. The amount of current required depends on the excess normal bias field above the run-out threshold. This is shown in the curve of figure 4.5. The reason for this behavior is that the higher the bias, the higher the tension in the stripe, and the greater the tendency for the adjacent segments to pull back the moved segment from the new position.

Figure 4.6 presents a four step sequence detailing the movement of a stripe end translating one half cycle under the left hand set of conductors. From the starting position shown in figure 4.6a, the required pulse sequence is $4^{+}\ 2^{-}\ 3^{+}\ 1^{-}$, which is shown in figure 4.6b through e, respectively. The second half cycle would follow with $4^{-}\ 2^{+}\ 3^{-}\ 1^{+}$. Under normal operating conditions, conductors 4 and 2, as well as 3 and 1, are operated alternately in pairs, reducing the eight steps per cycle down to four. In addition, conductors 1 and 2 should be phase shifted one half cycle, allowing the pairs 4-2 and 3-1 to be activated with the same polarity pulses. A single pulse would therefore be sufficient to activate four of the conductors at the same time with a total of four pulses required to move the entire stripe one complete cycle.

The purpose of this study was to test a combination system which (1) generates stripes, (2) continuously pins the stripes on separate permalloy pinning strips over a range of bias fields, and (3) propagates the stripes along in a spatially separated stepwise fashion. The goal was to learn enough about such combinations to improve, redesign, and utilize them for future devices. A number of observations were noted:

(1) The generator conductor is also the current return path for the serpentine conductors. This is undesirable, because when the stripe is near the generator, current in one of the serpentine conductors returns through a segment of the generator and causes a corresponding segment of the stripe to move the wrong way.

(2) The magnetostriction of the garnet, coupled with the strain of the conductors on the garnet, sometimes causes the stripes to favor locating along the serpentine conductors even when the current is off.

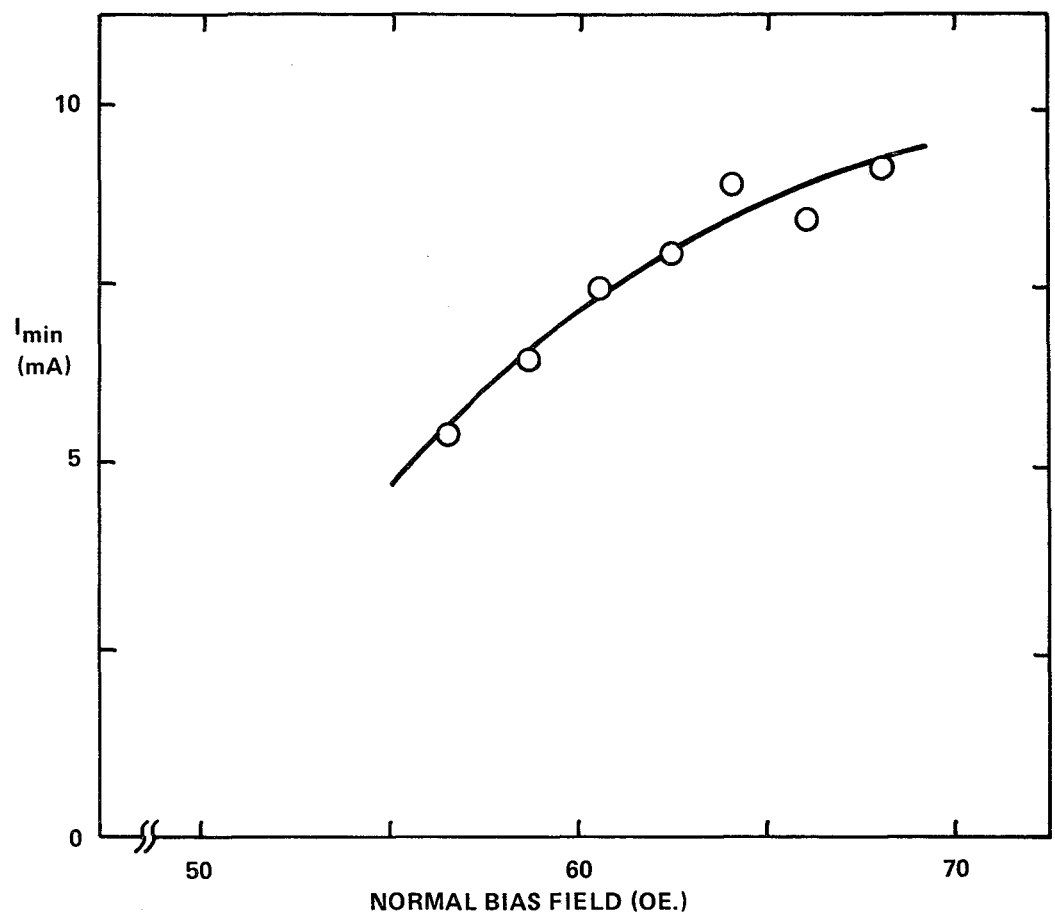

Figure 4.5 Minimum Drive Current Required to Move a Stripe Segment vs. the Normal Bias Field.

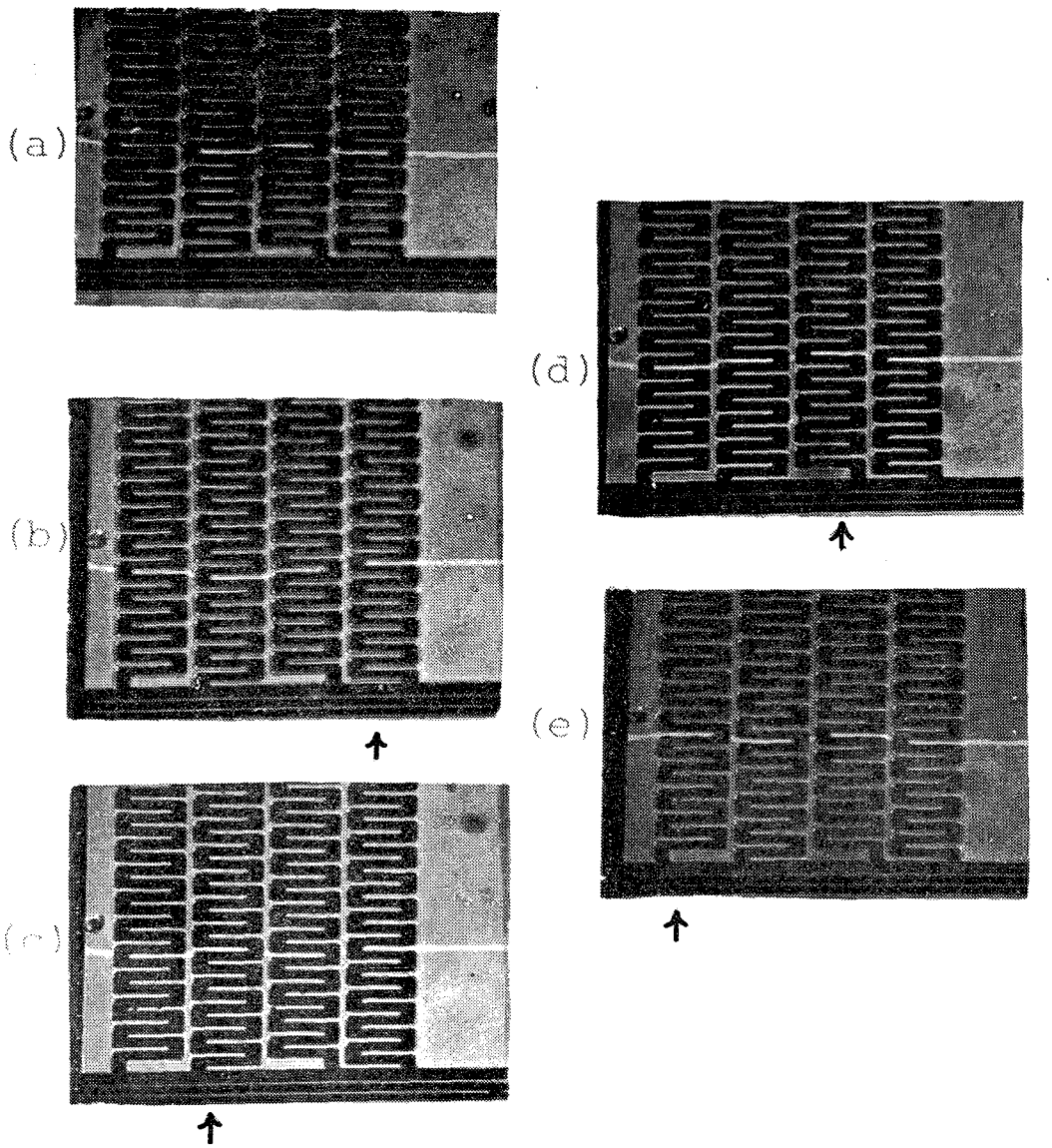

Figure 4.6 Piecewise Translation of a Stripe Domain End for One-Half Cycle.

(3) The equilibrium positions on the two serpentine circuits are so close together that the stripe domain can rest at those positions on both circuits at once without much bending. Unless a very high bias field and tickle field are used, the stripe is not stiff enough to be eased off the equilibrium position of the non-accessed circuit. When that circuit is accessed, the stripe may move the wrong way.

(4) The pinning bars are too wide, generating a situation where a complex stripe structure can exist under them. This sometimes causes the stripe ends to move when the normal bias field is increased, and is partially caused by the bias field not perfectly aligned normal to the film.

4.3.3 Magnetically Assisted Serpentine Circuits

Researchers at the Philips Research Laboratories have published a series of articles [8,9,10] describing their investigations of bubble circuits having both field accessed and current accessed features. Of particular interest to this program are the magnetically assisted, current accessed bubble propagation and stretcher designs. These circuits have NiFe features that, in general, are located over a conductive stripline, as displayed in figure 4.7. Bipolar current pulses and an in-plane magnetic field are required for successful propagation of bubbles.

The series of drawings in figure 4.8 depict the motion of a bubble through the circuit of figure 4.7a with the application of bipolar current pulses in the presence of an in-plane magnetic field. With the in-plane field directed to the left, the bubble motion is to the right, as shown.

The Philips circuits displayed in figure 4.7 have been modified in design configuration for the purpose of propagating stripe domains. Figure 4.9 shows one design, where stripe propagation is accomplished by translating each end of the domain. Bipolar current pulses are required in each serpentine leg of the circuit, in addition to an in-plane magnetic field. Motion of the ends of the stripe domain is similar to that of a bubble domain depicted in figure 4.8. The long conductors at the top of the circuit are employed to generate stripe domains.

A second circuit design is presented in figure 4.10, where each magnetic bar of figure 4.9 has been replaced by a magnetic chevron. Although the period to gap ratio for the chevrons may not be optimized for field accessed propagation, the concept tendered

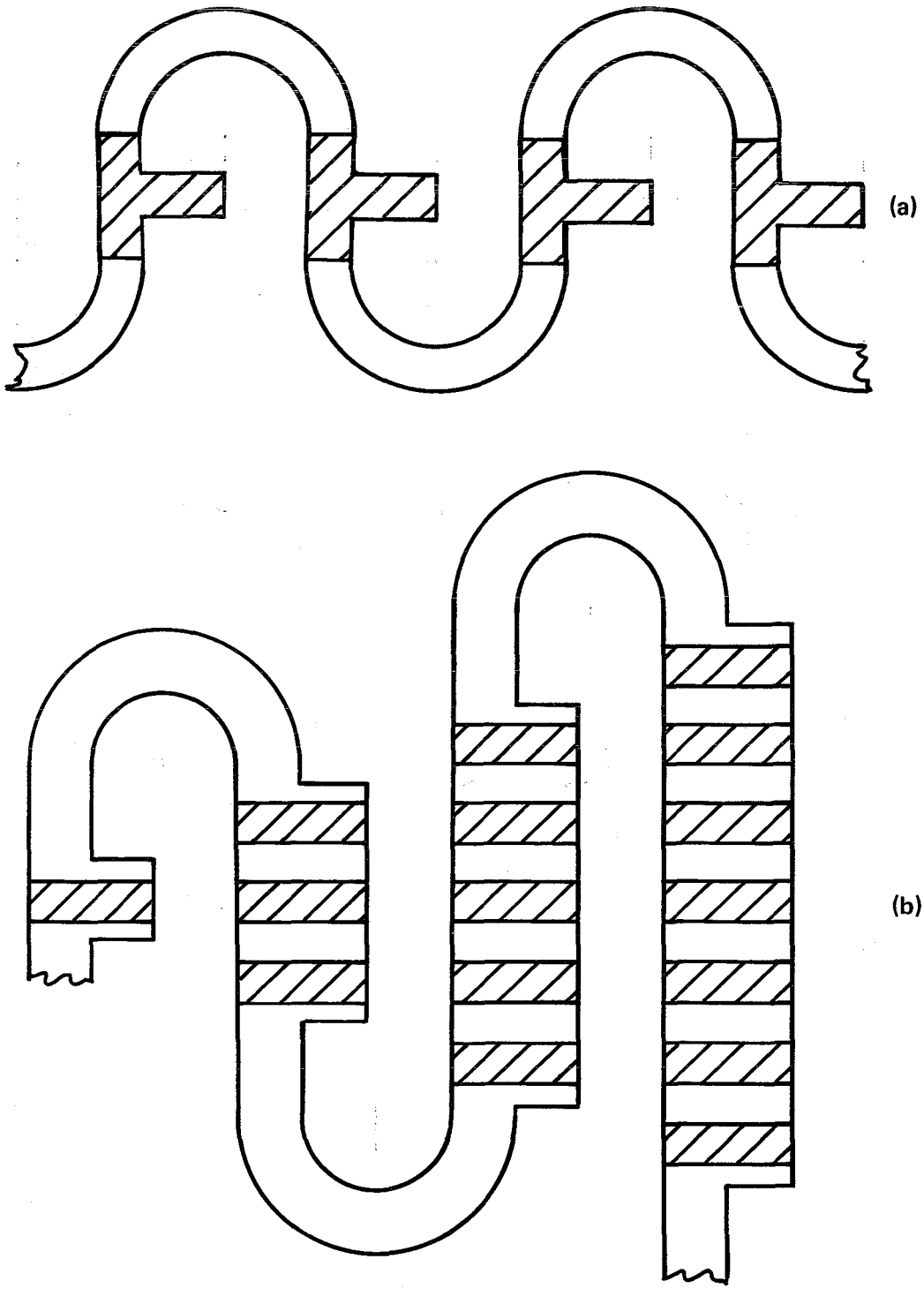

Figure 4.7 Magnetically Assisted Bubble Propagator (a) and Expander (b).

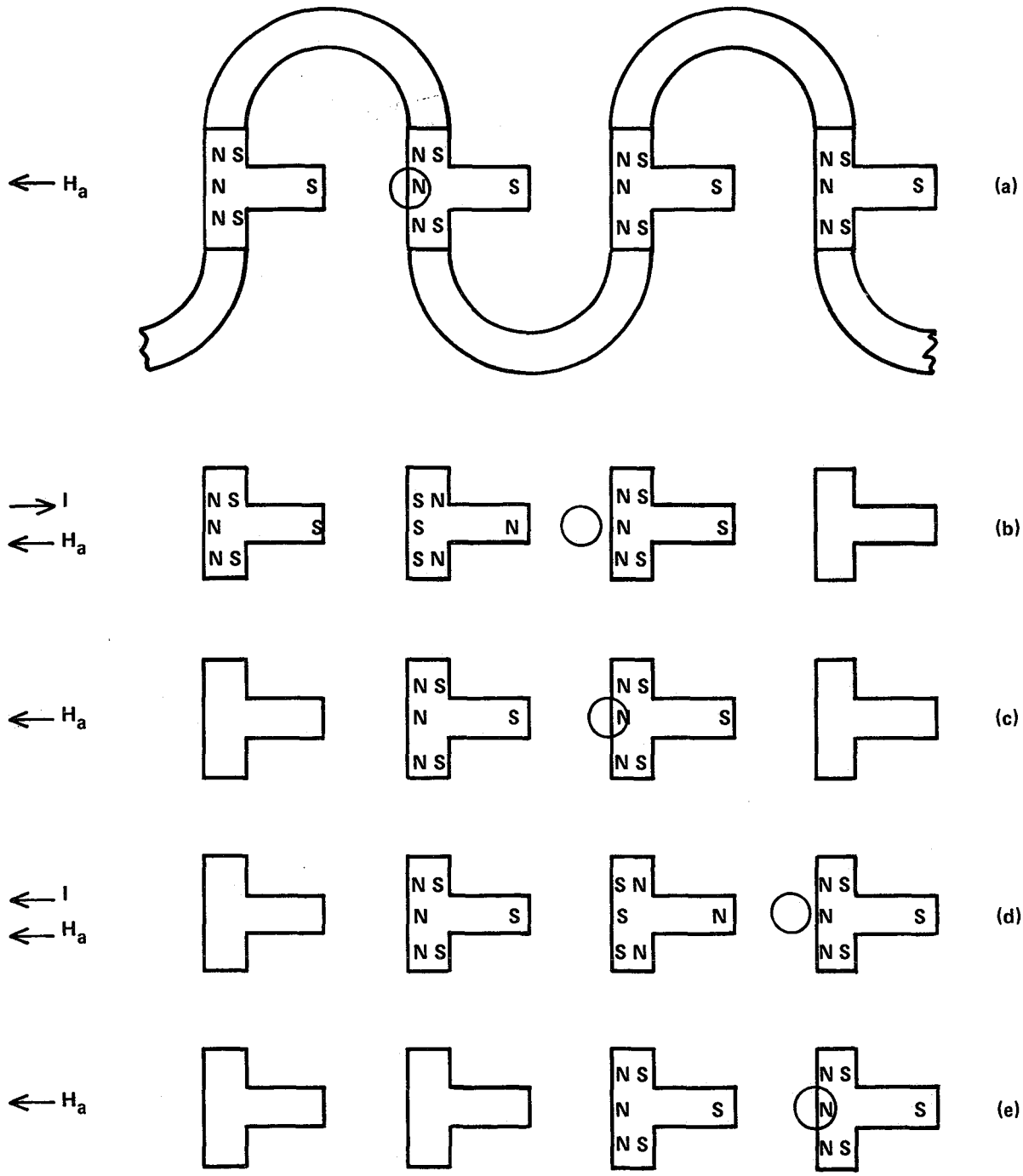

Figure 4.8 Propagation of a Bubble Domain with Applied Current I and Applied In-Plane Field H_a.

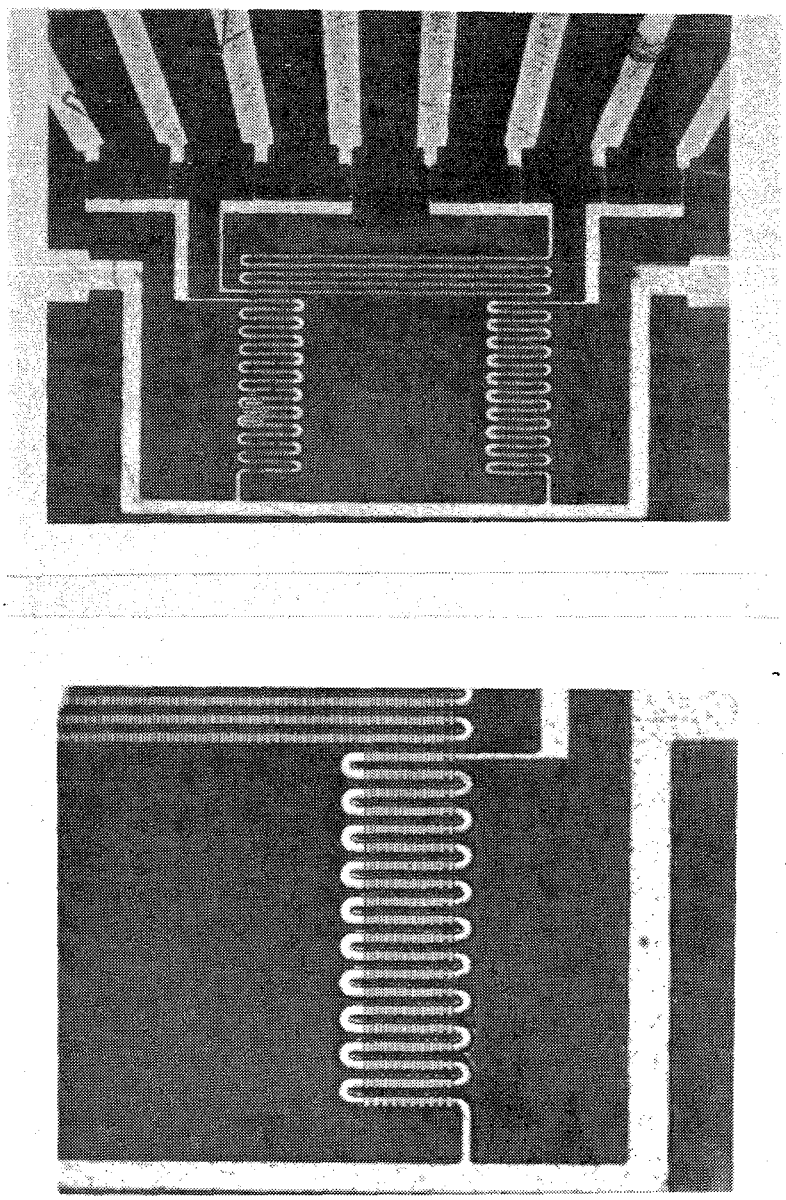

Figure 4.9 Stripe Domain Propagation Circuit with Magnetic Rectangles.

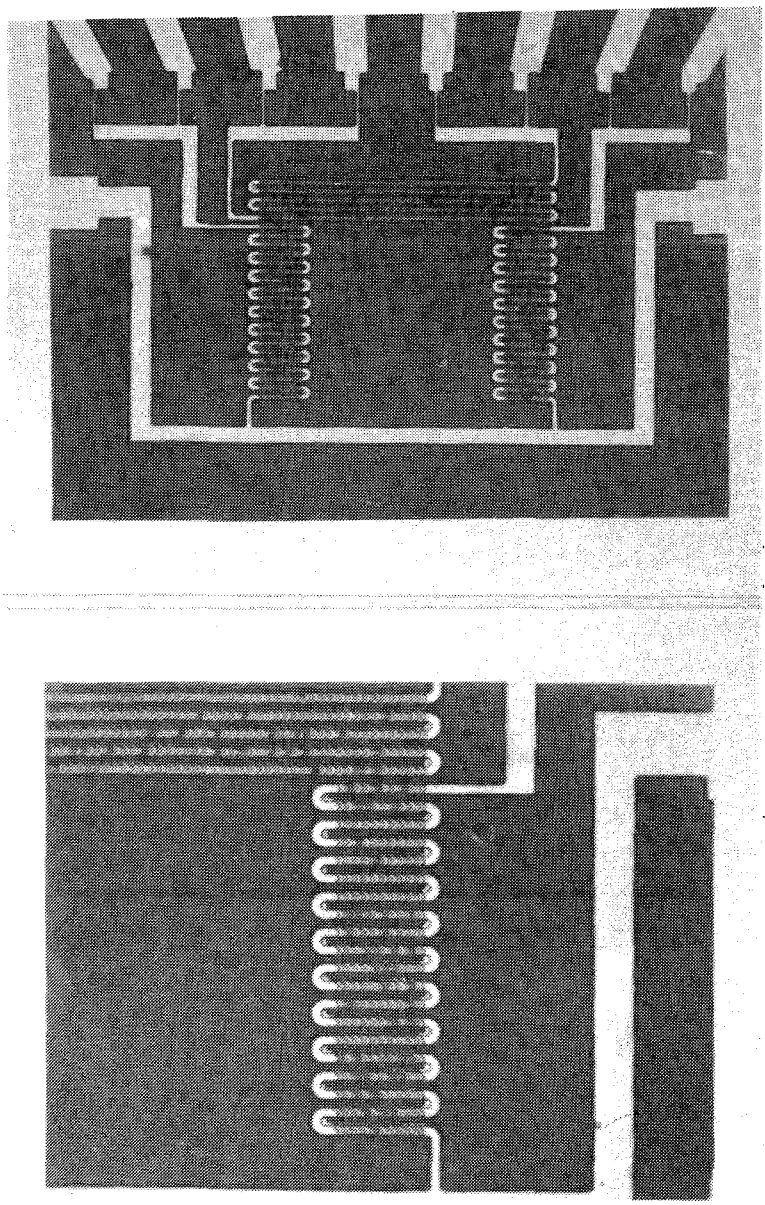

Figure 4.10 Stripe Domain Propagation Circuit with Magnetic Chevrons.

is a circuit that may operate with either field accessed or current accessed techniques. Propagation of stripe domains through the use of chevrons and rotating fields have been demonstrated in the past. With current accessed conductors, these chevrons should propagate bubbles or stripe ends in the same manner as the bar circuit of figure 4.9.

One of the advantages in designing this type of circuit is to extend the time available for testing purposes. It is almost inevitable that the current accessed circuit will become an open circuit, either due to operator error or test equipment malfunction. This design will hopefully extend the useful test time, if the circuit becomes open, by employing field accessed techniques.

Testing the circuit with NiFe chevrons demonstrated that propagation of stripe domains can be accomplished with both field access and current access techniques. With a rotating field peak value of 60 Oe, and a normal bias field of 50 Oe, stripe domains were propagated along the chevron rows. The stripes showed considerable bowing at their center. Measuring the normal field value to collapse a free stripe, and also a NiFe pinned stripe, indicated that the magnetostatic coupling between the chevrons and the stripes was approximately 9 Oe. This coupling is relatively small, and explains the stripe curvature. If the chevrons were located between the conductor and the garnet, the coupling would be considerably greater. Reversing the direction of the in-plane field, approximately 15 Oe, caused the propagation direction to reverse.

Propagation of the ends of stripe domains was observed while employing current accessed techniques. With an in-plane field of approximately 15 Oe, a normal bias field of 52 Oe, and bipolar current pulses of $\pm$ 20 mA and 1/3 μsec duration, stripe propagation under and near the conductors was observed. Due to the weak NiFe to stripe coupling, propagation of the entire stripe domain was not accomplished. Generation and propagation of stripes in the long generator section of the circuit was successful. Under all circumstances of current access, there was no propagation when the in-plane field was removed.

4.3.4 Segmented Chevron Circuit

A third permalloy assisted current access circuit has been designed which does not employ serpentine conductors, and incorporates a new concept of segmented chevrons. Figure 4.11 displays this circuit, showing the segmented chevrons located above the conductors, and also showing three long rows of normal chevrons. The principal advantage of this design over the previous two is that the conductor is wide and straight and does not have to meander back and forth, and thus has much lower resistance, and

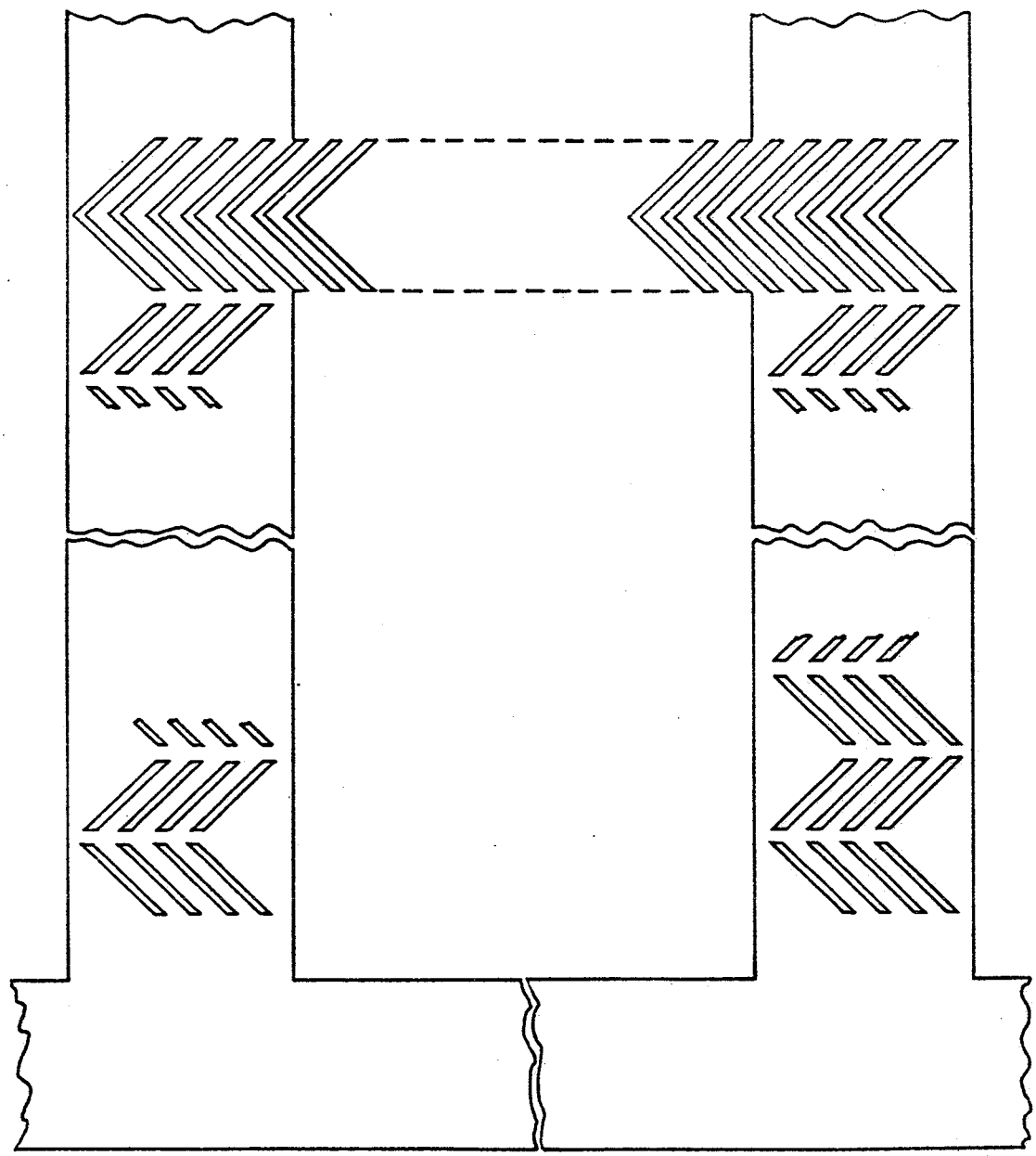

Figure 4.11 Segmented Chevron Circuit.

is easier to fabricate. This design also requires the presence of an in-plane field perpendicular to the stripe domains, in addition to bipolar current pulses. Figure 4.12 depicts the motion of a bubble along the segmented chevrons of figure 4.11 under magnetic field cycling.

Magnetization in one of the segmented chevron bars, parallel to the long edge, is shown in figure 4.13 as a function of the field from the strip line H_I, for an applied in-plane field H_a of 25 Oe. The chevrons shown in figure 4.11 have an interior angle of 90^o between neighbors, which corresponds to the 45^o curve of figure 4.16. This curve shows that a conductor generated field of 25 Oe will either saturate or demagnetize chevron A along its long dimension, depending on the polarity of the current pulse in the stripline. A bipolar current pulse which produces a field near $\pm$ 75 Oe will be a good compromise for proper operation of both chevrons. For a line width of 28 microns, this corresponds to a current of $\pm$ 335 mA; or $\pm$ 190 mA for a 16 micron wide line.

The segmented chevron circuit can be operated either with current access or with field access. When the circuit is operated with field access, the external in-plane field does not rotate 360^o around and around as is the case for normal chevrons, but rather rotates back and forth, through a total sweep of 180^o. When operated in a current access mode, an alternating current in the conductor supplies an alternating in-plane field which, when combined with an external dc field, causes domains to be propagated in a direction opposite to the dc field. The direction of motion can be reversed by reversing the direction of the dc field. How the propagation works is illustrated in figure 4.12.

The advantages of the segmented chevrons for propagating domains are:

1. The conductor is straight and broad and can thus have low resistance. The conductor does not meander like the serpentine conductors required for the other permalloy aided circuits described in the previous section.

2. The conductor runs perpendicular to the stripes, so the field from the conductor exerts no force that would tend to move the stripe. The conductor can be placed above the permalloy or below the permalloy, in contrast to the other permalloy aided circuits described in the previous section. Those circuits require the conductor to be between the garnet and permalloy, seriously degrading the coupling between the permalloy and stripe.

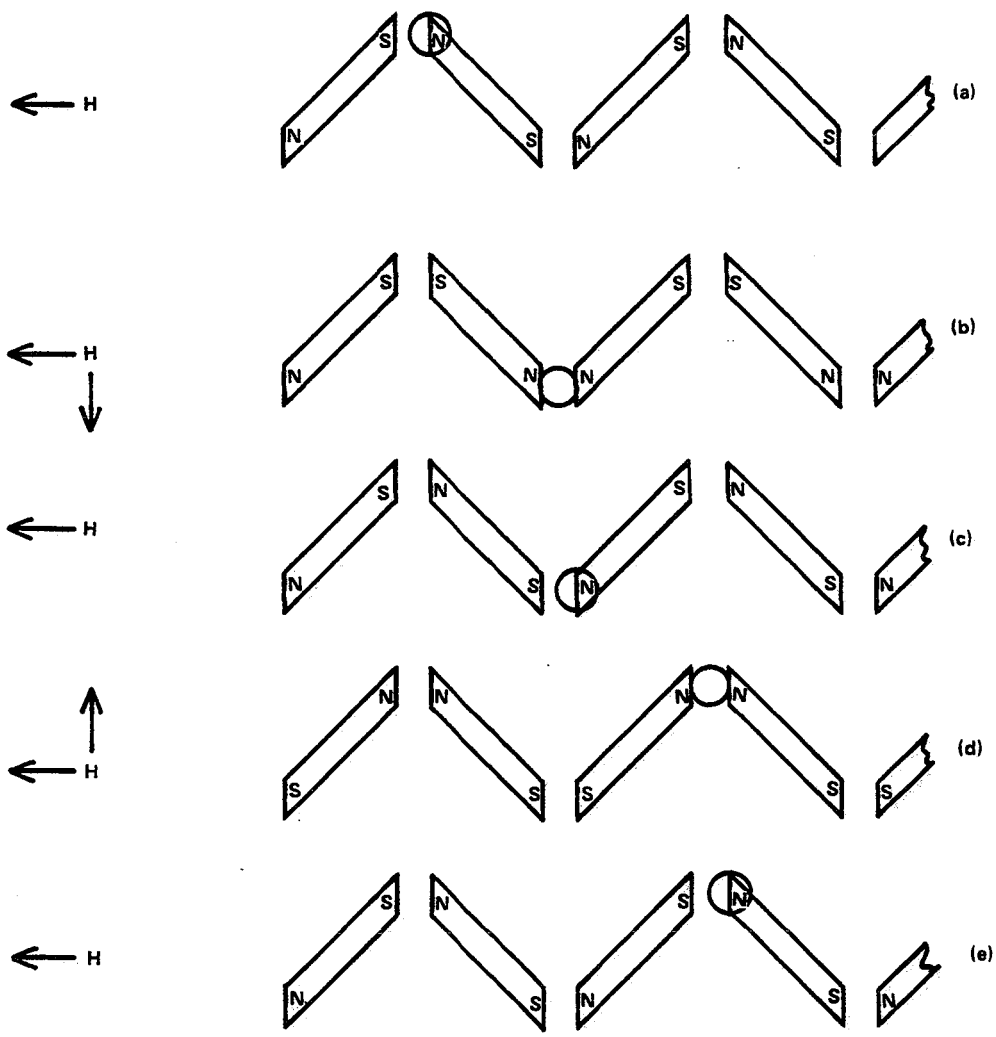

Figure 4.12 Bubble Propagation Through a Segmented Chevron Circuit, with Magnetic Fields from Conductor Current and External Application.

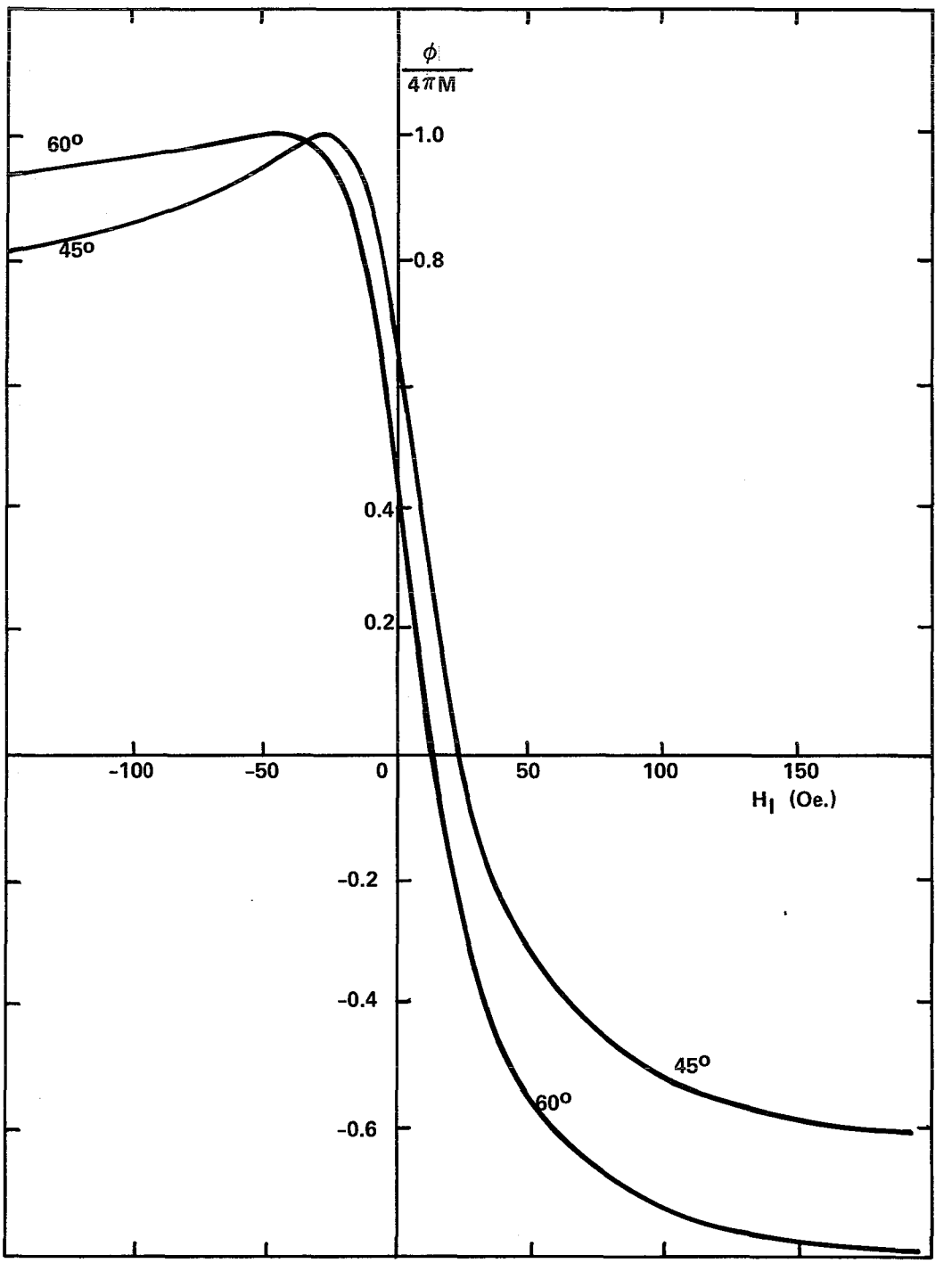

Figure 4.13 Magnetization Strength in a Chevron vs. the Magnetic Field from a Stripline Conductor, with Ha = 25 Oe.

3. Because the permalloy can be next to the garnet, the segmented chevron can be self-pinning, i.e., the chevrons can pin the ends of the stripes and prevent the stripes from contracting to bubbles even when the bias field is larger than the run-out threshold.

4. The segmented chevron can be used either in a field accessed mode or in a current accessed mode. This can be quite useful in experimentally analyzing the performance of an experimental device.

5. The dc in-plane field can be quite small, and is reversed only when the direction of propagation is to be reversed. Thus, the dc field does not impact the power or the speed of the device.

The disadvantages of this design are related to stripe cutting. There is a normal component of field from the conductor that is a maximum at the edge of the conductor. If this field is too large it can cut the stripe. The narrower the conductor and the farther away from the garnet, the smaller this effect. Propagation of stripes with this experimental device was possible without cutting the stripes.

Figure 4.11 displays the circuit that was tested. Segmented chevrons are used as propagating elements; full chevrons are used as stripe generators. The permalloy was placed on top of the conductor instead of between the stripline and the garnet, and resulted in weak coupling between the stripes and chevrons. The circuit was unfortunately fabricated on a garnet that has a long defect that runs diagonally across the circuit, which prevented full operation of the circuit.

The zero in-plane field coupling between stripes and segmented chevrons can be measured by measuring the difference in run-out threshold for stripes under the permalloy and stripes not under the permalloy. This was found to be only about 4 Oe for both normal chevrons and segmented chevrons. Operating bias is 65 Oe. This weak coupling is due to the large separation between the garnet and permalloy. Had the circuit been made with the permalloy next to the garnet, the coupling would have been much larger.

Propagation was tested in the leg of the circuit not blocked by the defect. Propagation was achieved both in the field access mode and the current access mode. A schmoo plot was made of the region of propagation: a plot of the locus of the combination of in-plane bias field and stripline current amplitude that propagates stripes, which is shown in figure 4.14. Propagation is

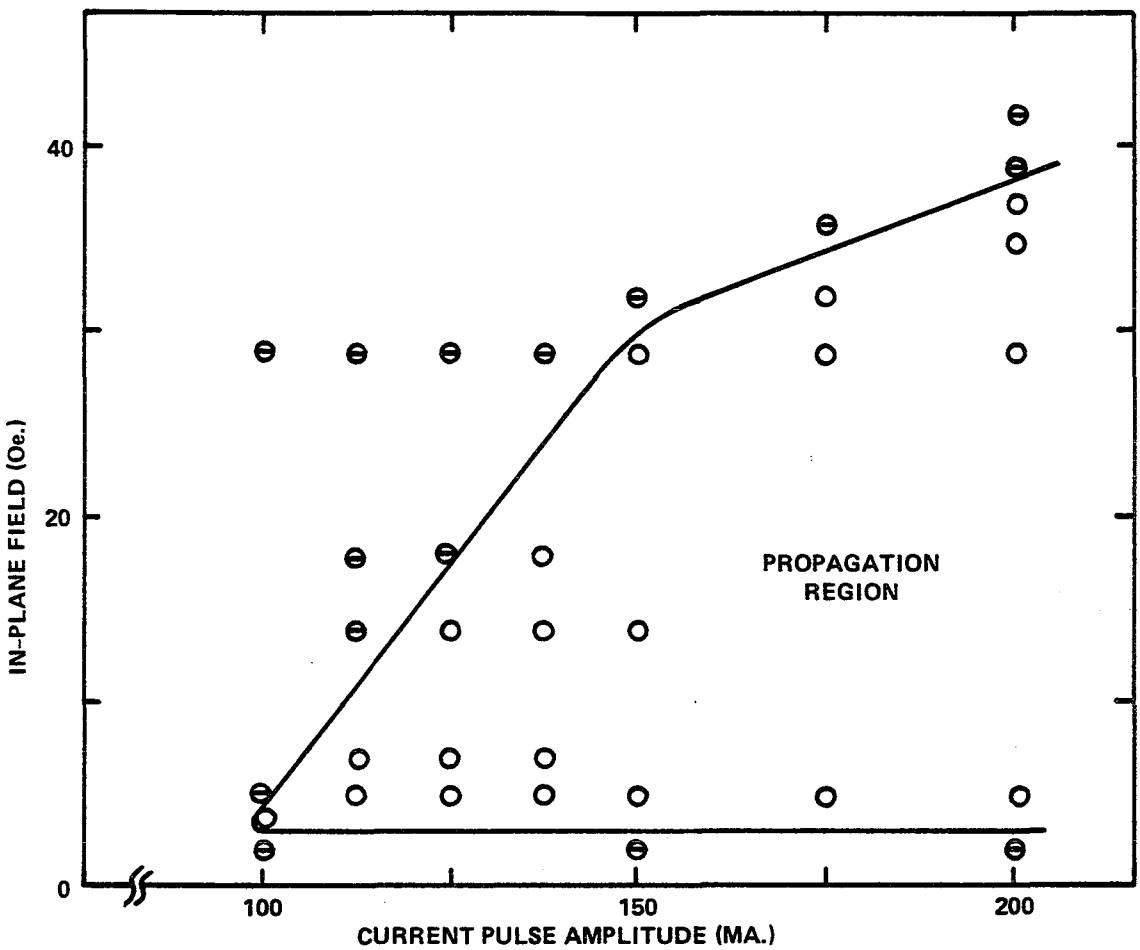

Figure 4.14 Propagation Region for the Segmented Chevron Circuit. Normal Bias Field = 42 Oe.

achieved with an in-plane field as low as 3 Oe and a current pulse amplitude as low as 100 mA in each conductor. When the in-plane field is increased, the required pulse current amplitude, in general, is also increased. Propagation failed with current pulses shorter than one microsecond. This corresponds to a domain velocity of 8m/sec, which is close to the limiting speed of domains in the garnet material.

The segmented chevron stripe propagator is extremely promising. It is the most attractive of the permalloy assisted current accessed propagators. It is self-pinning, fast, can be fabricated with the permalloy next to the substrate, has low registration specifications, requires low power, and can be operated as either a field accessed or current accessed device.

4.3.5 Apertured Current Sheet Experiments

Late in this contract, experiments were performed with apertured current sheets. The motivation was to use these sheets as an I/O track to insert and/or remove a row of bubbles from the side of an array. Current sheets appeared attractive for this application for two reasons: They require no permalloy and the minimum required feature size is two times larger, for a given bubble spacing, than either serpentine circuits or segmented chevrons. The lack of permalloy is important because during the stripe propagation phase, stripes and bubbles must be propagated past this I/O track unimpeded. A permalloy feature can trap a bubble or a stripe.

The experiment was successful; bubbles were propagated around loops defined by the apertures in the current sheets. Parts of the loop propagated bubbles parallel to the current flow, and other parts of the loop propagated bubbles perpendicular to the current flow. We were surprised and gratified to find that the latter also propagated stripe ends.

Current sheet propagators incorporate two layers of conductor sheets with apertures, and current accessed domain propagation is achieved without magnetic features. Figure 4.15 illustrates this concept, where the dotted apertures are in the conductor next to the garnet. Application of currents I_1, I_2, I_3, I_4, I_1 --- will propagate the bubble domain parallel to the current direction, as shown. A reversal in the order of applied currents will cause the bubble domain to propagate in the opposite direction.

Figure 4.16 compares the minimum feature size for one layer of current sheet propagators with other propagation schemes. The bubble spacing is the same for all. The feature size for non permalloy assisted serpentine must be twice as small. If permalloy bars are added to the serpentine circuit as shown, the minimum feature size falls by another factor of two.

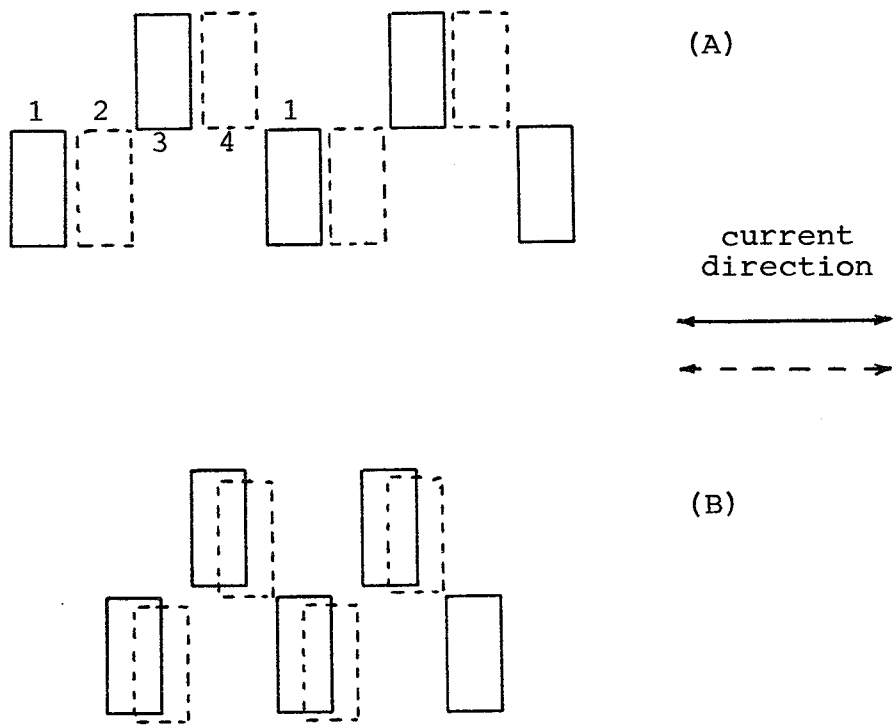

Figure 4.15 Data Track for Bubble Propagation Parallel to the Current Direction.

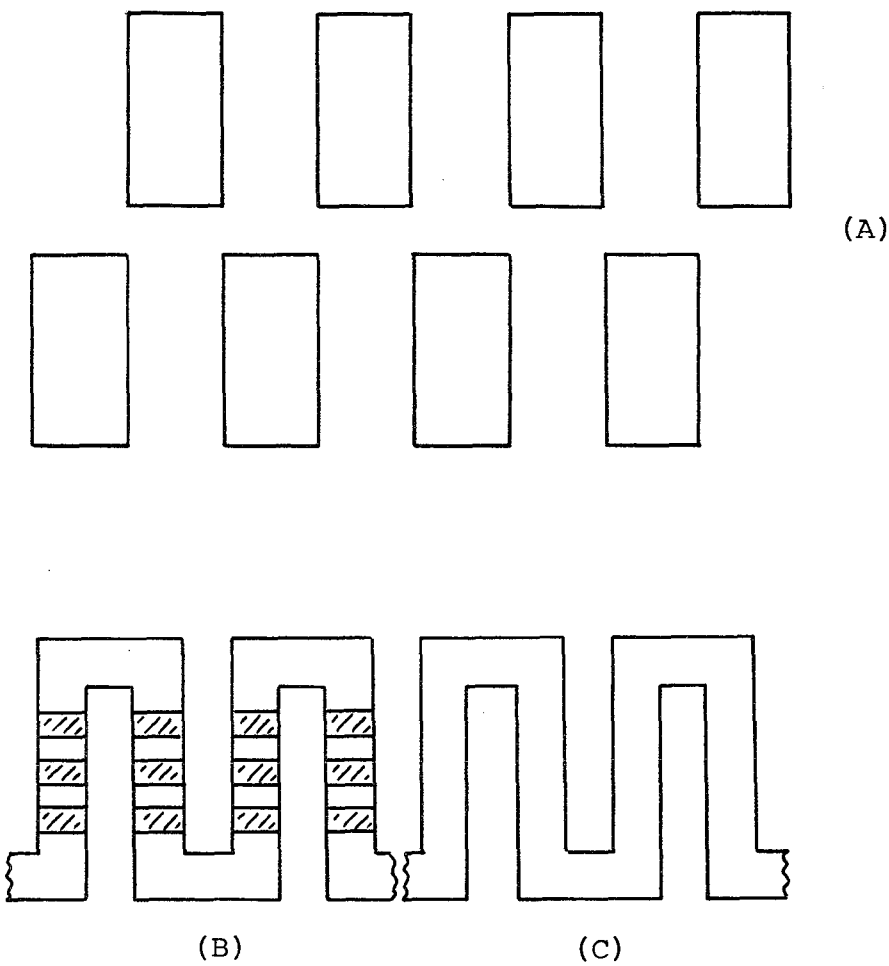

Figure 4.16 Comparison of Feature Size for One Layer of Current Sheet Propagator (A), NiFe Assisted Serpentine (B), and One Layer of Two Layer Serpentine (C).

The experiments demonstrated that stripe ends can be propagated with current sheets with current perpendicular to the propagation direction. Figure 4.17a illustrates a method that translates only the ends of a long stripe domain. An advantage of the current sheet propagation is that additional propagation features can be distributed along the stripe with no penalty, as illustrated in Figure 4.17b. This design possesses the advantage of redundancy. If a propagation feature is defective, neighboring features will propagate the stripe past the defective feature. With added propagation features, the problem of stripe bowing due to end translation will be reduced, which also reduces the requirement for garnets with very low coercivity. Later and improved designs are illustrated in Section 7.

4.3.6 Stripe Domain Curvature

As an empirical verification of the theoretical calculations presented in section 3.4.6, two experiments have been performed. Both experiments involved the generation and propagation of isolated stripes in chevron devices similar to that shown in figure 3.19. Stripe domains were propagated back and forth along the track of the chevron device by reversing the direction of rotation of the drive field, being careful to preserve the phase sense at all time. At the end of each field application the amount of distortion, shown as z in figure 3.19 was measured. Two situations were considered. In the first, the stripe curvature was measured as a function of the rf tickle field, H_{rf}, while the bias and drive field amplitudes H and H_r remained constant. In the second, the bias field amplitude was varied while H_{rf} and H_r remained constant. Using equation 3.46, this data allowed for the calculation of the effective coercivity H_c.

Both experiments were performed on a three sided 12.7μm period chevron device fabricated on a YLaTmGaFeO garnet. The relevant garnet properties are: h = 6.21μm, $4\pi M$ = 115 Oe, H_k = 1060 Oe, and ℓ = 0.752. The device employed was 185μm wide and about 1000μm long.

The results of the first experiment are shown in figure 4.18. Two calculations were performed. The coercivity H_c was first calculated using only the normal bias field H. In the second, the coercivity Hc* was found using the value $H + H_{rf}$ as the effective bias field seen by the garnet, where H_{rf} is the peak value of rf bias tickle field. As expected, the effective coercivities are a strong function of the rf tickle field, showing a tendency to level out as H_{rf} reaches higher values. The effect was manifested in the stripe as an increase in the radius of curvature with increasing H_{rf}, i.e., the stripe was straighter at higher rf amplitudes.

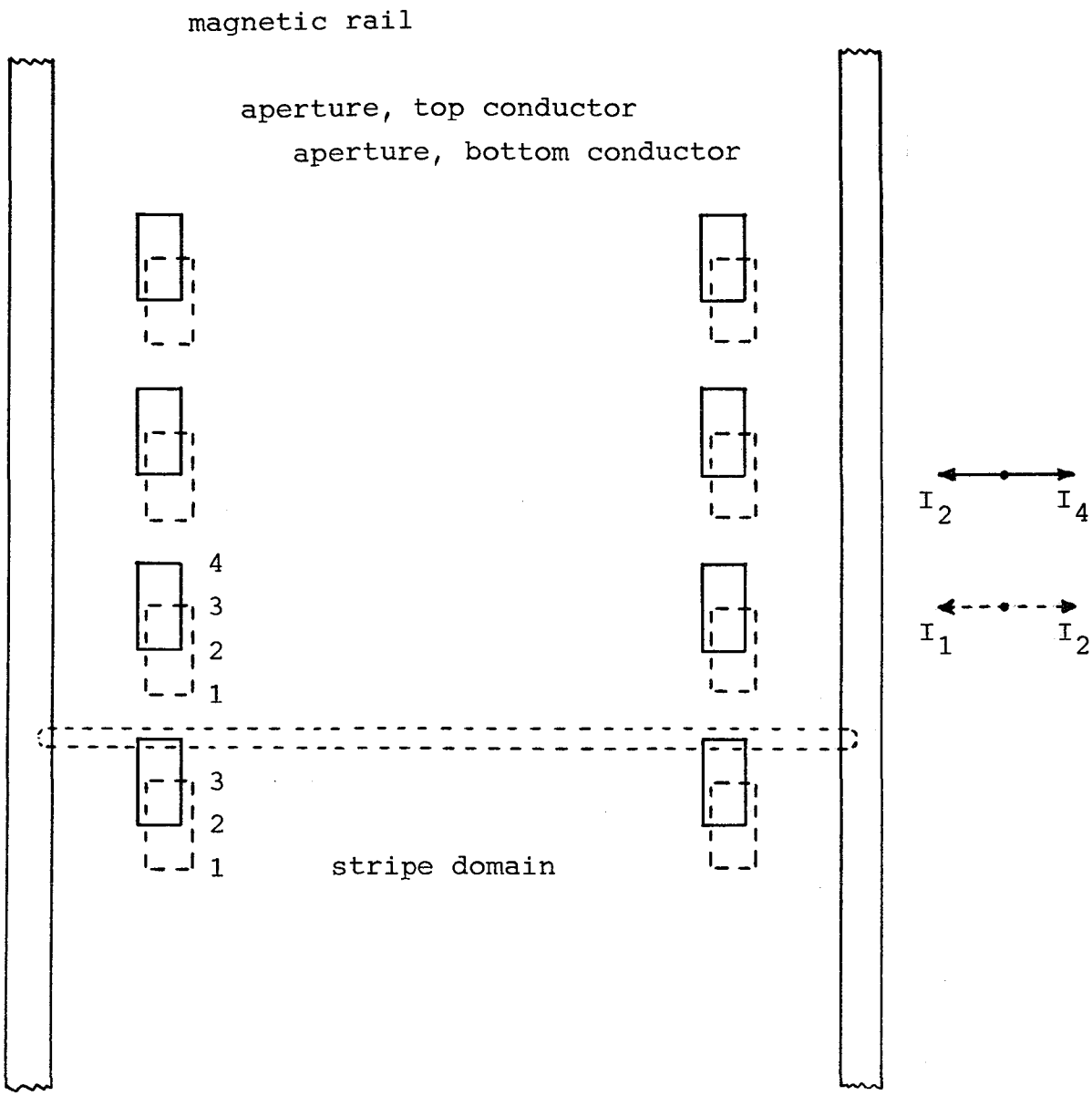

Figure 4.17a Stripe Domain Propagation with Dual Apertured Conductors.

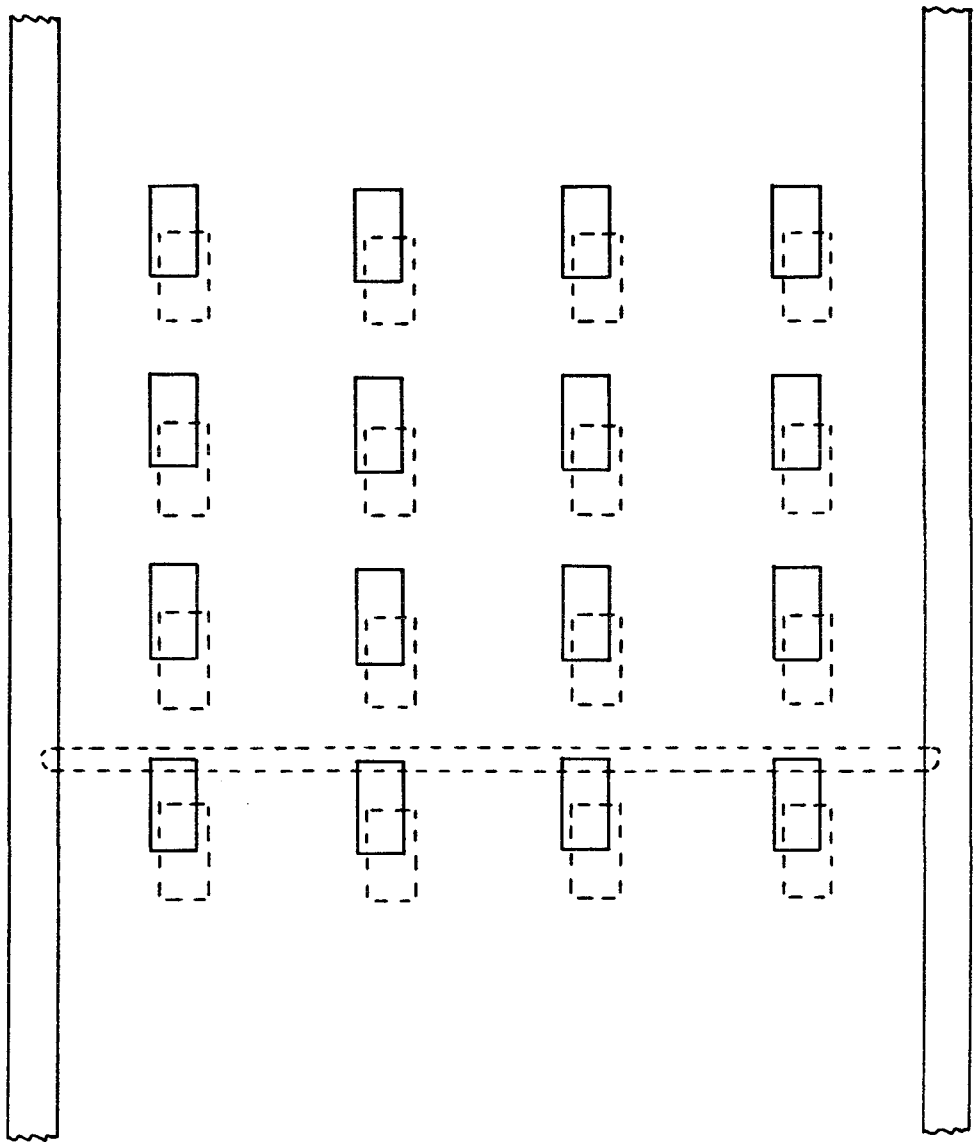

Figure 4.17b Stripe Domain Propagation Design with Additional Dual Conductor Apertures.

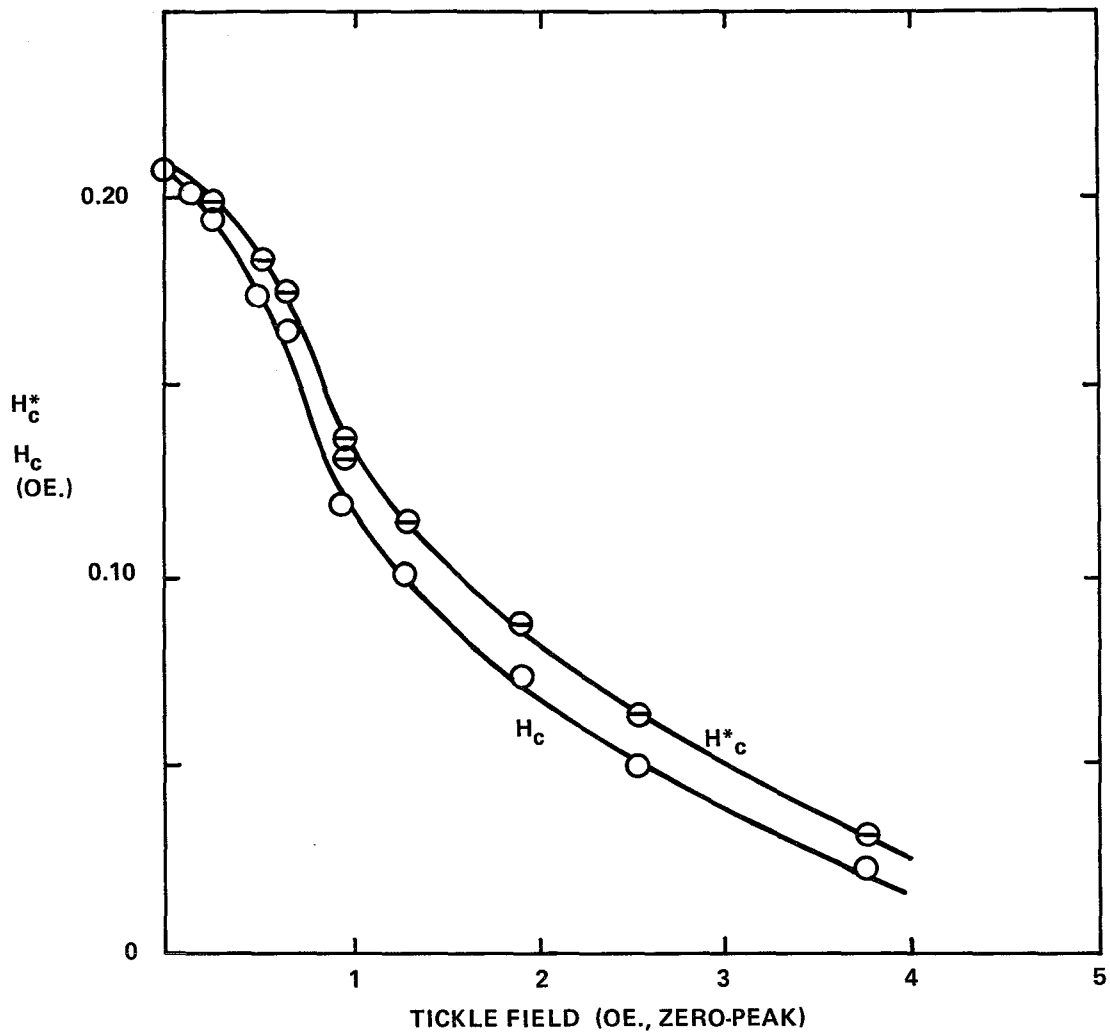

Figure 4.18 Garnet Coercivity vs. Tickle Field Amplitude.

In the second experiment the rf tickle field was held constant while the bias field was varied. The curvature was measured, and the coercivity was calculated from equation 3.46. As expected, the coercivity remained constant within experimental error. This lends confidence in the theory.

As a refinement to the theory, the data on curvature of the stripe was fitted to a catenary instead of an arc of a circle, but the difference was found to be negligible.

4.4 Magnetic Features and In-Plane Fields

During the initial testing of stripe propagation devices incorporating permalloy pinning bars, stripe ends were observed to creep along the permalloy bars as the bias field was increased. This phenomenon has been attributed to the domain pattern in the permalloy bars interacting with in-plane components of the bias field. As indicated schematically in figure 4.19, appropriate domains in the permalloy bars grow as the in-plane field component is increased, carrying the stripe ends along. In the extreme, this phenomenon can sweep the stripe domain completely off one end of the device. Although this phenomenon should not be a problem with a fully populated stripe array, it is a bothersome problem when testing devices populated with only a single stripe. To overcome this problem simply requires an alteration of the domain pattern in the permalloy bars. This can be easily accomplished by the use of a small in-plane field perpendicular to the NiFe pinning bars (i.e., parallel to the stripe) as illustrated in figure 4.20. Using 50μm wide bars and 5 to 11 Oe in-plane fields, it has been observed that pinned stripe domains are extremely stable as the bias field is varied through values from the run-out field H_{RO} up to 25% over the bubble collapse field, H_O. The magnitude of this in-plane field is limited only by the value at which the pole strength at the inside edge of the pinning bar becomes strong enough to slice the stripe domain. Typical values for this threshold are 15 to 17 Oe, allowing ample margins for thorough testing of present devices.

The use of the perpendicular in-plane field provides improved stripe end pinning while at the same time reducing device sensitivity to a parallel in-plane field. This perpendicular field can also be supplied by the use of permanent magnet materials in the bars, as well as by a slight canting of the device with respect to the normal bias field.

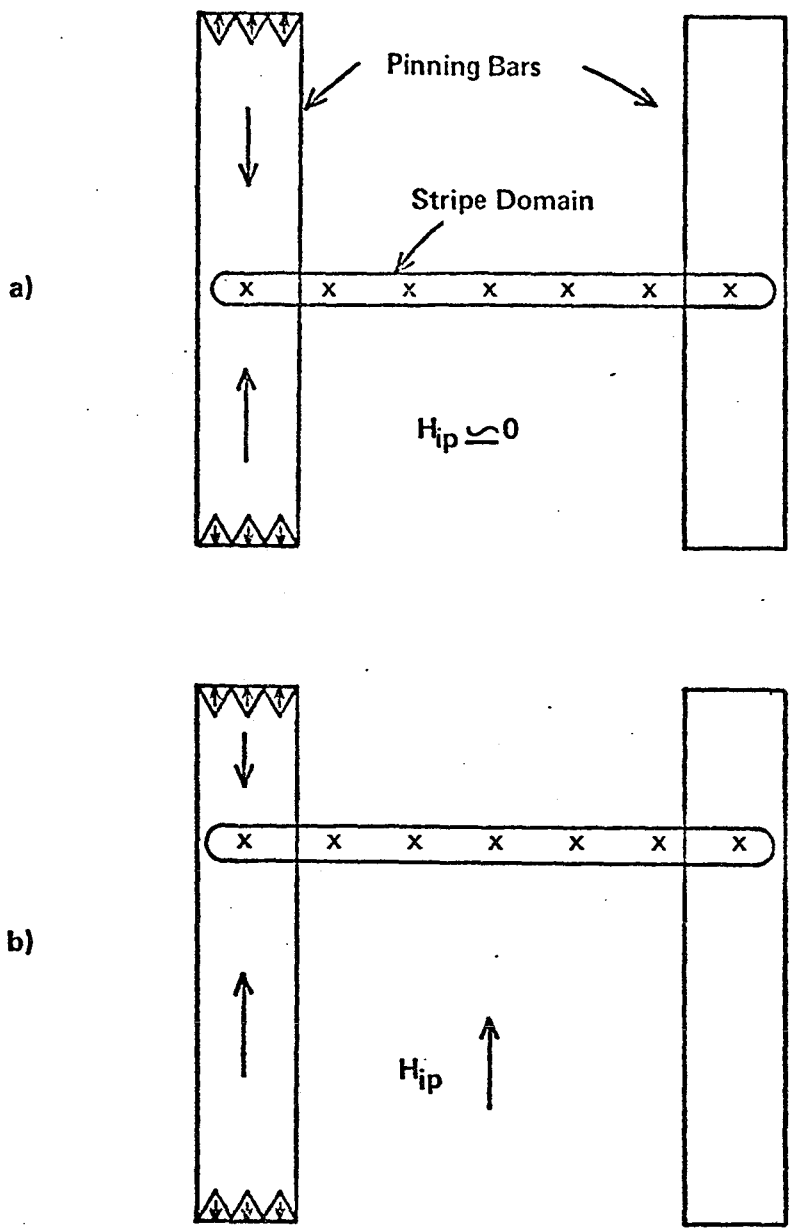

Figure 4.19 Simplified Representation of the Pinning Bar-Domain Interaction.

a) Domain Configuration with No In-Plane Field

b) Domain Configuration with an In-Plane Field Component Along the Length of the Pinning Bars.

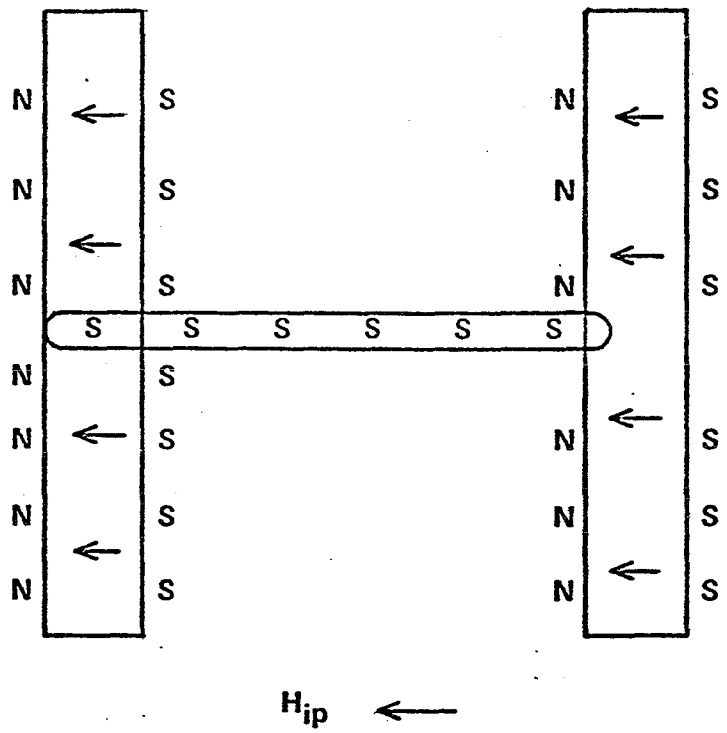

Figure 4.20 Simplified Domain Structure Using an In-Plane Field Perpendicular to the Pinning Bar

4.5 Garnet Materials

4.5.1 Objectives

Before device designs can be finalized, it is important to know the range of material parameters that are available in bubble supporting garnets. It is also very helpful to know the defect density in these materials, which will affect device yield, size, and required redundant circuitry. With multiple layer garnets, the coupling between layers must be known for material choice and layer thickness. It is the object of this section to determine the material parameters that are available, and how they influence the device design.

4.5.2 Garnet Survey

The two fundamental material parameters of bubble films are the saturation magnetization, M, and the characteristic length, ℓ. These are the two parameters independent of film thickness from which the other parameters important to bubble operation can be deduced.

A question important for multilayer bubble work is: "What combinations of $4\pi M$ and ℓ can be made?" Accordingly, a survey was made of garnet materials from Sperry Research Center and Univac Blue Bell, reported in two publications.[11,12] The results are listed in Table 4.1 on page 97.

When a graph is made of saturation magnetization, $4\pi M$, vs. characteristic length, ℓ, of these garnets, all the points fall on a single curve, as shown in figure 4.21. A mathematical relationship between the two parameters is found by plotting the natural logarithms of the two parameters, and the result is a straight line as shown in figure 4.22. The equation for that line is:

$$\ln 4\pi M = -.8125 \ln \ell + 4.67$$

or

$$\ell = \left(\frac{106.7}{4\pi M}\right)^{1.23} = \frac{313.8}{(4\pi M)^{1.23}} \quad . \qquad (4.1)$$

Although no garnet films in the survey were found that did not fit that equation, this does not necessarily mean that such films cannot be made. The impact of the survey, however, is that garnets that do fit the equation can be made over the whole range of $4\pi M$ and ℓ.

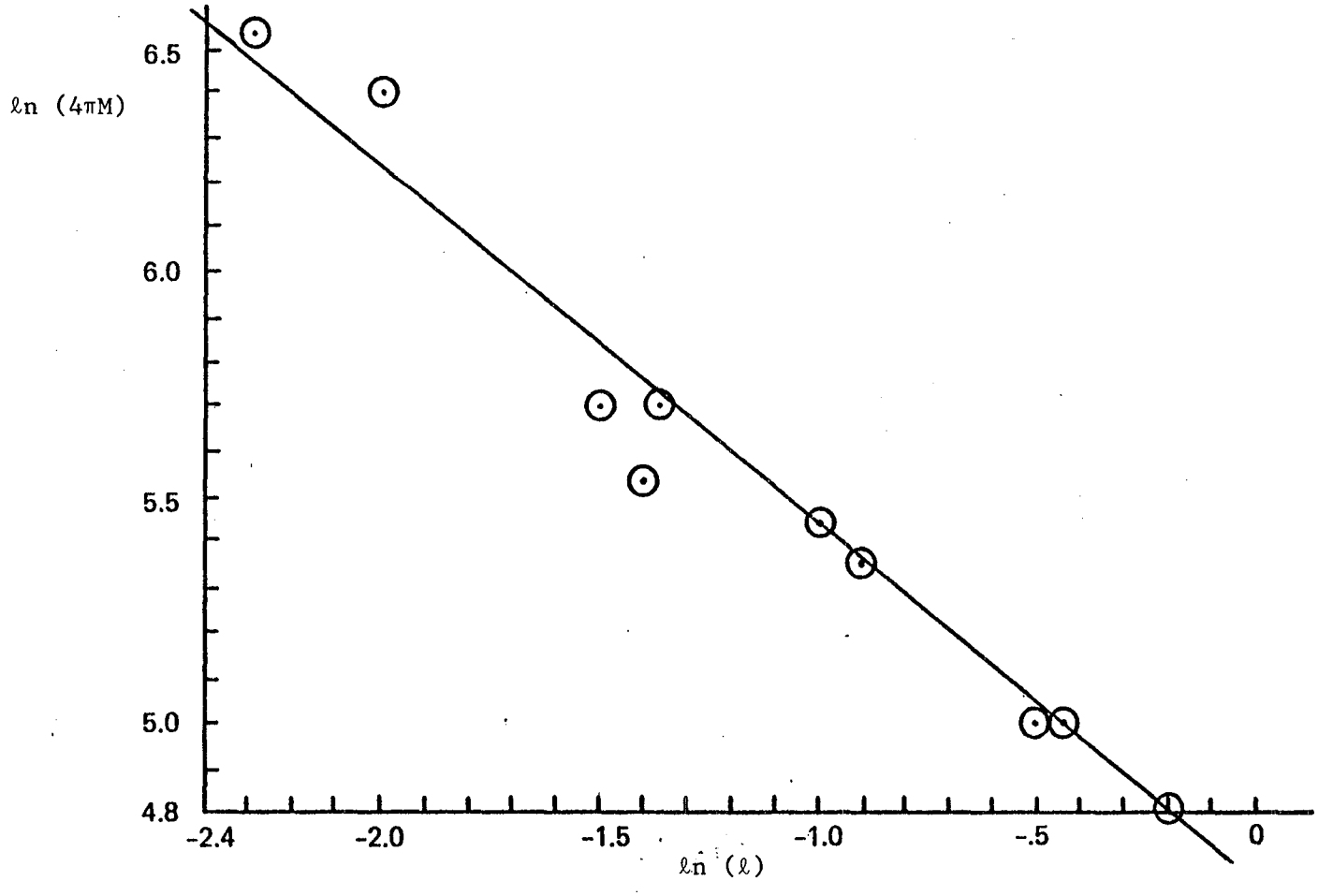

Figure 4.21 Magnetization vs. Characteristic Length of Typical Bubble Garnets

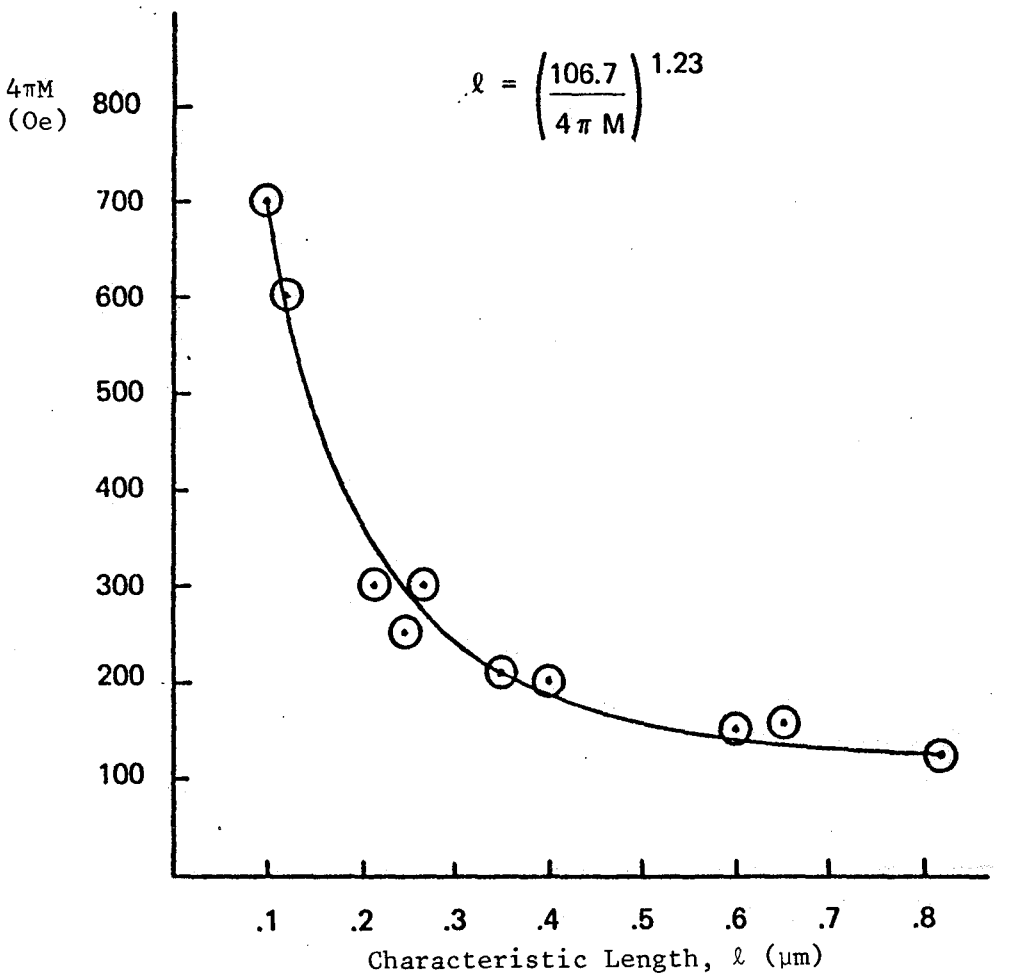

Figure 4.22 Magnetization vs. Characteristic Length of Typical Bubble Garnets.

TABLE 4.1

	4 M (Oe)	ℓ (μm)	H_k (Oe)	H (Oe)	Q	h (μm)
$(YSmLu)_3(GaFe)_5O_{12}$	300	.26	1500	∿200	5	
$(YSmLuCa)_3(GeFe)_5O_{12}$	300	.22	1500	∿200	5	
Ga	600	.13	1500	420	∿2.4	
CaGe	700	.10	1100	∿450	∿1.8	
YLaTm 7/25/74C	124	.822				6.0
YLaTM 8/1/73C	253	.37		165		4.6
YLaTM 4/23/73B	232	.37		128		3.8
YLaTM 4/23/73A	213	.40		104		2.8
YLaTM E412B	154	.65		86		6.9
$Y_{2.0}Sm_{1}Ca_{.9}Ge_{.9}Fe_{4.1}O_{12}$	154	.61				

4.5.3 Multiple Layer Garnets

Three magnetostatically coupled, one inch diameter, triple layer garnet films were made by the Sperry Corporate Research Center. Each film is comprised of two $(YSm)_3(GaFe)_5O_{12}$ magnetic layers separated by a Gadolinium Gallium Garnet (GGG) layer. The samples were made with different separation layer thicknesses, holding the thicknesses of both top and bottom magnetic layers constant at as close to 6μm as possible. Samples #1, 2, and 3 have a GGG epi-layer thickness of 2.25μm, 6.8μm, and 13.75μm, respectively.

These films settled one very important question, whether or not defect-free multilayer films can be made. The high qualities of the triple layer films can be seen in figures 4.23 through 4.27. The only defects are in the photographs, such as the scratch in the emulsion of figure 4.25f. Similar dust-free furnace facilities are presently being installed in the Sperry Univac facility in St. Paul.

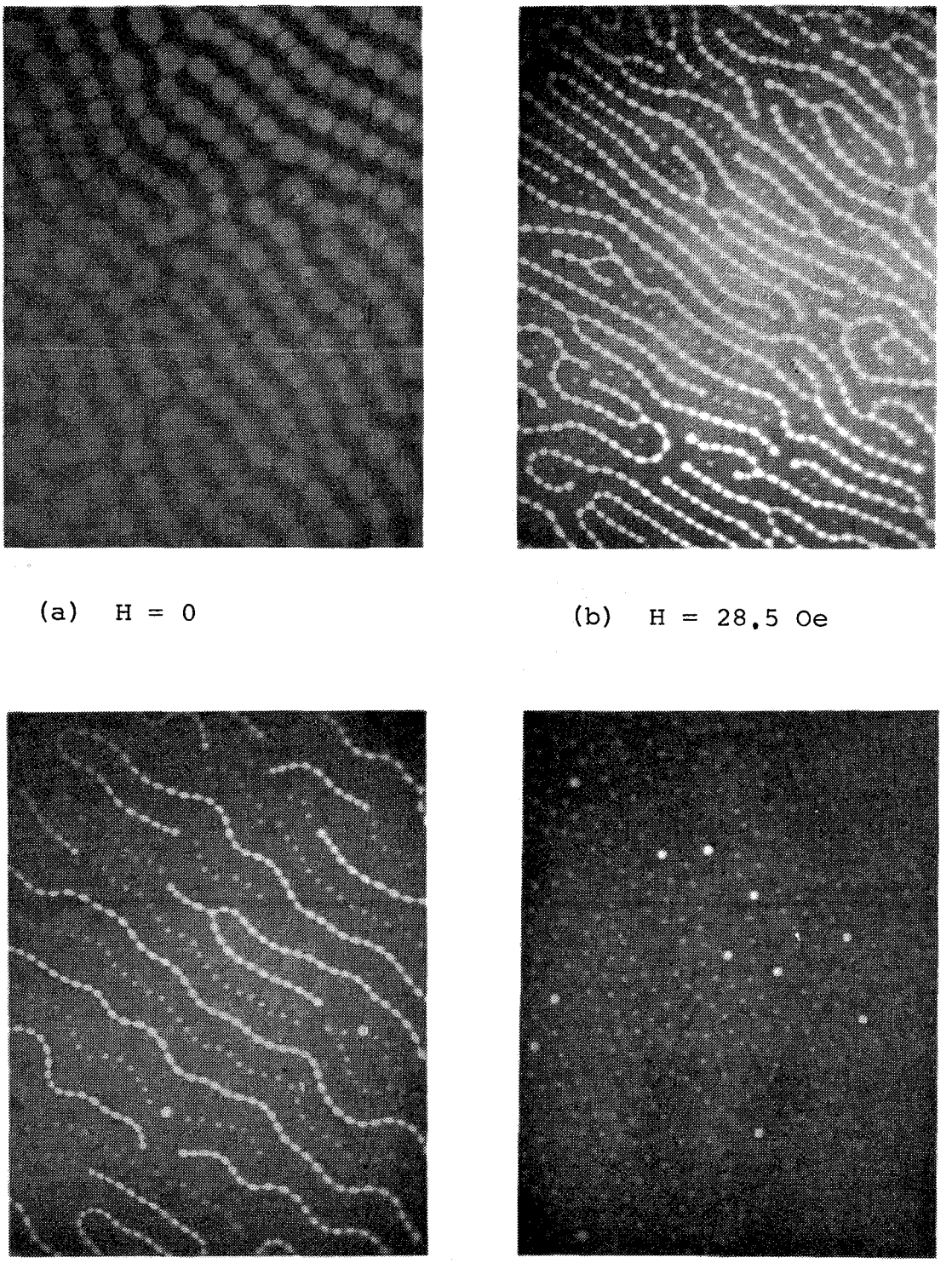

(a) H = 0

(b) H = 28.5 Oe

(c) H = 38 Oe

(d) H = 40 Oe

Figure 4.23 Domain Patterns in a Double Magnetic Layer Garnet with GGG Thickness = 2.25 microns.

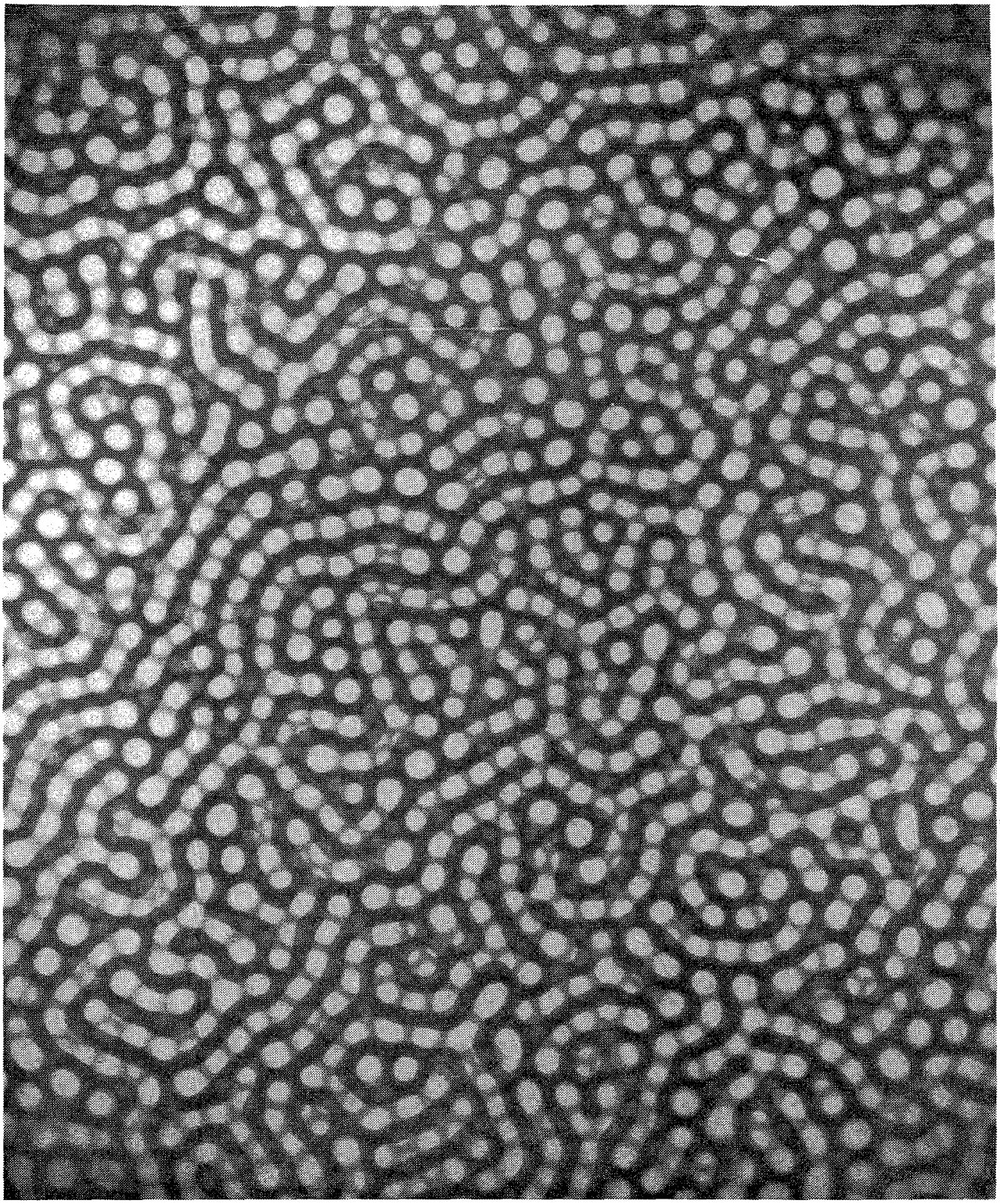

Figure 4.24 Double Magnetic Layer Garnet, with GGG Thickness of 6.8 μm, and H = 0.

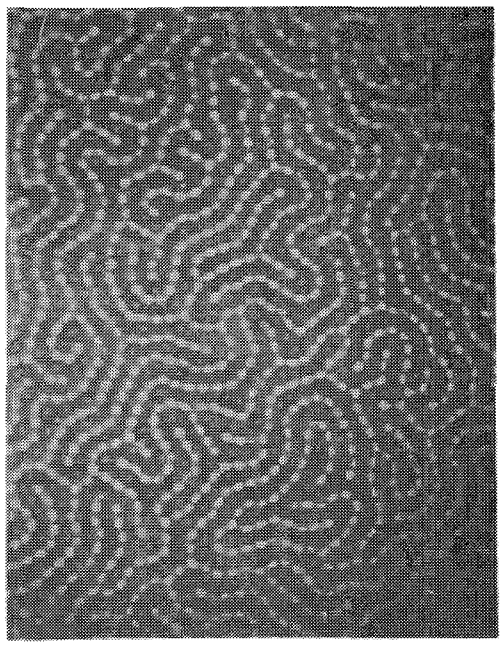

(a) H = 28.5 Oe

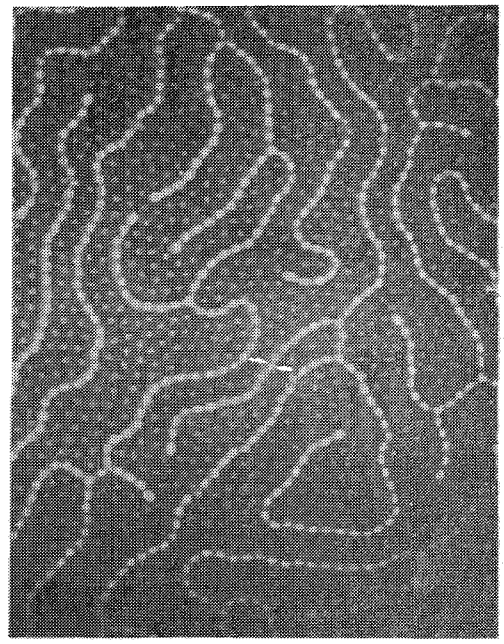

(b) H = 41.8 Oe

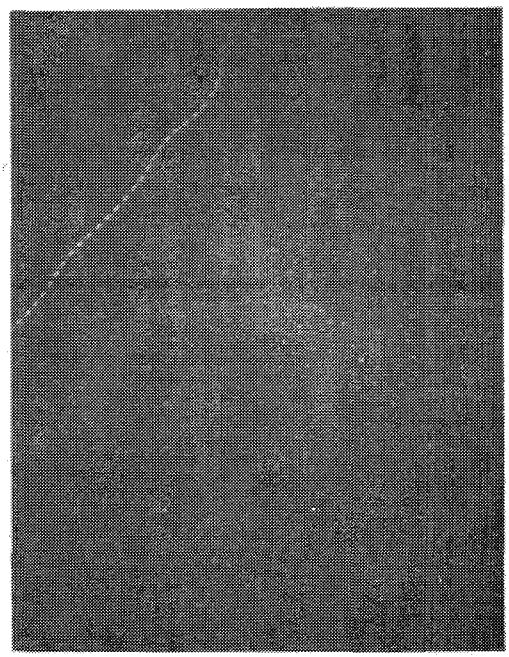

(c) H = 62.7 Oe

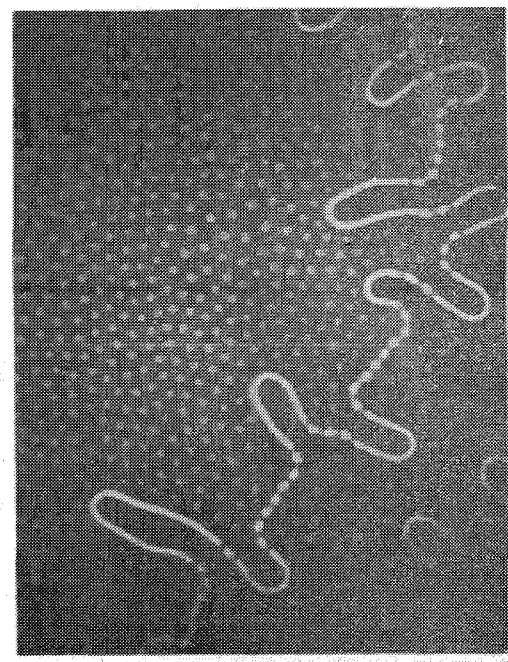

(d) H = 40.8 Oe

Figure 4.25 Domain Patterns in a Double Magnetic Layer Garnet with GGG Thickness of 6.8 μm.

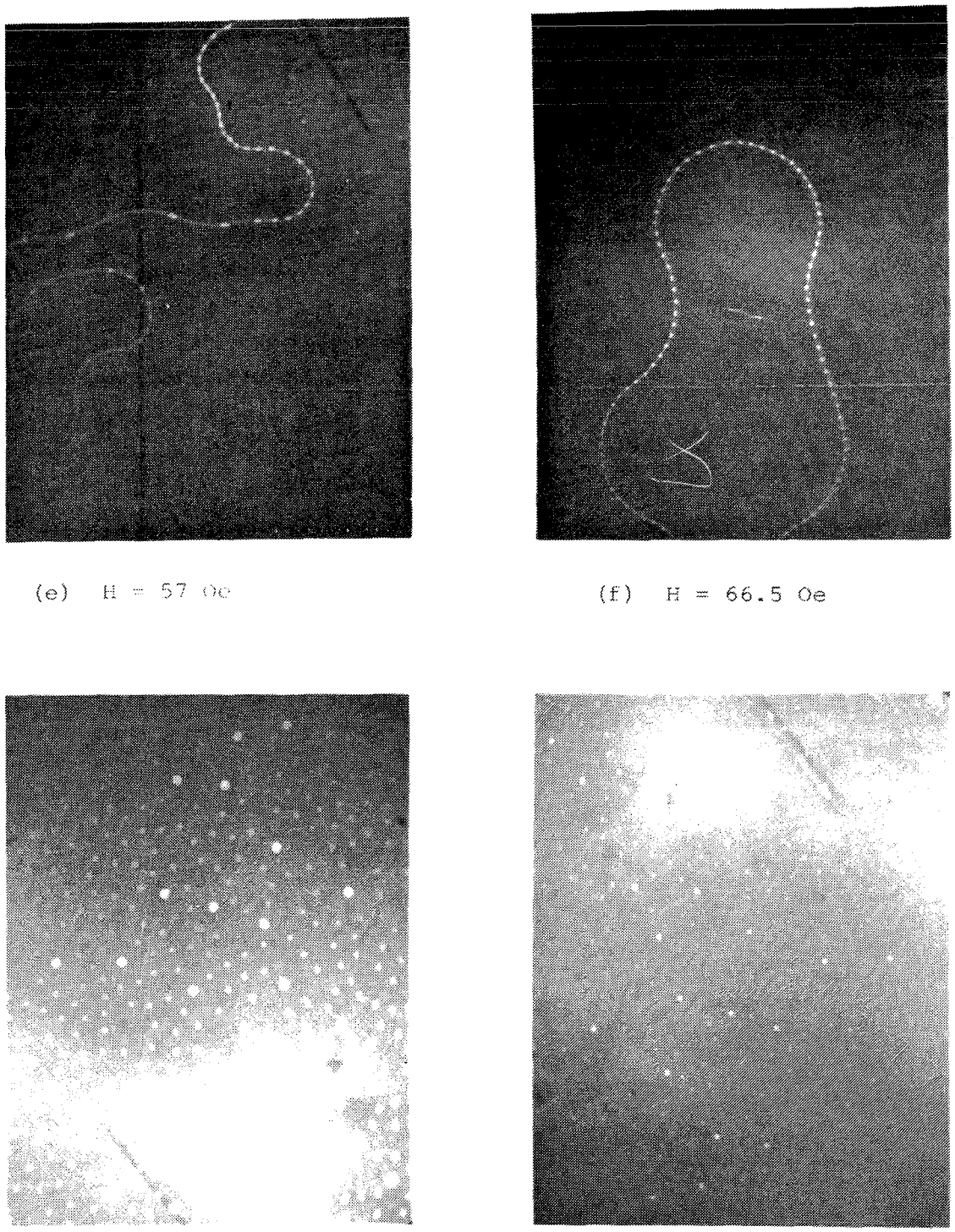

(e) H = 57 Oe

(f) H = 66.5 Oe

(g) H = 49.4 Oe

(h) H = 59.8 Oe

Figure 4.25 Domain Patterns in a Double Magnetic Layer Garnet with GGG Thickness of 6.8 μm.

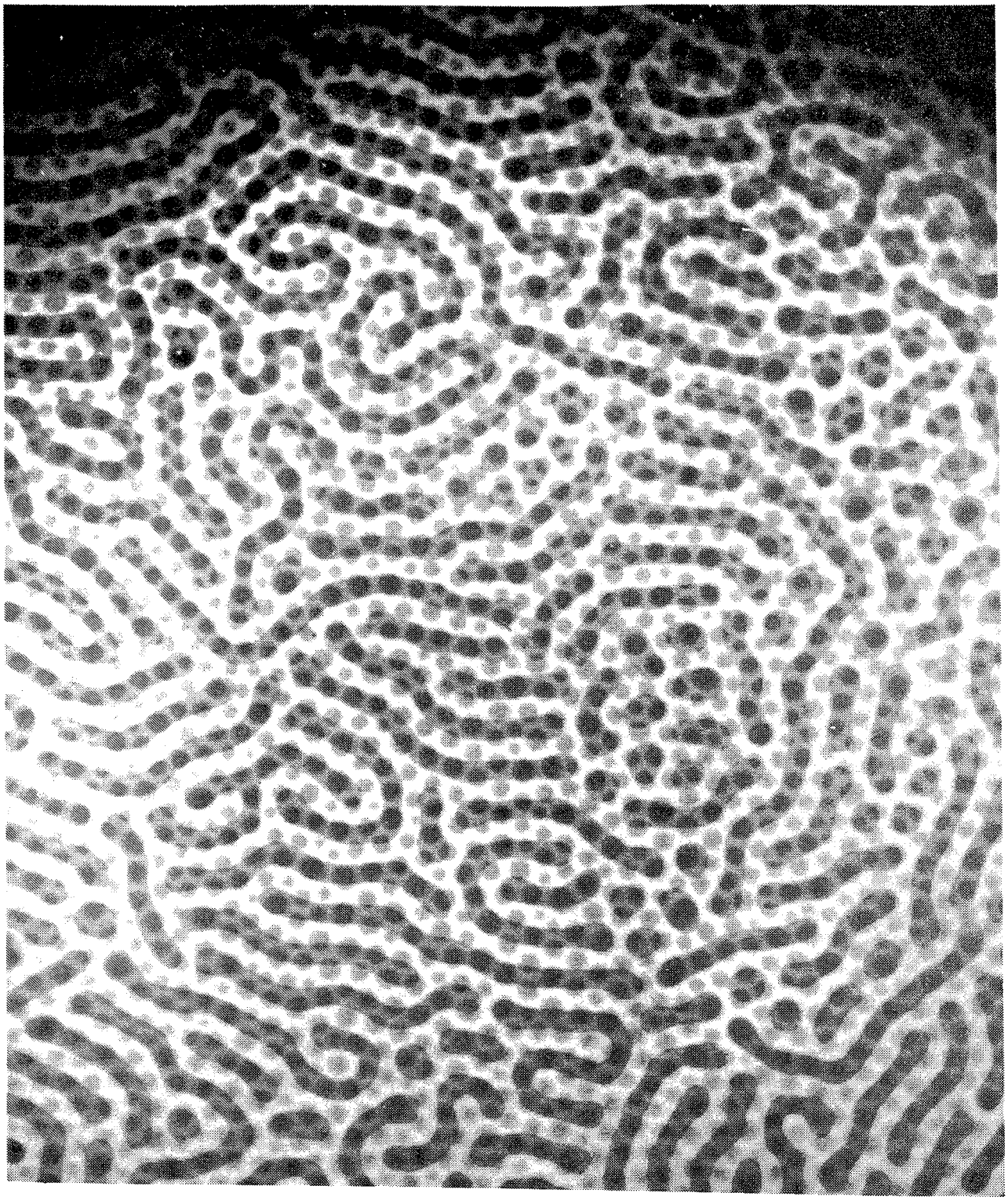

Figure 4.26 Double Magnetic Garnet Layers, with GGG Thickness of 13.75 μm, and H = 0.

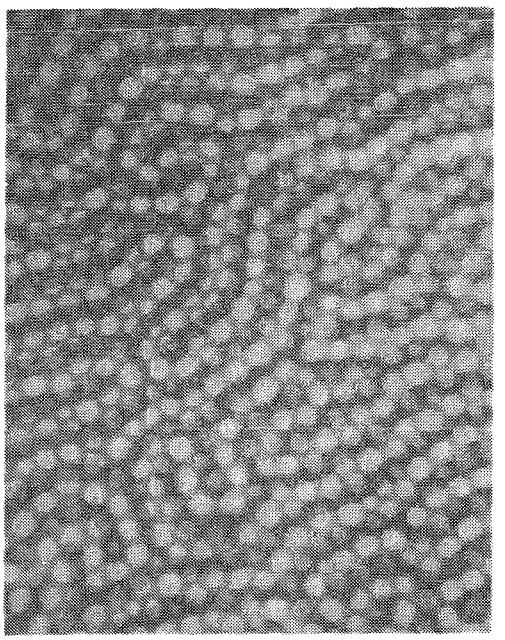

(a) H = 0

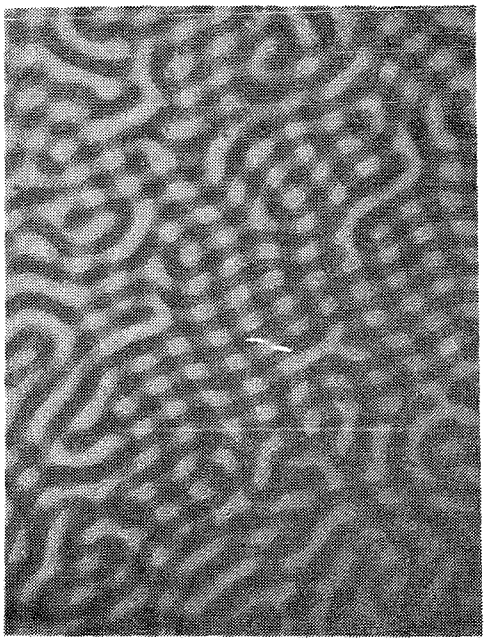

(b) H = 0, different area

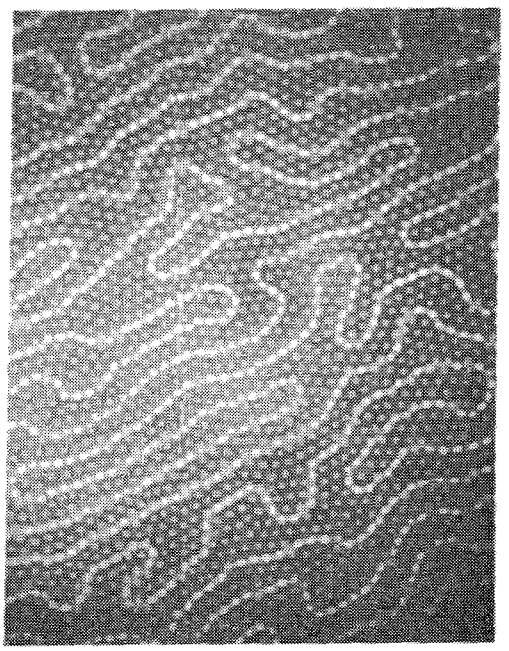

(c) H = 28.5 Oe

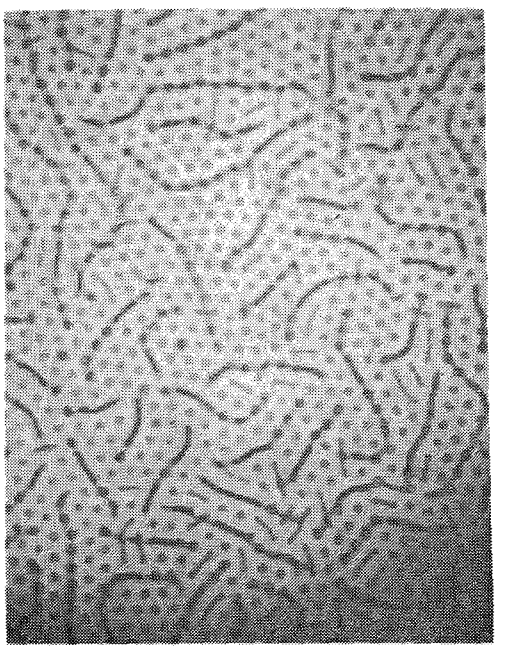

(d) H = 30.4 Oe

Figure 4.27 Domain Patterns in a Double Magnetic Layer Garnet with GGG Thickness = 13.75 μm.

The magnetostatic coupling between the two magnetic layers varies from sample to sample, being greatest for the smallest GGG epi-layer, and weakest for the largest. Figure 4.23 shows bubbles and stripes in the most strongly coupled triple layer film, sample #1 with 2.25μm GGG separation. Figure 4.23a is 219μm wide, while figures b, c and d are 438μ wide. Figure 4.23a shows bubbles strongly coupled to stripes at zero applied field.

Figure 4.23b shows the stripes collapsing when the normal applied field H is 28.5 Oe. When the stripes contract, they do so in jerks, ejecting a bubble each time. Bubbles are left behind by the receding stripes. Note that the uncoupled bubbles are smaller in diameter than the coupled bubbles. This is because the coupling field from the stripe is opposite to the normal applied field and tends to enlarge the bubble. Figure 4.23c, H = 38 Oe, shows some of the stripes have lost all but one of their bubbles and have collapsed to become double bubbles. These appear in the micrograph to be much brighter and larger than the single bubbles. They are brighter because the polarized light is going through two bubbles instead of one, and are larger because of the stray field of each bubble enlarges the other. Figure 4.23d, H = 40 Oe, shows all the stripes have collapsed, leaving only coupled and uncoupled bubbles.

Figure 4.24 shows coupled bubbles and stripes at zero bias field for sample #2, a triple-layer film with a 6.8μm thick GGG epi-layer. Note the many different coupled bubble configurations. The coupling is not as strong for this structure as for sample #1. Figure 4.25a shows this same sample with an applied normal field of 28.5 Oe, and figure 4.25b at an applied bias of 41.8 Oe. The stripes are contracting, disgorging their bubbles as they do so. This contraction is jerky, but not as jerky as for the sample of figure 4.23b. This is because the magnetostatic coupling between stripes and bubbles is not as strong for the structure with the 6.8μm GGG epi-layer as for the 2.25μm epi-layer. Figure 4.25c is at 62.7 Oe; some of the bubbles are beginning to collapse. The bias field was then lowered to 40.8 Oe, which is below the run-out threshold for the coupled stripes, and is shown in figure 4.25d. The stripes expand via the kink instability, pushing the uncoupled bubbles out of their way. Figure 4.25e shows the domain pattern after the bias is raised to 57 Oe; this is the run-out threshold for the bubbles coupled to the stripes. Figure 4.25f has H = 66.5 Oe, and the non-coupled bubbles have collapsed, leaving only the coupled stripes and bubbles. The scratch on the micrograph is on the photograph, not on the sample. Figures 4.25g and h show bubbles coupled to other bubbles (double bubbles) and free bubbles. From the difference in diameter between coupled and free bubbles, the coupling field can be calculated. All the micrographs in figure 4.25 are 438 μm wide.

Figure 4.26 shows triple layer sample #3, having a GGG epilayer thickness of 13.75μm, resulting in the two magnetic layers being relatively uncoupled. The micrograph is 438μm wide. Figures 4.27a and b are 219μm wide, and show different film areas at zero bias. Figure 4.27c is 438μm wide and has H = 28.5 Oe. The stripes here move with only a small coupling to the bubble lattice. Somewhat greater coupling is exhibited in figure 4.27d, in which the applied normal field is 30.4 Oe. The probable cause for this increased coupling is that the bubble lattice is less dense in figure 4.27d than in figure 4.27c.

4.5.4 Magnetostatic Coupling in Multilayer Garnets

To characterize a triple layer garnet it is necessary to quantitatively evaluate it to determine the magnetic parameters of each layer, and especially to determine experimentally the magnetostatic coupling between domains in one layer and those in the other. This section describes how this can be done, and presents the measurements for the garnet layers whose micrographs are shown in the previous section.

The thickness of single layer garnets are usually measured from optical interference patterns. However, the pattern from a substrate with three layers on each side is prohibitively complex. The most accurate method of direct measurement is with a scanning electron microscope. An indirect method of thickness measurement of the magnetic layers can be made by measuring the bubble collapse and run-out thresholds, measuring the bubble diameter, and the magnetostatic coupling can also be calculated from these thresholds and bubble diameters with these formulae. The relevant definitions and formulae have been presented in section 3.2.2.

Suppose that the thickness of each layer is known. The radius of the bubbles at the collapse threshold is measured by using a comparator on a micrograph, and this yields X_o. Equation 3.5 is inverted to give:

$$\lambda = \frac{3}{(3/2 + 1/X_o)^2}$$

and generates both λ and ℓ. For example, for the top layer of film #2, $X_o = 0.35$, $\lambda = 0.158$, and $\ell = .95\mu m$. Next, equation 3.4 yields $\tilde{H}_o = H_o/4\pi M$. In the case of the top layer of the film #2 this is $\tilde{H}_o = 0.43$, so $4\pi M = 146$ Oe. An alternative method which does not require a direct thickness measurement is to measure the ratio of the collapse threshold to the run-out threshold, and

find λ from the graph of figure 4.28, which is calculated from equations 3.4 and 3.7. Then equation 3.3 or equation 3.5 is used to find $X = r/h$ at a given field, and use the measured value of the bubble radius r to find the film thickness h.

Equation 3.3 gives the normalized radius of a bubble as a function of normalized applied field. This is shown in figure 4.29 for $\lambda = 0.158$. By using the graph of figure 4.29, the field applied to a bubble is determined merely by measuring the radius of the bubble. Notice in the micrographs of figure 4.25 that the coupled bubbles are larger than the uncoupled bubbles. By measuring the radius of each, and using figure 4.29, one can calculate the coupling field. For example, the coupled bubbles in figure 4.25h have a normalized radius of $X = 0.5$ while the uncoupled bubbles have a normalized radius of $X = 0.35$. These correspond to $H = 0.41$ and 0.43, respectively, in figure 4.29, and thus the difference in bias field is $4\pi M \cdot (0.43-0.41)$ or 2.9 Oe. The coupling field between carrier bubbles and data bubbles depends on the bubble size; the smaller the bubble diameter, the smaller the coupling field. Since the bubble size decreases with increasing bias field, the coupling field also decreases with increasing bias field. This is shown in figure 4.30 for sample #2 (thickness of GGG spacer is 6.8μm).

When a thinner GGG spacer is used, the coupling strength is increased. For example, the bubbles in figure 4.23d (sameple #1 with 2.25μm GGG layer) have a coupling strength of 11.7 Oe.

The coupling field of stripes to bubbles is expected to be larger than that of bubbles to bubbles. For example, the coupling field from a stripe to a bubble in figure 4.23b is 16 Oe.

The principal conclusions drawn from the two preceding sections are: (1) High quality triple epi-layer garnet films can indeed be grown, provided the proper equipment is employed; (2) All the relevant parameters of these triple layer films can be measured, including the coupling field of one domain to the other; (3) This coupling field decreases as the bias field increases; (4) The coupling field depends on the GGG epi-layer spacer thickness; (5) Bubbles can be uncoupled from stripes by raising the bias field past the stripe run-out threshold; and (6) The collapse threshold of coupled bubbles is larger than that of uncoupled bubbles by the value of the coupling field. This property may be useful in detecting bubbles in a data layer buried next to the substrate.

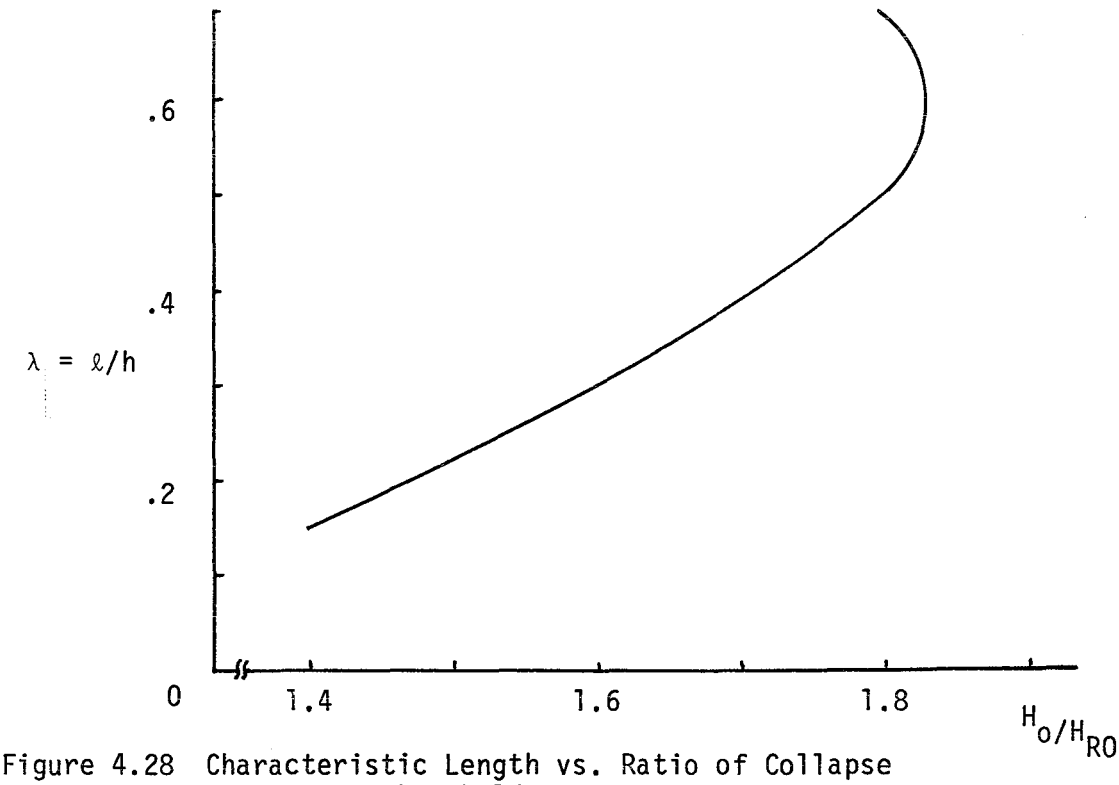

Figure 4.28 Characteristic Length vs. Ratio of Collapse to Run-Out Threshold.

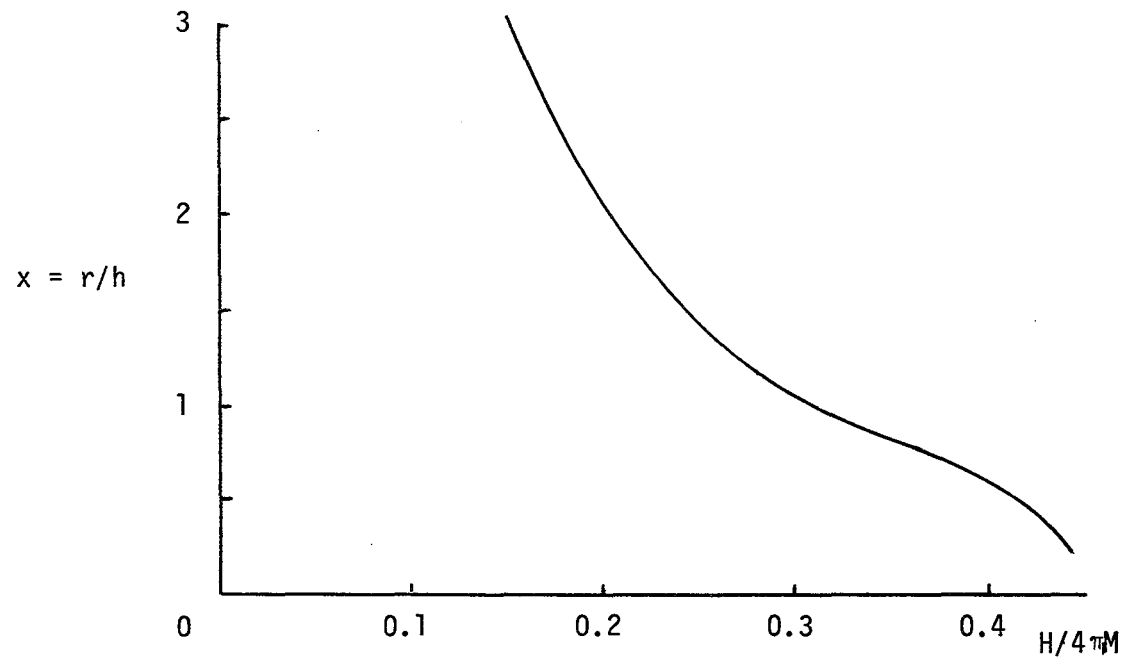

Figure 4.29 Bubble Radius vs. Applied Field for $\lambda = 0.158$.

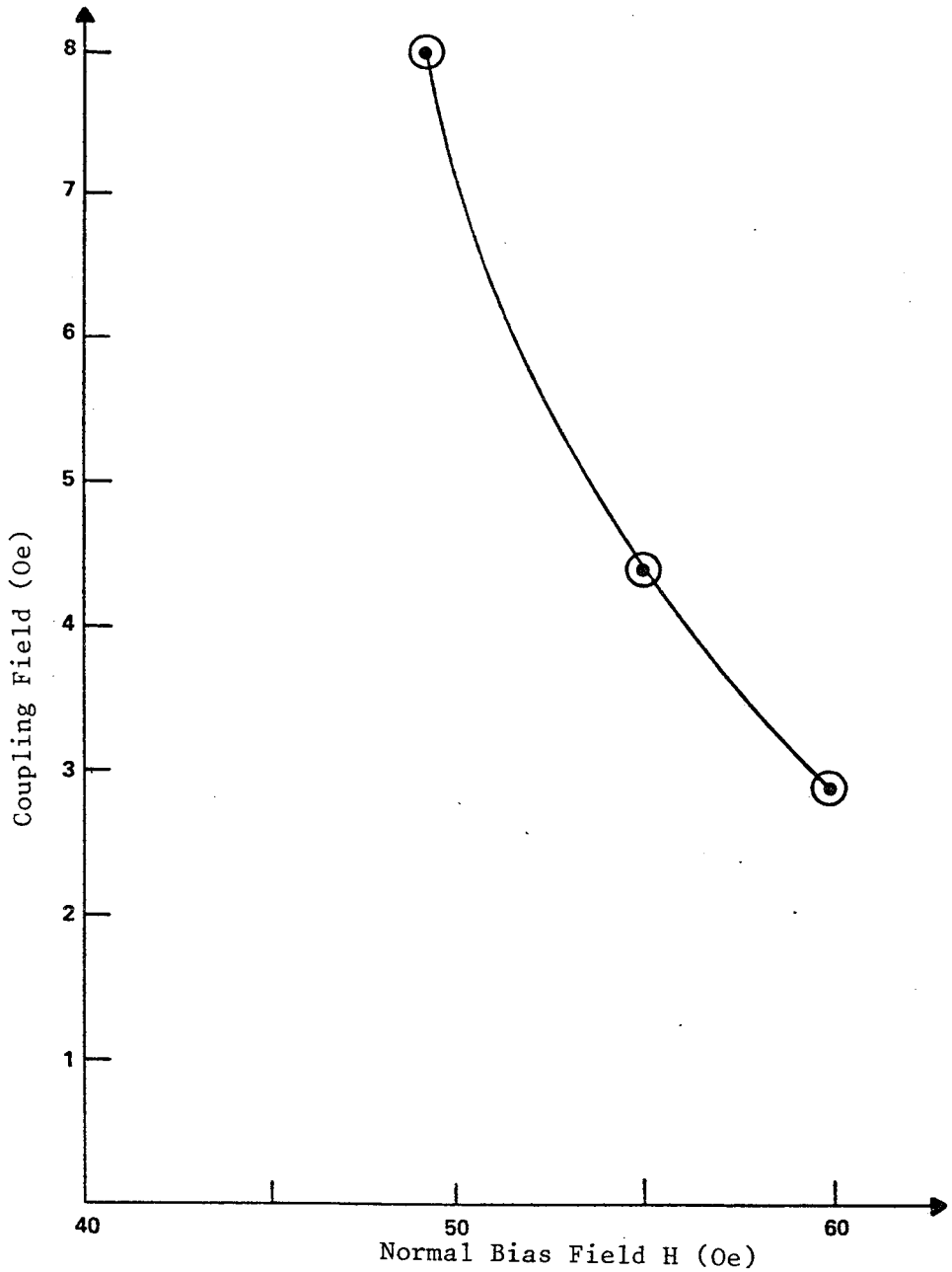

Figure 4.30. Coupling Field between Bubbles vs. Normal Bias Field Field for Sample No. 2.

4.5.5 Diffusion in Triple-Epi Garnets

More films were fabricated, each with two epitaxial magnetic garnets separated by an epitaxial GGG layer. The two magnetic garnet layers on each film were supposed to have equal properties. This is necessary for device operation. If the collapse threshold of the inner layer is smaller than the run-out threshold of the outer layer, device operation will be unsuccessful. After several attempts, the properties of the inner magnetic layer were measured before and after deposition of the GGG layer. The properties of the inner magnetic layer were found to be changed after deposition of the GGG. The changes are consistent with a decrease in the thickness of the first layer after the GGG deposition. A possible mechanism for this change is diffusion of some of the iron atoms at the interface from the magnetic garnet to the GGG. The result is that the collapse and run-out thresholds of the outer layer are higher than those of the inner layer.

In order to remedy this, the outer layer of one of our triple epilayer garnets (film #6) was thinned in order to adjust the collapse threshold of the outer layer to equal that of the inner layer. This thinning was done on the ion mill apparatus in small steps. After each step all the properties of each layer were measured. These properties include the collapse threshold of single bubbles in the outer layer, collapse of double bubbles, collapse threshold and run-out threshold of bubbles in the inner layer coupled with stripes in the outer layer, run-out threshold of single bubbles in the inner layer, run-out threshold of double bubbles, and film thickness. Not all the properties can be accurately measured for all outer layer thicknesses. For example, when the run-out threshold of the outer layer is higher than the collapse threshold of the inner layer, single bubble characteristics of inner bubbles cannot be measured. The results of this experiment are shown in figure 4.31. Film #6 started out with the collapse threshold for double bubbles lower than the run-out threshold for carrier bubbles. After the fifth thinning, the collapse thresholds for the outer layer, the inner layer, and for double bubbles is virtually identical. The run-out threshold for double bubbles is higher than either the inner or outer layer run-out threshold. In particular, the run-out threshold of the carrier bubble layer (the outer layer) is so much lower than the double bubble run-out threshold that we were unable to measure the carrier layer run-out threshold; double stripes ran out first, filling up the garnet. However the carrier layer run-out threshold can be estimated by extrapolating the run-out curve from greater thicknesses: This value of the run-out threshold for the carrier layer is fourteen Oersteds lower than the run-out threshold for double bubbles. This indicates the validity of the proposed method of detecting the presence or absence of a bubble in the data layer coupled to a bubble in the carrier layer by applying a pulse to determine if the bubble will run out.

Table 4.2 Properties of Triple Layer Garnets.

Set	Growth Layer	Magnetic Layer No.	Thickness of GGG (μm)	Garnet Thickness (μm)	Stripe Width (μm)	H_o (Oe)	H_k (Oe)	$4\pi M$ (Gauss)	Q	Coupling
Desired Values:		1		6.0	3.7	60	120	100	1.2	
		2		6.0	6.0		530	120	4.5	
1	1-15-81A	1	4	6.0	8.25	34	295	82	3.6	Weak
	1-27-81C	2		5.0	3.6	100	210	161	1.3	
2	1-15-81B	1		5.6	5.6	47	147	91	1.62	Weak
	1-29-81C	2		5.0	7.0	38	872	92	9.48	
3	12-5-80C	1	4	5.0	3.15	174	344	264	1.3*	Weak
	1-30-81A	2		5.0	3.5	155	387	246	1.57	
4	1-14-81A	1	4	6.2	3.6	139	232	204	1.14	Weak
	1-30-81B	2		5.0	6.0	52	668	113	5.91	
5	1-20-81A	1	4	+						Weak
	2-2-81A	2		5.0	11.5	16.5	1337	59	22.7	
6	1-14-81B	1	4	5.68	5.6	63	466	121	3.85	Weak
	2-2-81B	2		5.0	4.0	69	340	117	2.91	
7	1-26-81B	1	2	4.2	4.3	69	358	135	2.65	Strong
	2-2-81C	2		5.0	5.0	71.5**	492	138	3.57	
8	1-23-81C	1	3		4.3	62.5	451	135	3.24	Strong
	2-2-81D	2		5.0	6.5***	64	533	147	3.62	
9	1-27-81A	1	3	4.55	4.4	84	231	159	1.45	Strong
	2-2-81E	2		5.0	5.4***	65	537	132	4.07	
10	1-27-81B	1	3	4.55	4.2	72.5	293	133	2.2	Strong
	2-2-81F	2		5.0	5.2***	63	538	125	4.3	
11	1-26-81C	1	3	5.0	4.3	77.5	292	137	2.13	Strong
	2-2-81G	2		5.0	4.8***	80	418	151	2.77	
12	1-26-81D	1	3	5.15	3.9	85.5	211	142	1.48	Strong
	2-2-81H	2		5.0	4.5***	80	376	145	2.59	
13	1-26-81A	1	3	4.5	3.8	89	188	156	1.21	
	2-2-81B	2		5.0	4.0	106	192	180	1.07	

* These measurements made before 3G added. All other Layer 1 measurements were made after 3G added.
** This is collapse field for double bubble.
*** This is stripe width of double stripe.
\+ Very low $4\pi M$, non-uniform stripes.

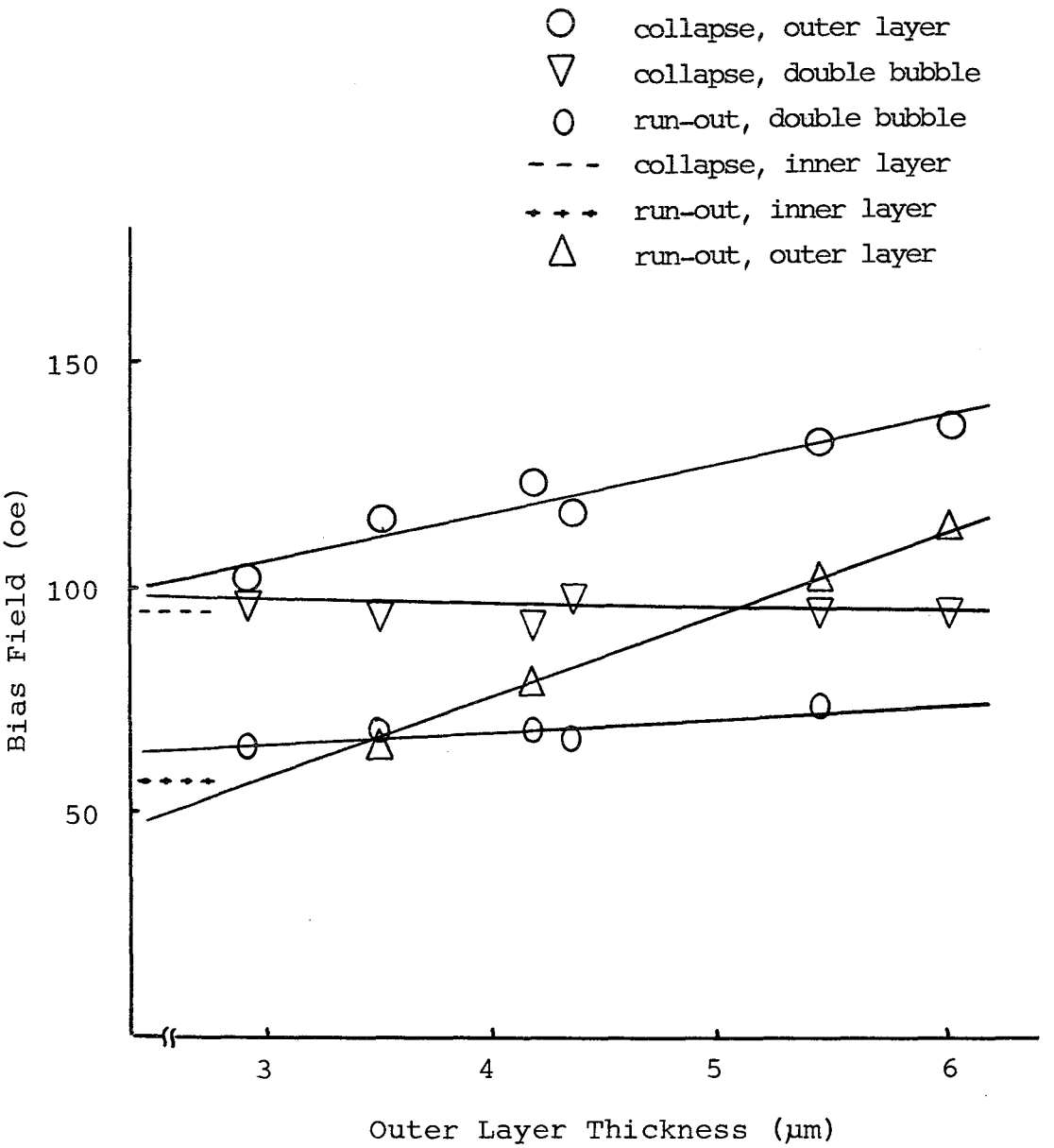

Figure 4.31 Thresholds in a Triple Epi-Layer Garnet as a Function of Outer Layer Thickness.

4.5.6 Observations of Double Bubbles

Sometimes when a double bubble collapses in a triple epi-film, only one layer collapses, leaving a single bubble. In that case the remaining single layer bubble will not collapse until its collapse threshold is reached. In the case of film #5, that threshold is 15.1 Oe higher than that of the double bubble. However, sometimes the double bubble collapses entirely, removing the high threshold bubble as well. This effect is not understood. One possible explanation envolves the in-plane stray fields of the bubbles. Another involves the stray fields from neighboring bubbles.

Another unexpected phenomenon is the combination of bubbles on a high threshold film coupled with stripes in a low threshold film. This is just the opposite that one would expect. This phenomenon occurs when a bubble lattice exists in the high threshold film. When the bias is lowered, a stripe in the low threshold film runs outs under the lattice, capturing the bubbles. When the bias is raised, the stripe runs in, dropping the high threshold bubbles one by one.

4.5.7 Exchange Coupled Films : Experiment:

Approximately 40 exchange coupled films have been made in our St. Paul laboratory to date. This experimental program was initiated to do two things: (1) verify the theory presented earlier, and (2) make an exchange coupled film suitable for device applications. Our latest films, while not perfect, nevertheless, satisfy these goals.

Exchange coupled films have three advantages over triple epilayer (stray field coupled) films: (1) the exchange coupled films have only two epitaxial layers instead of three, which means lower costs and higher yields, (2) double bubbles can be written with relatively low currents in exchange coupled films even when the anisotropy field is large, in contrast to the triple epilayer films (in the latter the anisotropy in the buried bubble layer must be very small which implies a very narrow temperature operating region); and (3) in exchange coupled films, the double bubble diameter can be just as small as the diameter of single bubbles, provided the film parameters are correct, and the bias field is above a critical value. In such a film the buried layer has lower magnetization and higher anisotropy than the outer layer. A bubble that does not extend completely through both layers has a capping wall. If the capping wall is in the outer layer, we call the bubble a single bubble. If the capping wall is in the buried layer, we call the bubble a double bubble. The capping wall is repelled by the interface between layers, no matter which side of the interface the capping wall is on.

Because the anisotropy is larger in the buried layer, exchange energy of the capping wall is less when it is in the outer layer, and a capping wall must overcome an energy barrier to cross from the outer layer to the buried layer. On the other hand the magnetization in the buried layer is less and a capping wall in that layer finds a magnetostatic repulsion from the poles at the interface; this repulsion becomes larger the closer the capping wall is to the interface. Thus, two bubbles can exist side by side, one with the capping wall in the buried layer, the other with the capping wall in the outer layer. In each case the capping wall is very close to the interface, and the two bubbles look exactly the same in the microscope. However, when the bias field is lowered past a certain threshold, the capping layer in the buried layer leaves the interface and goes to the farthest side of the buried layer, so that the bubble extends through both layers. The bubble then is larger and much brighter in the microscope than the other bubble which remains unchanged.

Film #02/13/81 on Film #01/13/81, displays this property. The specifications to the crystal grower were for the buried layer to be 7μm thick with an H_k of 1200 Oe and a $4\pi M$ of 100 Oe, while the outer layer was to be 7μm thick with an H_k of 400 Oe and a $4\pi M$ of 200 Oe. Because the films are coupled strongly we were unable to measure the individual parameters after the double film was grown.

The run-out threshold of single stripes in the outer layer was approximately 75 Oe. If the bias field was lowered to 63.5 Oe a string of bubbles in the buried layer appeared on the stripes in the outer layer. The field from the bubbles immediately cut the stripes, leaving only a string of double bubbles. If the bias field is increased to 89 Oe the double bubbles undergo an abrupt diameter decrease and become much dimmer. However when the bias field is lowered slightly, this change is reversed and they appear as before. This reversability holds up to 93.5 Oe. If one slightly exceeds that value the capping wall penetrates the interface and a single bubble results. This single bubble does not convert to a double bubble even when the field is lowered to the single stripe run-out threshold of 75 Oe. The single bubbles collapse at 94 Oe.

Figure 4.32 illustrates these changes. The bubble diameter was measured as a function of applied bias field, by use of a microscope with a traveling eyepiece. These measurements were made on a double bubble and a single bubble in close proximity and reasonably isolated from other domains. The abrupt diameter change of a double bubble is shown when the capping wall travels from the bottom to the top of the buried layer. The transition across the interface doesn't occur until almost the collapse threshold.

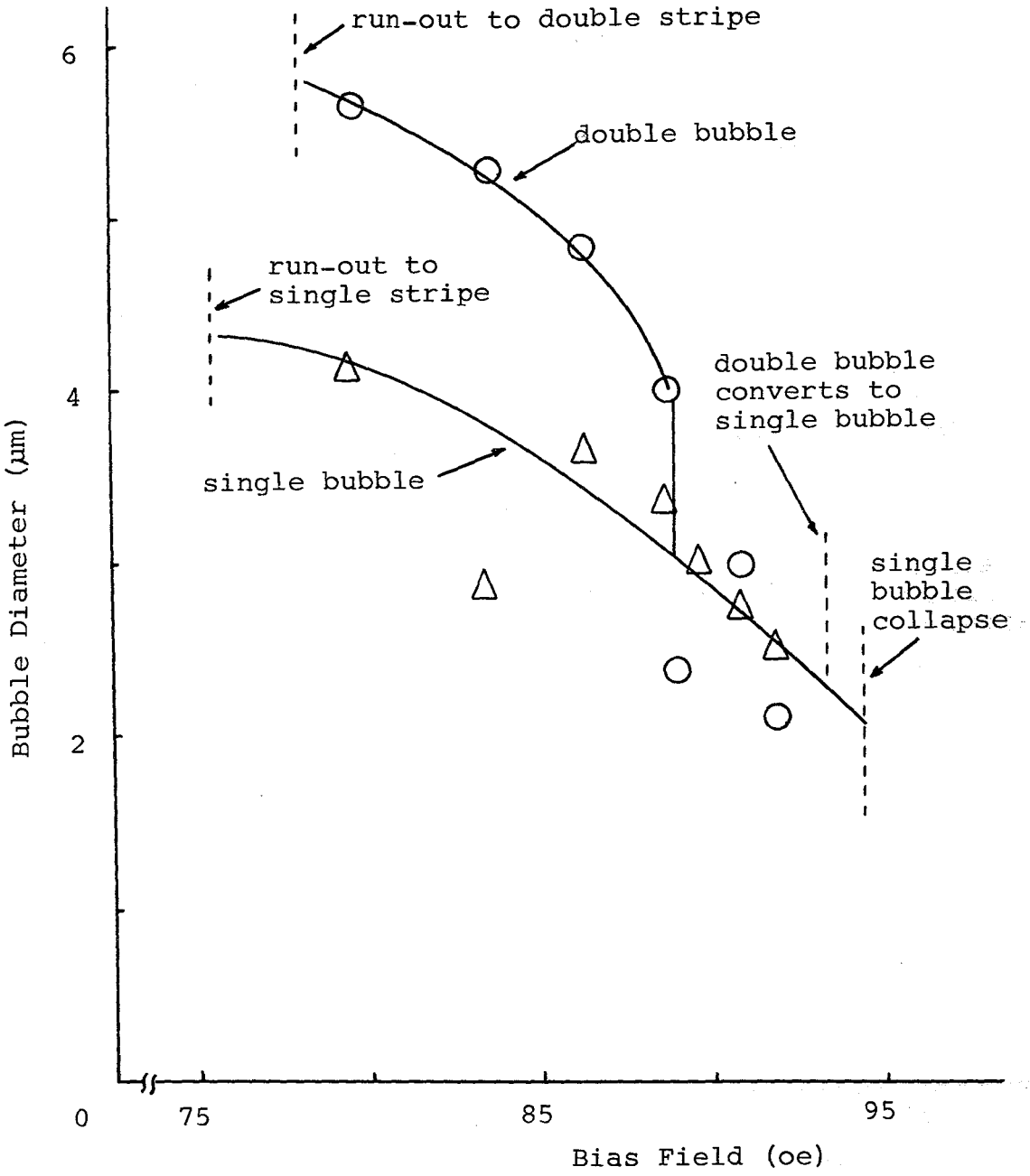

Figure 4.32. Bubble Diameter Changes with Applied Bias Field.

Another illustration of these changes is given in figure 4.33 for film #5-17-81A on film #5-15-81. The cap position can be inferred from the Faraday rotation of a bubble, the size of the bubble, and the threshold for conversion from single to double bubble or vice-versa. Figure 4.33 shows the hysteresis of the cap position as a function of normal bias field. There is a considerable region over which a bubble with the capping wall on one side of the interface can coexist with a bubble with the capping wall on the other side of the interface.

Figures 4.32 and 4.33 demonstrate the essential features of the theory of section 3.2.3. Exchange coupled films were used as well as triple epi-films for the memory element test vehicles of section 6.

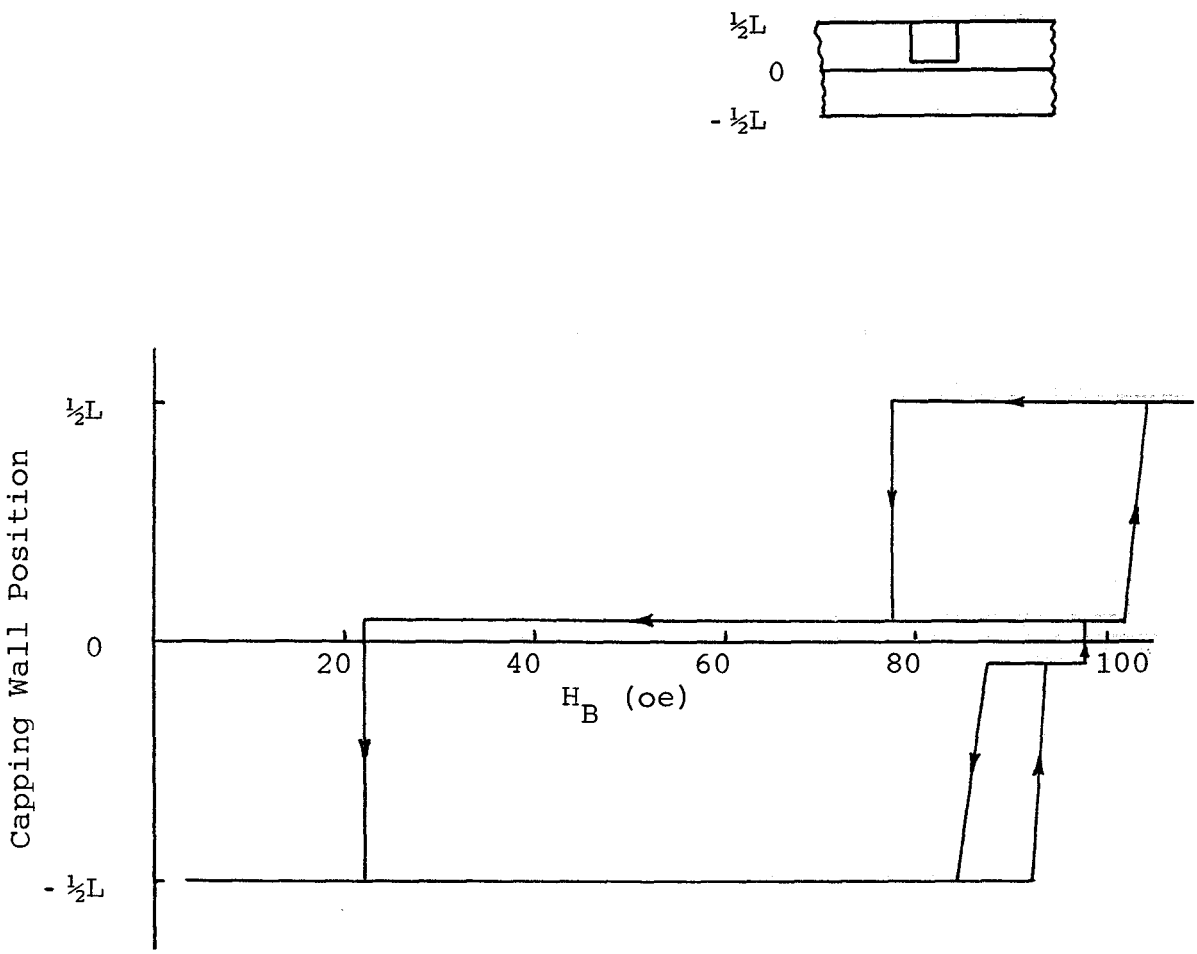

Figure 4.33 Hysteresis in an Exchange Coupled Garnet Showing the Position of the Bubble Capping Wall as a Function of Normal Bias Field.

5. Test Vehicles

5.1 Introduction

Various test vehicle circuits have been designed with the intent of propagating rows of stripe and bubble domains. Each circuit contains current accessed generators for stripe domains and bubble domains, in addition to current accessed circuitry for propagating stripe domains by translating the ends of each stripe domain. A general representation of the device design is illustrated in Figure 5.1.

Stripe domain generators consist of a set of long, narrow conductors, which are also employed to push and pull the newly formed stripe domain into the storage area. Bubble domain generators are of the hairpin design, and generally are connected in series for this series of test circuits. Several bubbles are generated at the same time with this arrangement, and does not represent the design which will be eventually utilized to insert data in the storage area.

Stripe domain propagation circuits have many designs, which include magnetically assisted circuits, double layer serpentine circuits, and various circuits with magnetic bias for stripe domain end pinning. Test results of several test vehicles are presented in the following paragraphs.

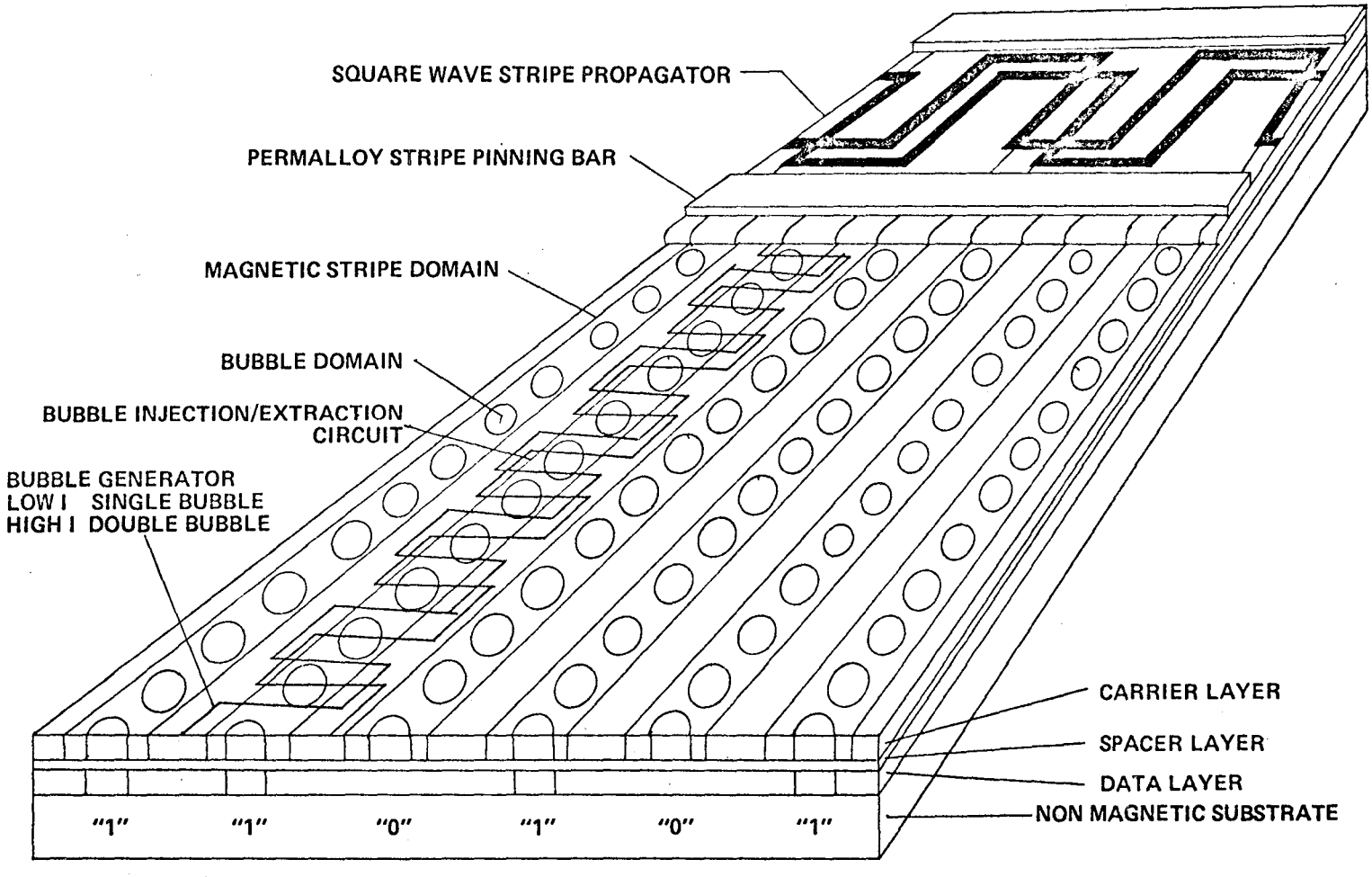

Figure 5.1 Schematic representation of a multilayer, self-structured memory.

5.2 Test Vehicle Evaluation

Four device designs were selected for the most recent test vehicle fabrication cycle. The devices are shown as:

Figure 5.2: Two layer, two phase square wave,
Figure 5.3: Permalloy assisted Philips' type square wave with side entry bubble generation,
Figure 5.4: Philips' square wave with series double bubble nucleation, and
Figure 5.5: Modified Philips' design with series single bubble nucleation.

These device designs were selected to allow at least one or more variations of each of the basic functions, including stripe nucleation, stripe end pinning, stripe transfer, stripe propagation, single and double bubble generation, bubble side entry, and bubble row transfer. Each of these functions will be discussed individually below.

Stripe domain nucleation has been demonstrated by two different methods: current pulses through an elongated hairpin loop and a single conductor stripline. In both cases a 500 μm stripe is produced pinned at both ends under the magnetic bars. The current required varies from ~100 to 600 mA x 0.2 μs, which is a function of garnet $4\pi M$ and the presence or absence of a "seed" domain beneath the magnetic pinning bar. Once generated and pinned, the stripe domains are stable in bias fields in excess of the bubble collapse field by up to 25% or more.

Pinned stripe domains can be transferred between the conductors in the generate region by 20 to 50 mA pulses 0.5 to 1.0 μs long.

A major obstacle was encountered in most Philips' type devices when it was attempted to hand off the stripes from the generate region to the propagation lines of the main storage area. The stripe domains were acted on by a variety of gradient producing conditions which attempted to push, pull, or flip the domains into the control of the propagation circuitry. However, the stripe domains consistently were severed at one or both ends, causing the stripe domains to collapse to bubbles when performed at bias fields greater than H_{RO}.

The reason for this behavior became readily apparent after a scanning Electron Microscope (SEM) study of two of the devices. Due to the nature of the ion milling process used [13] for conductor line etching, a trench was ion milled into the garnet film surface near the edge of many of the AlCu conductors. As shown in Figure 5.6, the conductor edges susceptible to trenching effects are those which are exposed to an open area of more than 2μm from the stripline edge. Stripline gaps of 2μm

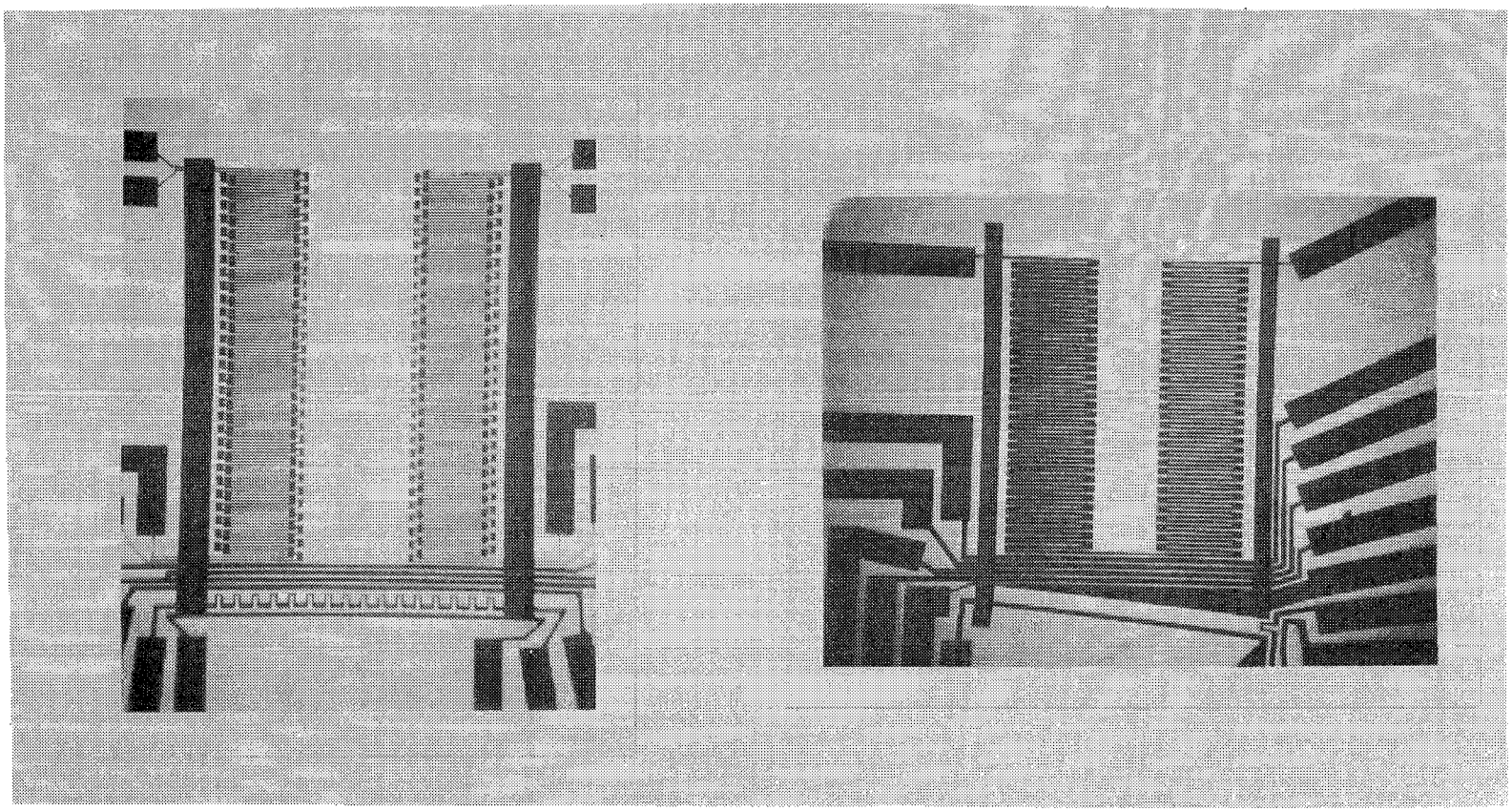

Figure 5.2 Two Layer, Two-Phase Square Wave Series Single Bubble Nucleation.

Figure 5.3 Philips' Type Square Wave with Side Entry Bubble Row Generation.

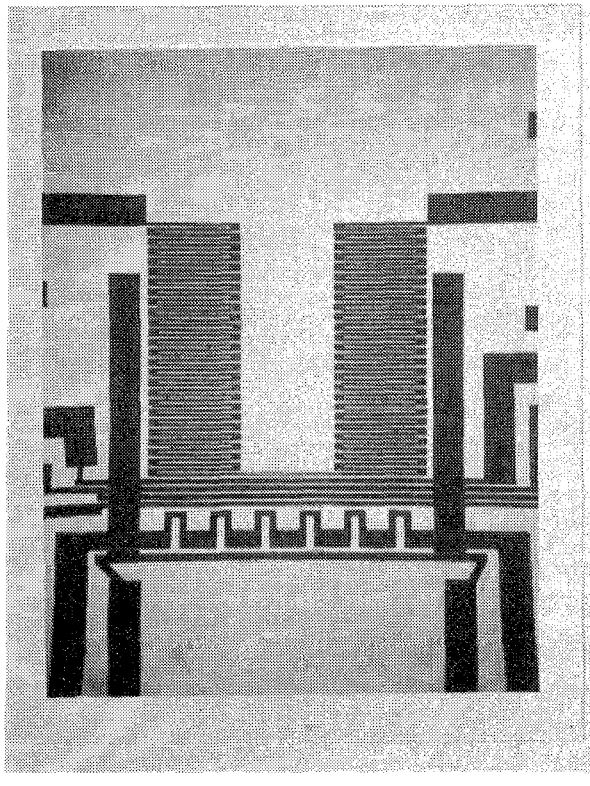

Figure 5.4 Philips' Type Square Wave with Double Bubble Nucleator.

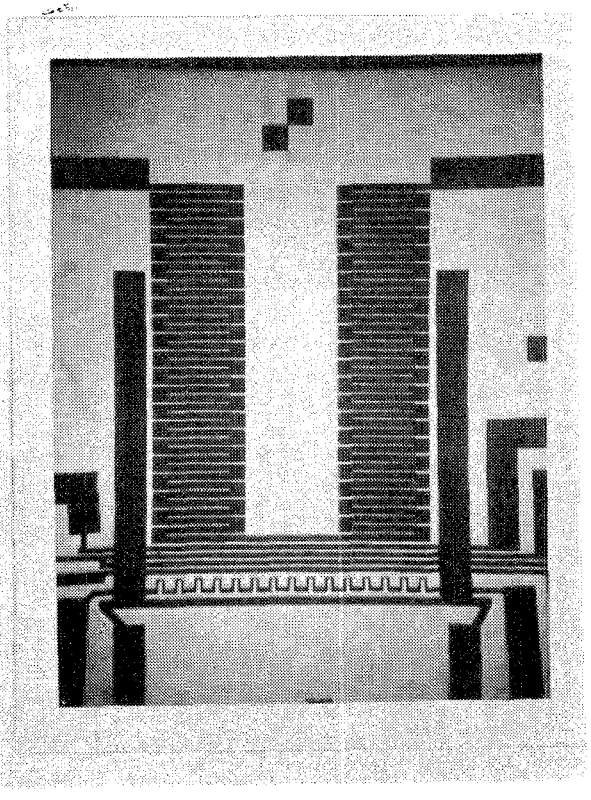

Figure 5.5 Modified Philips'Square Wave with Single Bubble Nucleator.

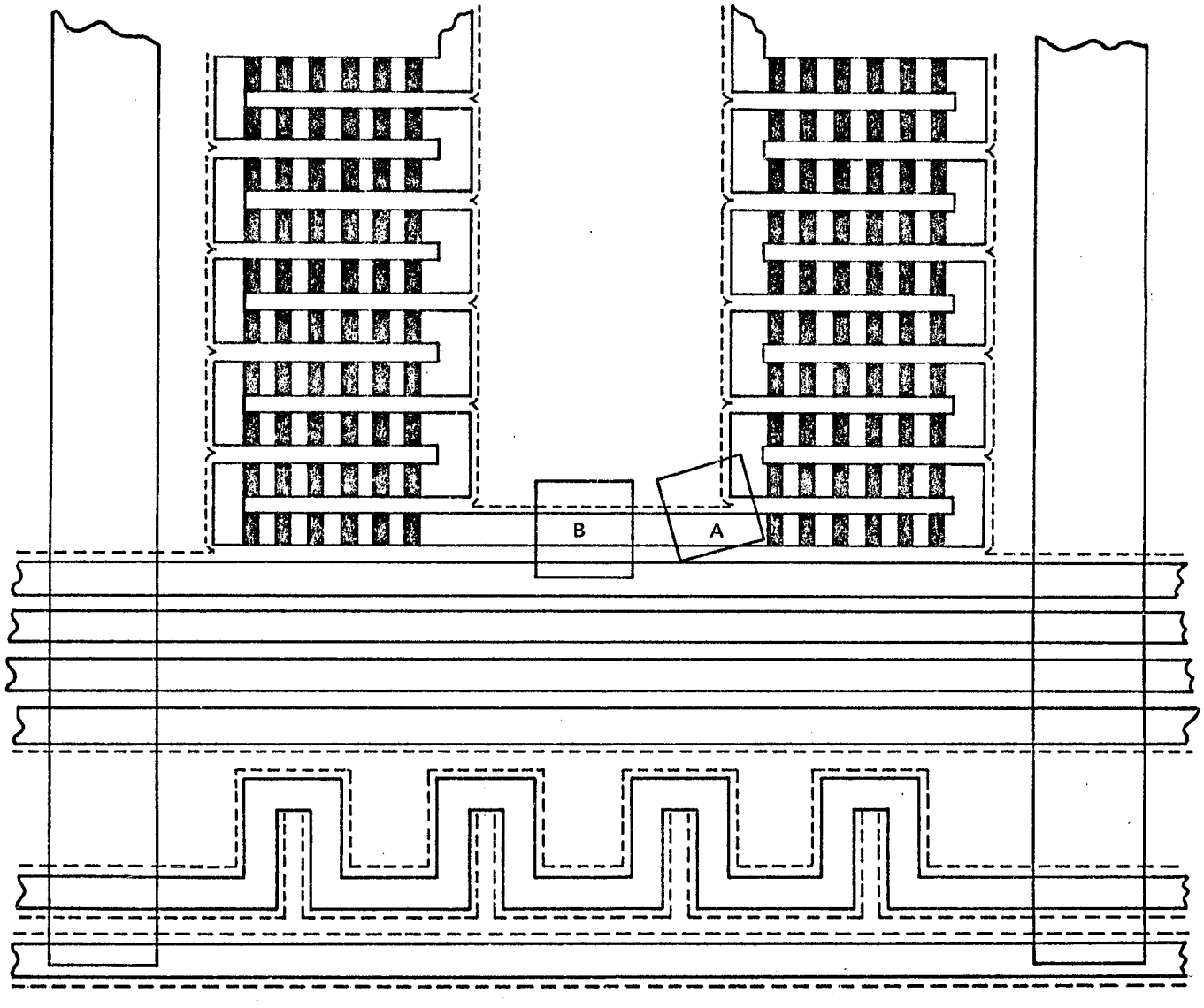

Fig. 5.6 The dashed line indicates device areas affected by the ion mill trenching effect. Blocks A and B refer to fig. 5.7a and 5.7b, respectively.

or less experience a less severe trenching effect which does not penetrate the 4500 Å SiO_2 spacer layer between the AlCu and garnet films. In general, the spacing between adjacent lines is 2μm, except between the lower three lines illustrated in the device of Figure 5.6, thus explaining the trench pattern shown.

In Figure 5.7, SEM photographs show a device which has been etched in a buffered HF solution to remove the SiO_2 spacer layer. Note that the AlCu lines have also been attacked and significantly reduced in width. Figures 5.7A and 5.7B represent areas of Figure 5.3 labeled A and B, respectively. The trenches described earlier are clearly evident. One should recall at this point that ion milled channels and mesas are often used to provide energy barriers for the confinement of magnetic garnet domains.[14] In this case, trenches of 2000 to 5000 Å depth are interferring with the movement of stripe and bubble domains within and out of the generate-transfer region.

Devices of the two layer two phase square wave variety did not suffer from any of the trenching effects observed in the Philips' variety. However, as shown in the SEM photo of figure 5.8, the SiO_2 step coverage over the AlCu conductors was incomplete due to processing steps which followed that SiO_2 deposition. As a result, magnetic pinning bars provided a continuous shorting bar for the entire length of the device, effectively disabling all current accessed functions.

In spite of these difficulties it was still possible to introduce a limited number of fully pinned stripe domains into the propagate regions of a number of the Philips' type devices. Bi-directional propagation of the stripe domains was demonstrated using 12 to 15 mA x 0.5 μs pulses and a DC in-plane field of $\pm$ 5 to $\pm$20 Oe. The direction of the in-plane field controls the direction of propagation as explained in detail in Section 4.3.3. A 1 MHz rf tickle field was used in all cases to reduce the effects of coercivity, as described in Section 3.4.6.

Rows of single bubbles were easily generated with multiple pulses in the series hairpin loop conductor and subsequently transferred to within one line of the propagation region.

At this point, the ion milled trenches presented at least as great a barrier to the bubbles as to the stripes. It was, therefore, not possible to enter a bubble row into the propagation region to produce the desired "half-lattice" carrier array. However, both half and full lattice arrays were created with another circuit, as shown in figure 5.9.

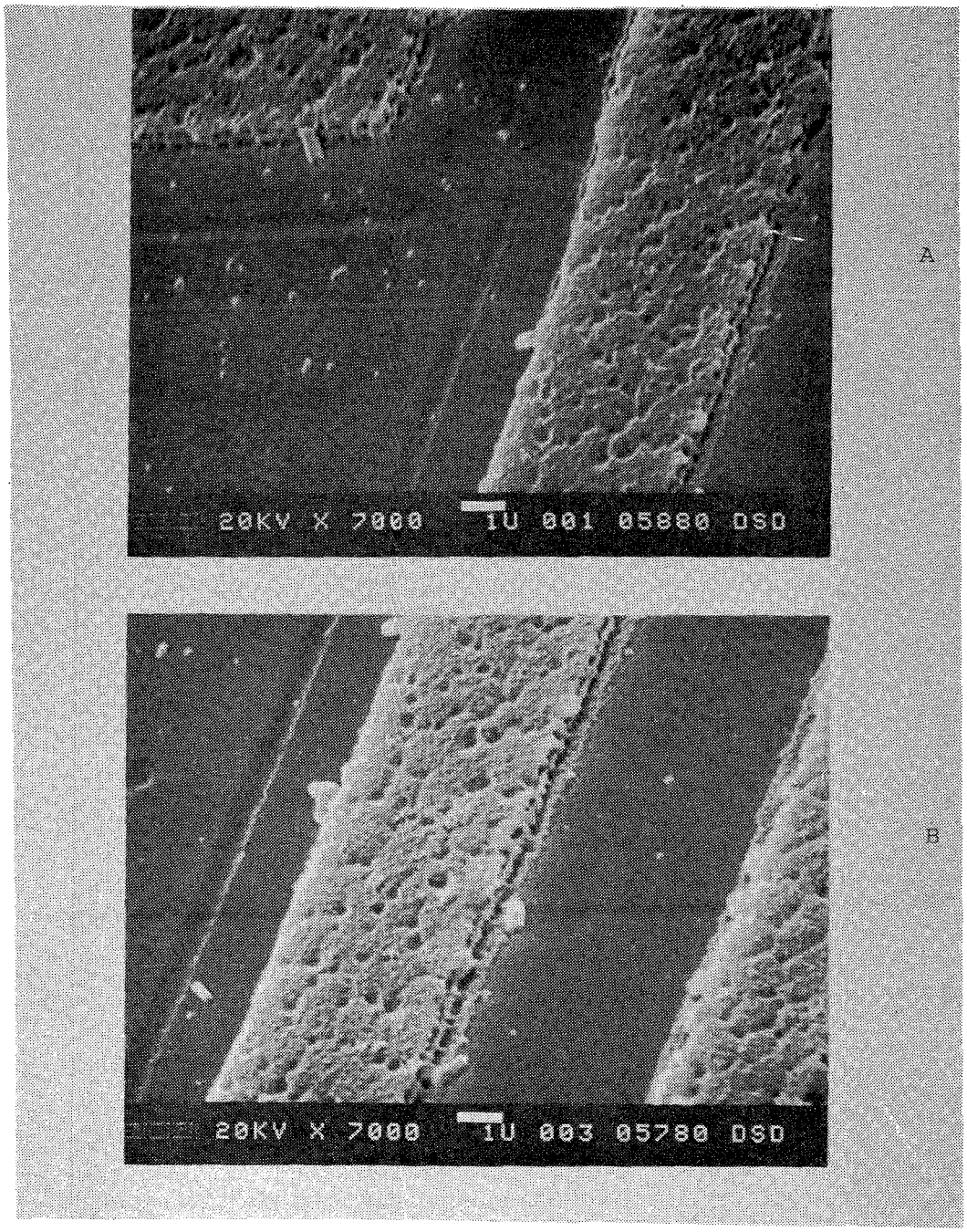

Figure 5.7 SEM Photos of Garnet Surface After HF Removal of SiO_2 Layers (AlCu lines were also strongly etched). Note Penetration of Ion Milled Trench Into the Garnet Surface of this Philips' Type Device.

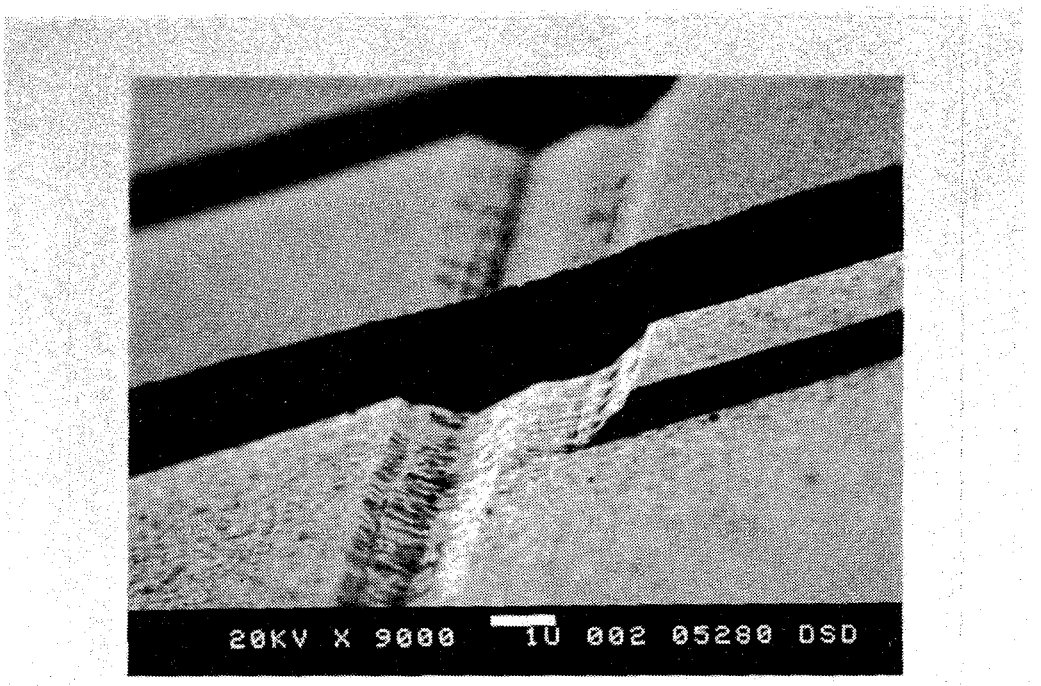

Figure 5.8 SEM photo of a Two-Layer Square Wave Device Showing NiFe Pinning Bar Shorting Between Two AlCu Lines. The SiO_2 to AlCu Interfaces are Clearly Evident. The Knife Edge on the NiFe bar is also a Result of the 10^{o} Ion Milling Angle.

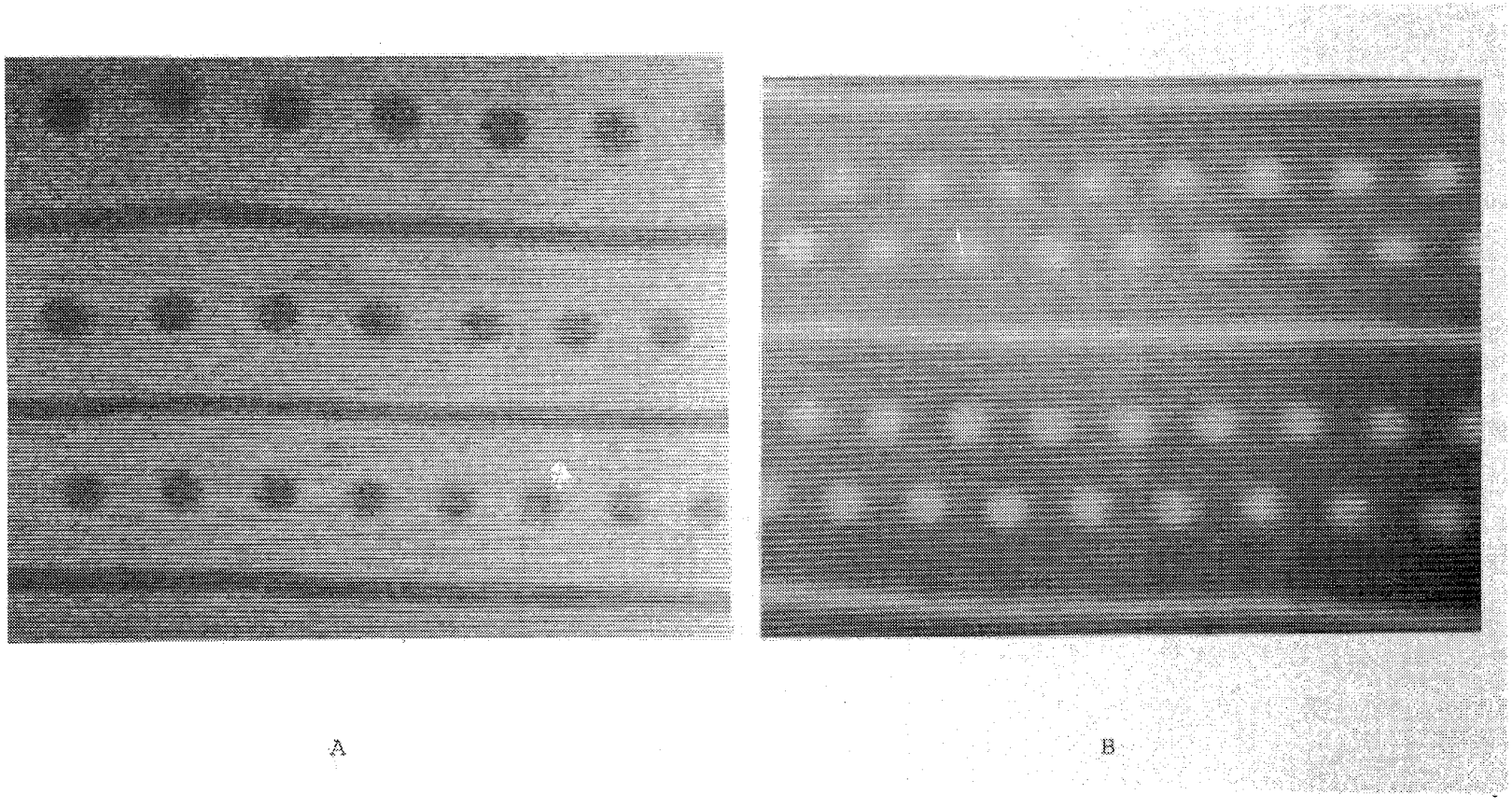

Figure 5.9 Photographs from a Television Monitor of Stripes and Bubbles in (A) "half-lattice" and (B) "full-lattice" Configurations.

Bubble row nucleation using the side entry technique of figure 5.3 has been judged unsuitable for use on present devices. The bias field gradient required to move bubbles along the line cannot be produced within the margins available for stable bubbles on the low $4\pi M$ garnets presently being used. As the project progresses to smaller bubble, higher $4\pi M$ materials, the bias margins will increase to a point where this design may once again be considered.

Double bubbles have been created using a scaled variation of the standard hairpin single bubble nucleator. The currents required are undesirably high. Alternative methods of double bubble generation, such as stripe cutting with garnet property variations, will be investigated.

5.3 Test Vehicle Summary

All functions necessary to develop a multilayer self-structured bubble memory device have been demonstrated. Specifically, these functions include:

- stripe domain end pinning,
- current accessed propagation of stripe and bubble domains,
- generation of arrays of co-existing stripe and bubble domains in one garnet layer,
- different values of the strip-out field for single and double bubbles, indicating adequate margins for data detection, and
- generation of single and double bubbles.

All of these functions have not been demonstrated on a single device, but have shown operational behavior in individual experiments.

6. Memory Element Circuits

6.1 Introduction

A second generation set of test vehicles was designed and fabricated to evaluate all the component functions necessary to implement a self-structured bubble memory. These components included bubble domain generation, stripe domain generation, data bubble input, stripe domain transfer, bubble detection, stripe propagation, and interlaced stripes and bubbles in the memory storage area. The test vehicle circuit is illustrated in Figure 6.1. All bubble and stripe control is accomplished with current accessed techniques.

Two types of multi-layer magnetic garnets were employed for the fabrication of the test vehicles. Double layer magnetic garnet layers, separated by a GGG layer, were grown on a GGG substrate by the Sperry Research Center in Sudbury, Mass. This type of garnet structure has the magnetic layers coupled by magnetostatic interaction. Double layer magnetic garnets with no separating layer were grown on a GGG substrate by the Physical Sciences Dept. of Sperry Univac in St. Paul, Minn. This type of garnet structure has the magnetic layers coupled by exchange interaction.

6.2 Memory Element Circuit Fabrication

Processing of the test vehicle circuits comprised 57 separate steps to realize a completed chip, and consisted of the following main fabrication steps. A spacer layer of SiO was vacuum deposited on the cleaned garnet, and followed by a vacuum depostied layer of 95% AlCu. Photolithographic processes defined the propagation circuit patterns. A layer of sputtered quartz was deposited for insulation purposes, followed by a vacuum deposited layer of NiFe. Photolithograhic steps then generated the NiFe propagation elements and the magnetoresistive sensors. Another layer of sputtered quartz was deposited, and vias were etched in this layer to expose the leads to the magnetoresistive sensors. A final layer of AlCu was deposited, and photolithographic processing defined the remaining control lines and sensor leads. Additional vias were then etched in the quartz layers to expose all the bonding pads.

Typical values of the layer thicknesses and deposition temperatures are: SiO, 4KÅ, 125°C; AlCu, 4 to 5 KÅ, 25 to 125°C; SiO_2, 5KÅ; NiFe, 4KÅ, 400°C. The completed chips were mounted on printed circuit cards, and electrical connections to their 40 pads were made with ultrasonic bonding with 0.001" aluminum wire.

6.3 Bubble Generation

Generation of single layer bubble domains in the exchange coupled garnet was easily accomplished with the hairpin generator located at the end of the data input track. A current pulse of 80 to 90 ma,

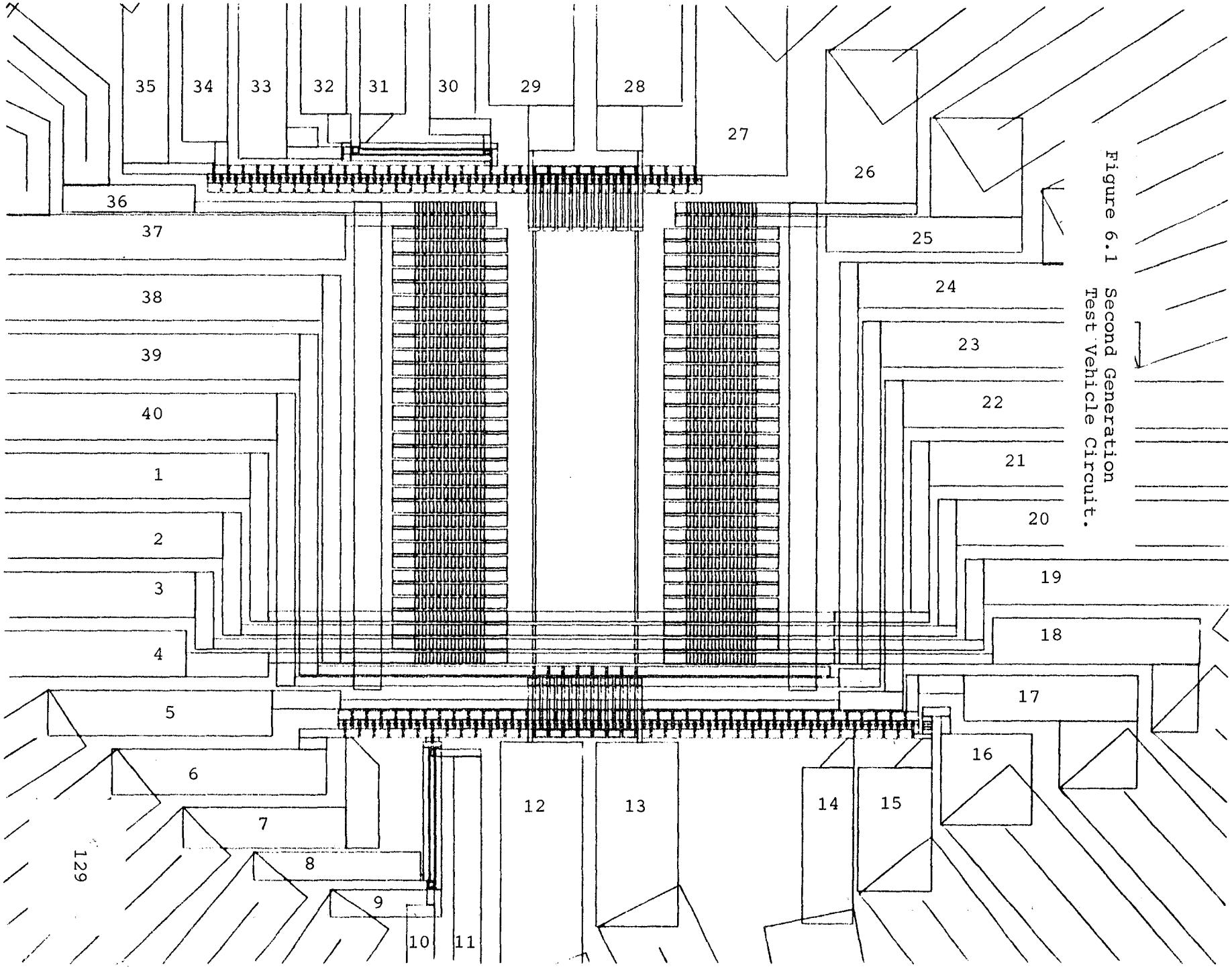

Figure 6.1 Second Generation Test Vehicle Circuit.

0.5 μs long, would generate a bubble over a bias field range of 75 to 85 oe. Two of the three legs of the hairpin generator have NiFe bars located above them, and the bubbles are observed at the end of one of these bars after the generate pulse is applied. The location of the bubble depends on the direction of the applied in-plane field, which establishes the magnetic polarity of the NiFe bars. The in-plane field was employed to define the direction of bubble propagation along the data input track.

Bubbles were propagated along the entire length of the data input track with alternating current pulses of ±15 ma, 2 μs long, with an in-plane field of 5 oe. Reversing the direction of the in-plane field caused a reversal in the direction of bubble propagation, which is opposite to that defined by the applied field. Both fully and partially populated patterns of bubbles were propagated along the track.

Generation of double bubbles was not attempted with this circuit. Due to the anticipated large current requirement, it was decided to delay this test because of the possibility of fusing the circuit, which would destroy a portion of the test vehicle.

6.4 Bubble Transfer

Transfer of bubbles from the data input track to a location between the stripe domain generator and storage area is required for this self-structured memory design. Bubbles were transferred in the exchange coupled garnet from the data input track to the bottom of the NiFe features located on the stripe generation circuit with a 42 ma, 2 μs, pulse in line 12-13, at a bias field value of 75 oe. Two in-plane fields were applied; a 10 oe field along the input track and an 8 oe field orthogonal to this field. The first field defines the direction of bubble propagation along the input track, and the second field establishes an attractive pole on the NiFe features located on the stripe domain generator circuit. A small current pulse, 15 ma, 2 μs, in the stripe generator (lines 39-40) moved the bubbles to the NiFe features on the other leg of the stripe generator, translating toward the storage area. A 15 ma pulse of the opposite polarity applied to the stripe generator circuit (39-40) caused the bubble to move close to the edge of line 4, thereby releasing from the NiFe features. This represents an important experimental demonstration, where a bubble domain has been removed from a magnetic feature to a location with no magnetic feature.

Current pulses of 15 to 20 ma of the proper polarity applied to lines 1,2,3, and 4 propagated bubble domains from the edge of line 4 to the center of line 1. The pulse pattern is illustrated in Fig. 6.2. Since there are no defined propagation tracks for bubbles to move from line 4 to line 1, some of the bubbles would move to the confinement rail NiFe features located on lines 1 through 4, which is undesirable.

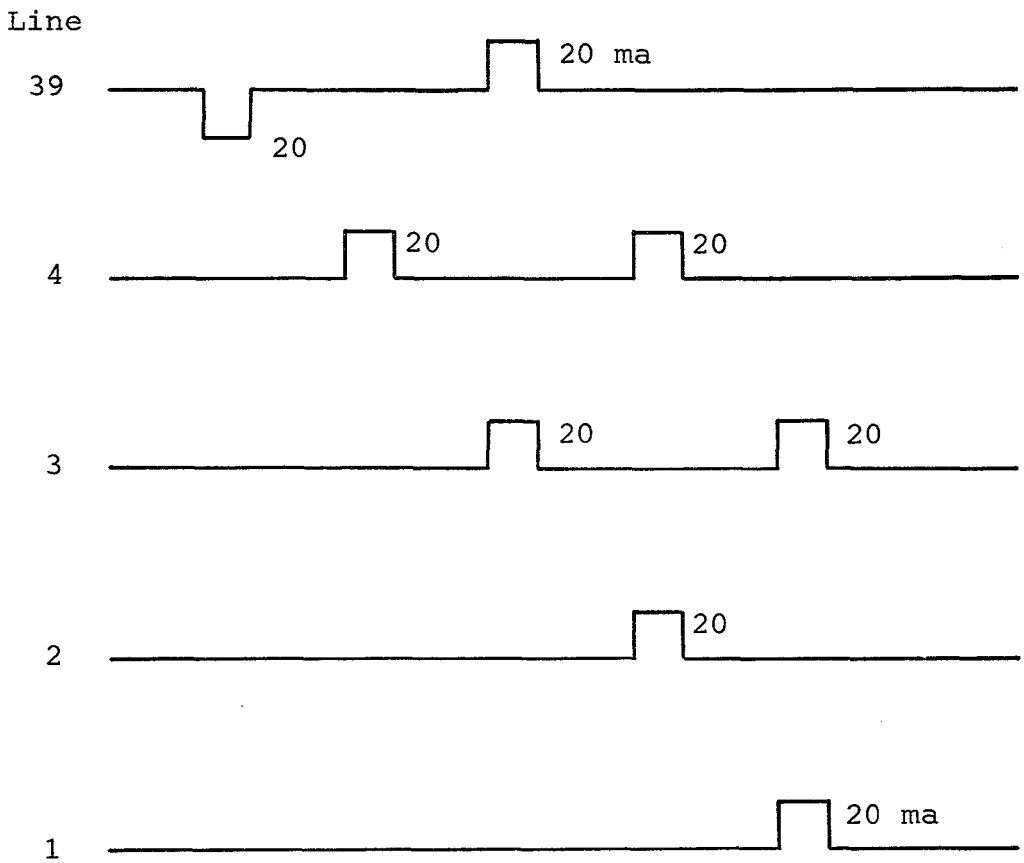

Figure 6.2 Current Pulse Sequence for Bubble Propagation from the Stripe Generator to the Edge of the Storage Area.

This behavior will not occur with a fully populated row of bubbles, since the design assumes that expendable bubbles on each end of the row will attach to the NiFe rails, thereby establishing a barrier for the bubbles between the rails. The fully populated row would contain carrier bubbles, with data bubbles located in the second garnet layer.

6.5 Stripe Domain Generation and Transfer

Generation of long stripe domains in the exchange coupled garnet was accomplished with the application of a 170 ma, 0.5 μsec pulse to the stripe generator circuit, lines 39-40, over a bias field range from 70 to 88 oe. The stripe was located along one of the two long inner edges of the hairpin generator circuit, depending on the direction of an applied in-plane field acting on the NiFe features located on the generator legs. Two large NiFe stripe pinning bars are located outside the serpentine stripe propagation circuits, and the newly formed stripe was attached to these bars. A normal bias field of 15 oe above the bubble collapse threshold was required to release the stripe from the pinning bars.

Successful propagation of long stripe domains from the generator to the edge of the storage area was accomplished with the current pulse pattern illustrated in Fig. 6.3. The current pulse in line 23 flows through one leg of the stripe generator circuit, and moves the stripe from the inside to the outside of the generator. This pulse, in combination with the wide pulse in line 4 applied at the same time, causes the stripe to release from the NiFe features on the generator and move to the nearby edge of line 4. Applying the pulse pattern shown in Fig. 6.3 to lines 23, 4, 3, 2, and 1 moved the central portion of the long stripe to the edge of the storage area. Current pulses in lines 38 and 24 were employed to move the ends of the long stripe domain.

The NiFe features located on top of the serpentine long-stripe propagation circuits are in their proper position with respect to the garnet. Lines 1 through 4 cross these propagation circuits, thereby placing the NiFe features between these lines and the garnet. This last arrangement generates normal magnetic fields at the edges of the conductor and the ends of the magnetic features which are in opposition. Therefore, it was not possible to propagate the entire stripe domain with pulses in line 1 through 4 (to propagate the central portion) coincident with the pulses in lines 38 and 24 (to propagate the stripe ends). Successful propagation of long stripe domains was accomplished by delaying the pulses in lines 38 and 24 to move the stripe ends, as illustrated in Fig. 6.3. This procedure eliminated the interference of the two conductors surrounding the NiFe features.

When a stripe domain was generated, it extended to the NiFe pinning bars located near each end of the generator circuit. It was not possible to move the end of the stripe along these pinning bars

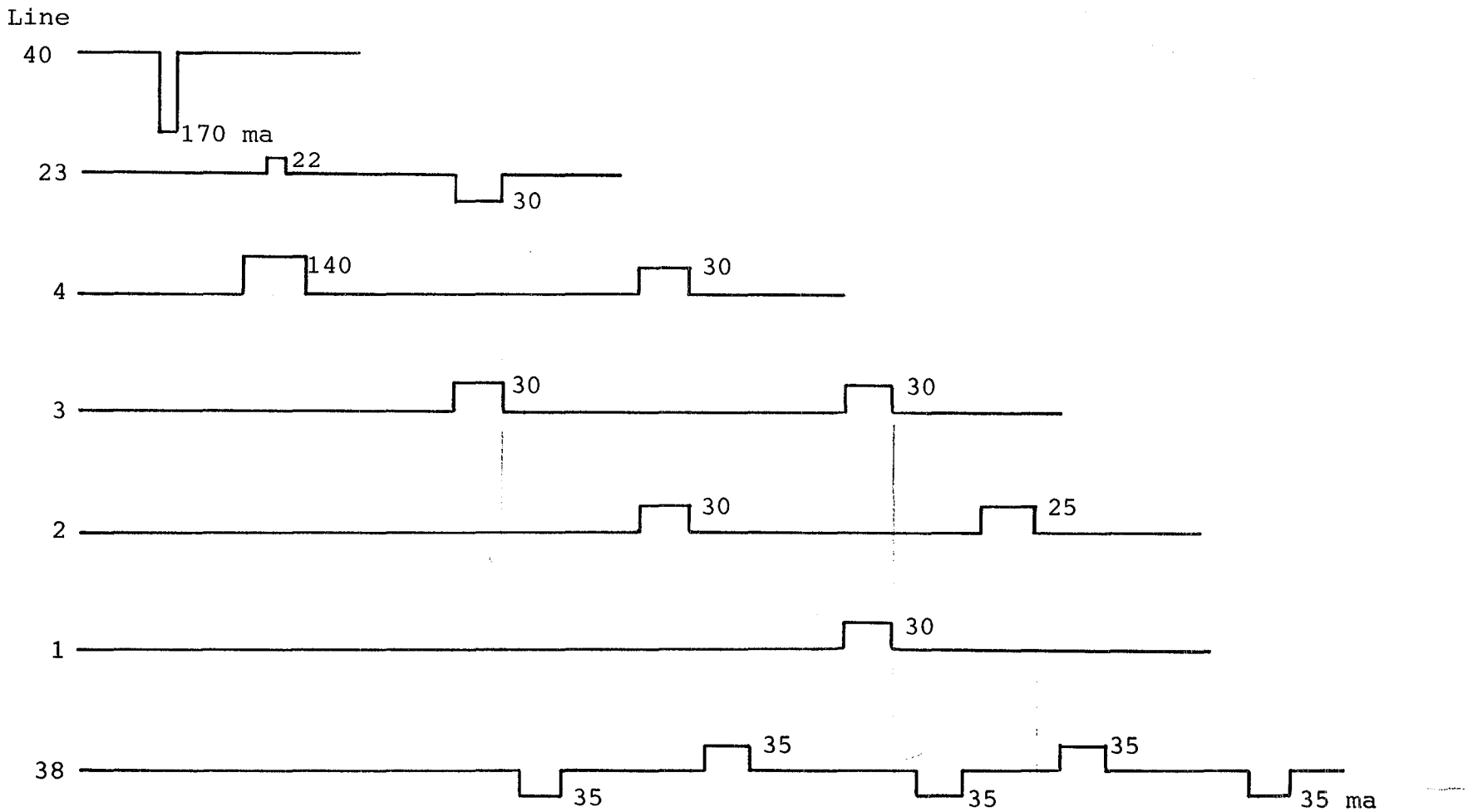

Figure 6.3 Current Pulse Sequence for Stripe Domain Transfer from the Stripe Generator to the Edge of the Storage Area in the Exchange Coupled Garnet Circuit.

during the stripe movement described above. The reason for this behavior is the familiar "conductor crossing" problem, where the NiFe bar is crossing the tapered generator conductor. The presence of a bias field generates magnetic poles at this transition region, and holds the stripe at this location. This situtation will be avoided in future designs.

After propagation of a long stripe to the edge of the storage area, it was possible to move the stripe ends further along the serpentine circuits, but the central portion remained behind. It was not possible to move the central region beyond the last edge of conductor 1. Apparently there are large stresses along this conductor that traps the stripe, and being able to only push the stripe from one side (conductor 2), resulted in the stripe not releasing into the storage area. The addition of a ±6 oe, 1 MHz modulation to the normal bias field did not help in moving the stripe past the last conductor. Replacing SiO and SiO_2 with polyimide for insulating and stress relief layers should improve the domain behavior near conductor edges.

Similar tests were conducted with the magnetostatic coupled garnet circuit, and the pulse sequence to generate and translate a stripe domain to the storage area is shown in Fig. 6.4. The pulse pattern in very similar to that employed with the circuit on the exchange coupled garnet, but with two notable differences. The pulse amplitudes for generation and transfer are considerably larger, and the pulse durations are increased from 2 μs to 5 μs. Again, the stripe could be transferred to the edge of the storage area, but it would not release from the edge of the last line.

6.6 Stripe Domain Propagation

Serpentine conductors, with NiFe features, located on both sides of the storage area are designed to propagate long stripe domains by translating both ends of the stripe. Since it was not possible to move a stripe from the generator into the storage area, stripe domains were established in the storage area by saturating the garnet with a normal bias field, and then reducing the field, with a transverse in-plane field applied to define the stripe direction.

Propagation of the stripe domain ends in the exchange coupled garnet along the serpentine conductors proceeded nicely with bipolar current pulses of 35 ma, 2 μs. However, the central portion of the stripe did not follow the motion of the ends, and moved approximately one-fourth as far, causing the stripe to be severely bowed after several propagate pulses. The application of a ±6 oe, 1 MHz bias modulation field improved the situation somewhat, but only to where the central portion moved approximately one-third that of the ends. Increasing the magnitude of the DC bias field caused the bowed stripes to straighten somewhat, but they collapsed easily when their ends were translated.

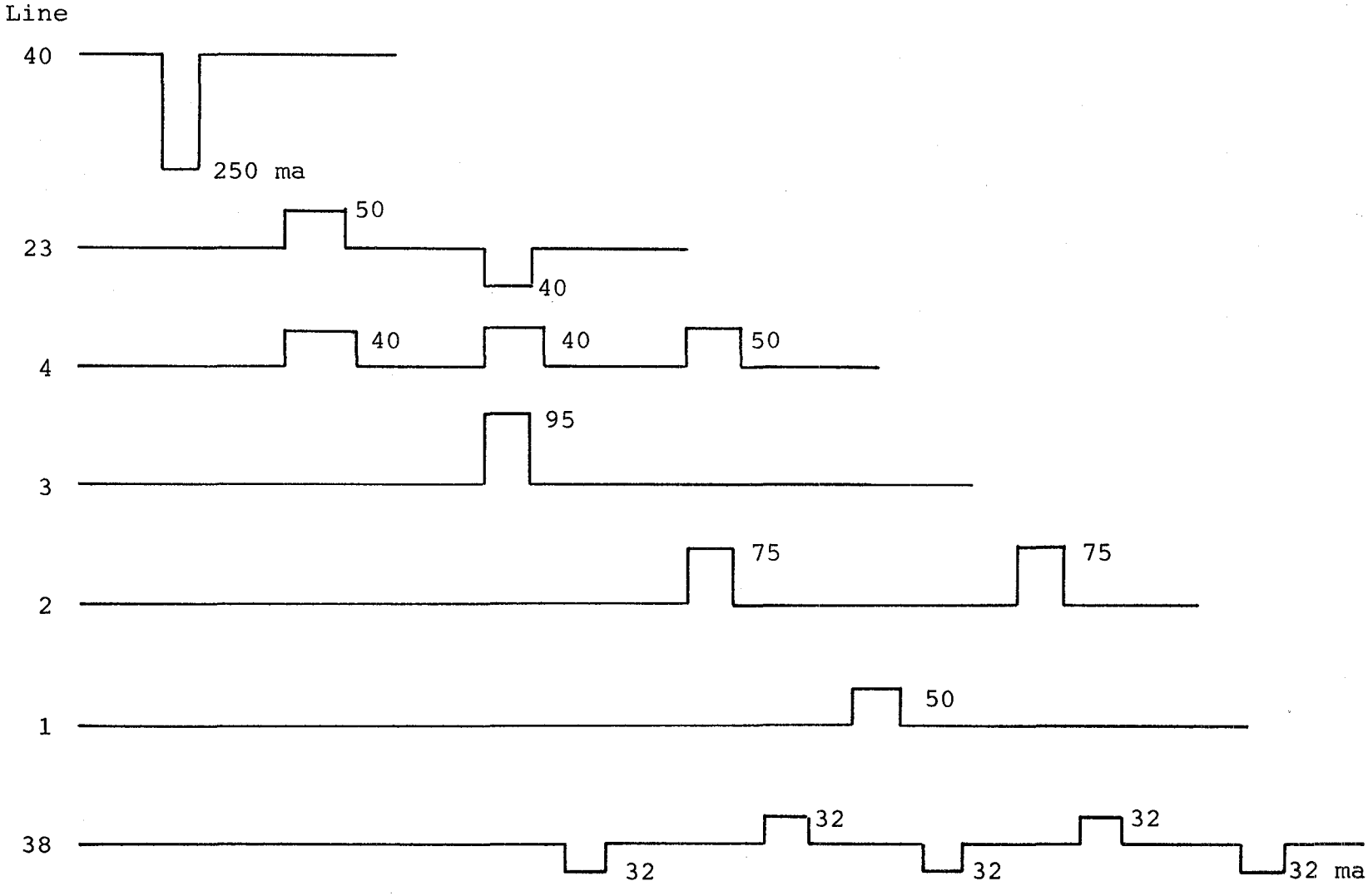

Figure 6.4 Current Pulse Sequence for Stripe Domain Transfer from the Stripe Generator to the Edge of the Storage Area in the Magnetostatic Coupled Garnet Circuit.

Propagation of long stripe domains was more successful with the magnetostatic coupled garnet. Applying 2 μs current pulses to the serpentine circuits did not cause reliable propagation of the stripe ends. Increasing the pulse width to 7 μs promoted good propagation. Apparently, the domain mobility of this garnet is less than that of the exchange coupled garnet. Without the 1 MHz bias modulation field, central stripe movement severely lagged behind the stripe ends. However, with a ±6 oe RF field, the central portion propagated quite nicely, and trailed the ends by approximately one-half period of the serpentine circuit. Forward and reverse propagation was observed, corresponding to a reversal of the direction of the applied in-plane field of 10 oe magnitude. The central portion of the stripe generally did not move at the same time as the stripe ends, often moving slowly for an additional 1/2 to 1 second after the application of the propagation pulses. The action of the RF field was responsible for this delayed behavior. Increasing the magnitude of the RF field decreased this response time, but did not completely eliminate it. A larger bias field caused the stripes to be more nearly straight, but the stripes sometimes collapsed when propagating under these conditions.

The improved propagation of long stripe domains in the magnetostatic coupled garnet with RF bias field modulation indicates that the coercive force of this garnet is lower than that of the exchange coupled garnet. However, the required longer duration of the current pulses indicates that the mobility or limiting velocity of the domains is lower in the magnetostatic coupled garnet.

6.7 Domain Detection

A brief experiment was performed to electronically detect domains entering the region of the magnetoresistive sensor. A bridge circuit, with the magnetoresistive element in one leg of the bridge, and with external resistors, was employed for detection as shown in Fig. 6.5. A signal level change of 1 mv was observed when a domain ran out along or collapsed from the NiFe element, with 10 ma of current in the NiFe element. The domains detected were double stripes, since the run-out threshold of stripes in the outer garnet layer is less than that for a double stripe.

The NiFe element of the detector is the same thickness as the domain propagation elements, (4 KÅ), which is much too thick for an optimum signal. Reducing the detector thickness by a factor of ten would increase the signal by a factor of ten, with the same detector current. Increasing the detector current from 10 ma to 50 ma would increase the signal by a factor of five. The signal was detected using an external bridge, which attenuates the signal by a factor of two. Incorporating a dummy detector on the chip with differential sensing would recover this factor of two.

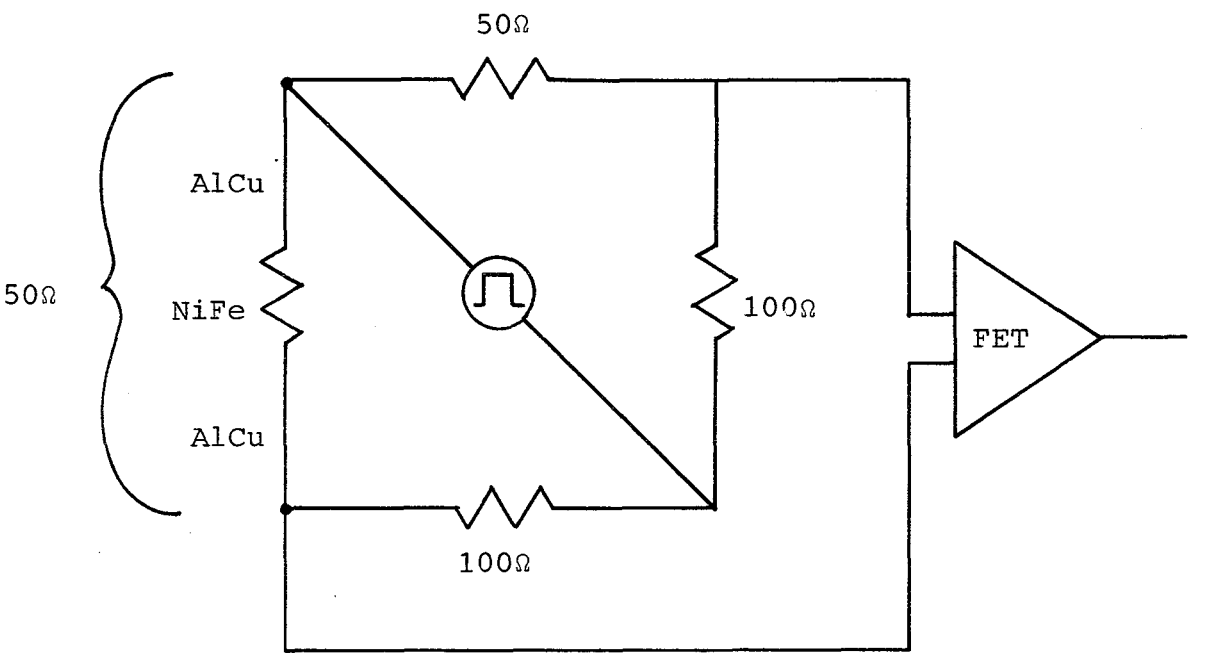

Figure 6.5 Domain Detection Circuit, with One Magneto-resistive Element and Three External Resistors.

The NiFe element has a length to width ratio of approximately 26:1, a thickness of 4000 Å, and a resistively near 13 micro ohm cm, yielding a resistance of 8.5 ohms. The total detector resistance of 50 ohms indicates that the AlCu conductors on the chip account for approximately 40 ohms. The change in voltage drop ΔE across the NiFe element due to a change in its resistance is related to the element resistance R, the percentage change in resistance p, and the current flowing in the element I, as expressed in eq. 6.1.

$$\Delta E = pIR \tag{6.1}$$

Using R = 8.5 ohms, I = 10 ma in the NiFe element, and p ≈ 2%, eq. 6.1 yields ΔE = 1.7 mv. The detected signal should be one-half of this, 0.85 mv, since the bridge attenuates the signal by a factor of two. This value is reasonably close to the 1 mv signal change observed experimentally.

6.8 Memory Element Circuit Summary

In addition to the memory functions demonstrated by the test vehicles and listed in Section 5.3, the memory element circuits have demonstrated the following functions which are necessary to develop a multilayer self-structured bubble memory device:

- current accessed propagation of stripe domains,
- current accessed propagation of bubble domains,
- stripe domain end pinning,
- generation of long stripe domains with pinned ends,
- generation of bubble domains,
- bubble domain release from magnetic features,
- domain detection with magnetoresistive sensing, and
- self-structured design compatibility with magnetostatic and exchange coupled garnet layers.

7. Memory Configuration Recommendations

The next phase of this effort is to begin with the design of a self-structured current accessed bubble memory device of 10^7 bits on a 1.5 cm by 1.5 cm chip with shift rates greater than 1.5 X 10^6 bits per second. Next, the component set (i.e. stripe propagators, I/O bubble propagation, generators, detectors, etc.) is to be identified. This set is to be verified experimentally by fabricating various devices. The number and variety of device designs will be as large as the funding will allow.

There are two different designs that deserve consideration. One is a rectangular array design; the other is a concentric circular array design. These are presented below. The interior of each array has common features:

7.1 Common Features

The multilayer magnetic bubble structure is shown in Figure 6.1. The design of the propagation, or carrier, layer includes current accessed stripe domain propagation conductors, stripe domains, magnetic bars for stripe end pinning, carrier bubbles, stripe generators, double bubble generators, bubble extraction conductors, and bubble expanders and detector circuitry. The data layer includes only the data bubbles.

Data bubbles are located directly under the carrier bubbles, due to magnetostatic interaction, and follow the motion of the carrier bubbles during propagation. Binary data is coded by the presence and absence of data bubbles associated with each carrier bubble. Propagation of the stripe domains causes bubbles to also propagate in an orderly fashion.

The data layer is located below the carrier layer, which simplifies the fabrication of the device. An earlier design had the data layer on top, with this garnet layer smaller in area than the bottom carrier layer to accommodate stripe domain propagation circuitry for the carrier layer. The difference in the bubble nucleate field provides the basis to write data into the device. A low level current in a simple generator loop will nucleate a single bubble in the carrier layer, and a high level current will nucleate a double bubble -- one bubble in each layer. Detection is based on the difference in the run-out threshold. A carrier bubble is placed in the detector and is tested by a current pulse, which reduces the local normal field below the run-out threshold for a double bubble. A double bubble will strip out across the expander/detector, while a single bubble will not strip out and no signal will be detected.

Bubble and stripe domains can co-exist in the same garnet layer when biased above the run-out threshold, since the stripes are prevented from collapsing to bubble domains by the end pinning action of the magnetic bars illustrated in Figure 5.1. Carrier bubbles in this layer are located between pairs of stripe domains, and are evenly spaced due to mutual repulsion.

7.2 Rectangular Array

Figure 7.1 shows the chip design for rectangular arrays. This design meets the requirements of the T.D.R.S.S. for a current accessed 10^7 bit per 1.5 centimeter by 1.5 centimeter chip, with data rates of greater than 1.5×10^6 bits per second. The design presumes a bubble cell size of 6 micrometers by 3.2 micrometers, or 19.2 square micrometers.

Photographs of self-structured bubble lattices with larger bubbles extrapolated down indicate that the required bubble size is 1.6 micrometers. The chip is divided into 18 arrays, two of which are redundant. Each array contains 1,024 rows, of 512 bubbles each. The stripes of any array can be accessed by selecting the appropriate stripe propagate line. By selecting an appropriate data track, a row of bubbles from any array can be removed and sent along the track to the detector. Likewise, a row of bubbles can be inserted into the array. The data track originates at the bubble generator and branches; the bubbles follow the branch in which current flows.

One possible modification to the mentioned design is suggested by the fact that there is only one stripe propagate pulse in every 512 bubble track propagate pulses. The impedances of the two lines are approximately the same; consequently, the power dissipation in the stripe propagate lines is only 1/512 of that in the bubble track propagation lines in a serial mode. This suggests that a reduction in complexity and a large reduction in the number of pads for outside connections can be achieved by running the stripe propagate lines for all arrays in parallel.

There are two ways of entering data into a rectangular array: end entry and side entry. If data is entered at one end and extracted at the other, the result is a completely serial array, of little commercial interest. If data is entered from the side, as shown in figure 7.1, fast random access can be achieved. One can move the stripes forward or backward rapidly until the desired row of bubbles is at the input/output track. The bubbles can then be removed on that track and a new row of bubbles inserted. One problem with this scheme is that it is wasteful of space. If there is one input/output track per array as shown in figure 7.1, then bubbles can be stored in only half the array. The rest of the array

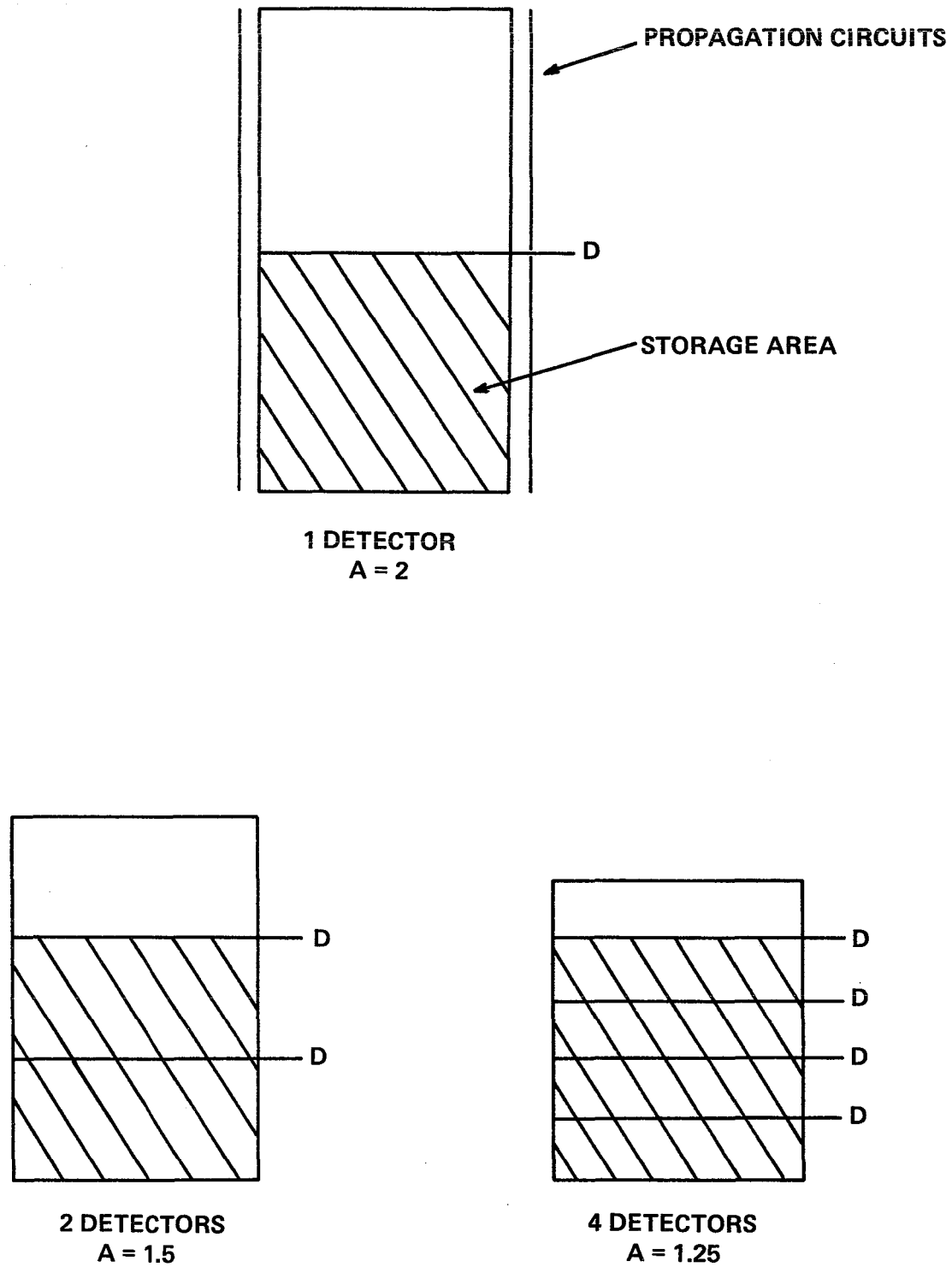

Figure 7.1 Total Area for a Memory Design vs. the Number of Detectors.

must remain ready to receive the bubbles when they are moved to place the desired bubble row at the input/output track. This is shown in figure 7.1. If two input/output tracks per array are used, the waste space is reduced to one third of the array, as shown in figure 7.1. If four input/output tracks are used, the waste space is 20% and so forth.

The rectangular array with side entry requires stripe propagators that can propagate the ends of stripes forward or backward. If the permalloy assisted serpentine propagators of figure 4.9 are used, a reversible in-plane field is required to determine the stripe motion. If the non-permalloy-assisted double serpentine conductors of figure 5.1 are used, the stripe motion reversal is accomplished by reversing the phase of the currents in the striplines.

7.3 Concentric Circular Array Design with Current Sheets

Late in the program we started testing current sheet bubble propagators for input/output tracks. Current sheets have the very desirable property of requiring a minimum feature size twice as large as a serpentine propagator. We found that these current sheets propagated stripe segments as well. That observation led to the chip and array design presented below. This configuration uses fewer lithographic features and larger features than the present test vehicles, has fewer outside connections, is more nearly impervious to etch out and shorts, has higher redundancy, requires no in-plane bias coils, no r.f. tickle field, has wider bias margins, is faster, and has less waste area on the chip.

7.3.1 Stripe Propagation

Figure 7.2 shows the basic arrangement for propagating stripes. The stripes can be put into such an array by applying a single large current pulse to one of the conductor layers. The stripes are propagated by first applying a positive current pulse, 1+, to the first layer, then a positive , 2+, to the second conductor layer, then a negative current pulse, 1-, to the first layer, and then a negative pulse, 2-, to the second layer. The current is parallel to the slots.

It is interesting to note that the minimum feature size is twice as large as in a serpentine stripe propagator such as found in our present test vehicles.

Note that each aperture pushes against the full length of each stripe. This is not wasteful. If we replaced a long aperture with two shorter ones we would have to supply a higher field gradient to the driven segments of the stripe to overcome the drag from the non-driven segments.

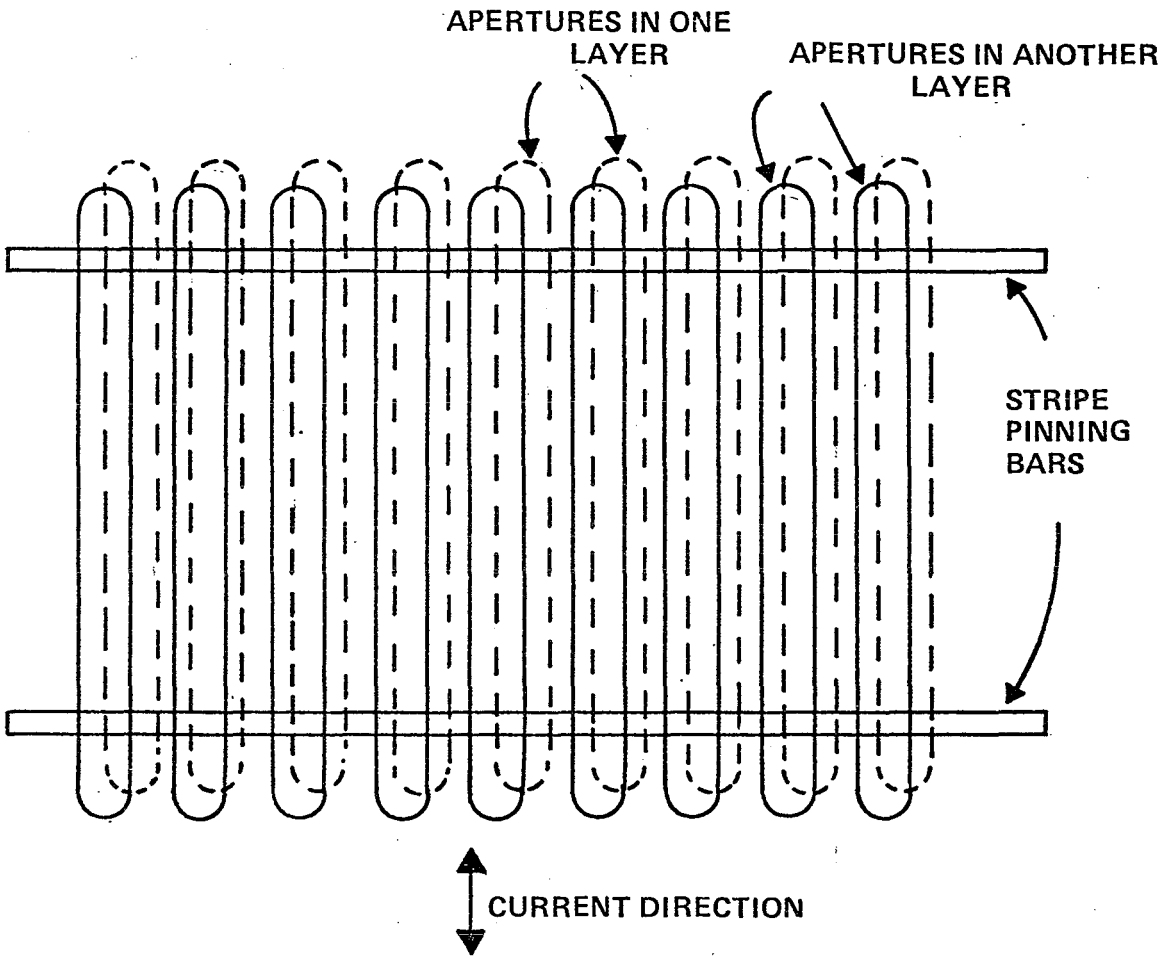

Figure 7.2 Current Sheet Stripe Domain Propagators.

7.3.2 Schematic Chip Organization

Figure 7.3 shows the schematic of a chip with concentric data tracks. The tracks are circular, and the chip is drawn square with rounded off corners.

The pads for wire bonding are mostly in the center. Pads 1 and 2 are to supply current to the two current sheets for stripe propagation as shown in fig. 1. Pads 3 and 4 are the outputs from the magnetoresistive sensor. Pads 8 and 9 supply current to the run-out strip that differentials between double and single bubbles. Pads 6 and 7 are for the input/output sheets that remove a row of bubbles from the lattice. That I/O track is shown at 4:00 o'clock in fig. 2. At the lower end of the I/O track is a bubble generator, labeled G. Although a single straight track is shown, a double track as a loop can offer advantages. The circular data tracks are labeled 10 through 18. Although only 8 of those are shown, as many of these as desired can be included.

One of the advantages of this design with radial current sheets is that no ground plane is required to reduce the normal field at the sheet edges parallel to the current flow. In this circular design there are no such edges.

7.3.3 Current Level

The current sheets measured in our lab require a current density of 1 ma per μm to propagate. This is a low current density, but for the current sheets shown in figure 7.3, the total pulse amplitude is inconveniently high. For a outer track diameter of 1.25 cm this would be 39 amps. Although we have experimentally demonstrated that such pulse amplitudes can be attained with transformers, it may be more convenient to divide the chip into sections and connect the sections in series as shown in figure 7.4. In both fig. 7.3 and 7.4 the current density is larger at the inner tracks than at the outer. While propagation margins are not sensitive to this, one may wish to have more uniform current. This can be achieved with the wire bonding scheme shown in figure 7.5. This reduces the required pulse amplitude to 3.25 amps. If a keeper is used, the pulse amplitude becomes a convenient 1.6 amps.

7.3.4 Power Level of Current Sheets

The current sheets are assumed to be 0.4μm thick and the deposited AlCu is assumed to have a resistivity of 5 μΩcm. The length of each segment shown in figure 7.4 is 0.23 cm and the average width 0.27 cm. The resistance of each segment is then 0.106Ω, the current per segment without keeper, 3.25 amps, the power per segment at 50% duty cycle is 0.56 watts, and the total power, 10 watts. If a keeper is used, the current is halved, and the total power is 2.5 watts.

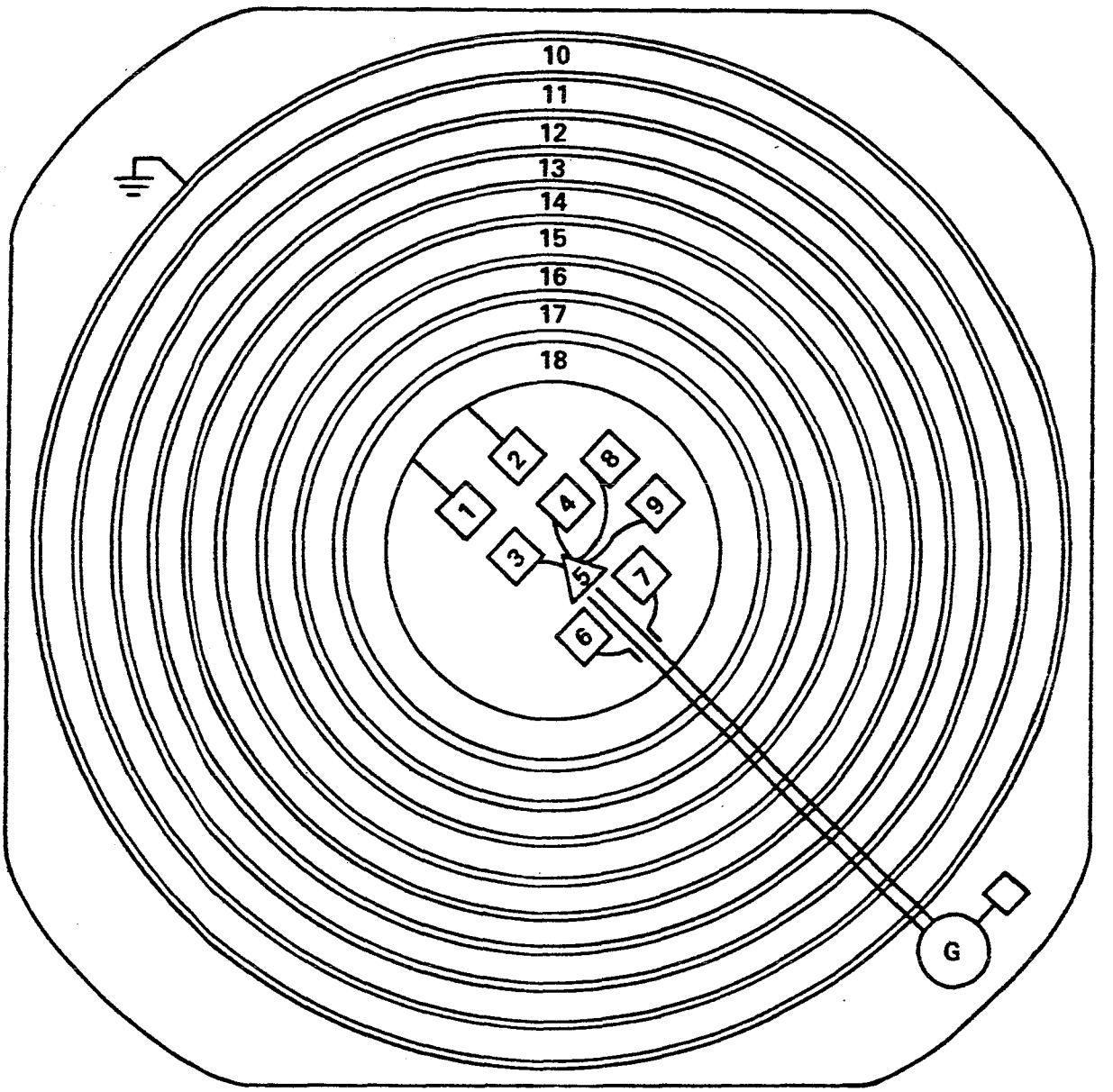

Figure 7.3 Schematic Representation of a Current Sheet Chip with Concentric Data Tracks.

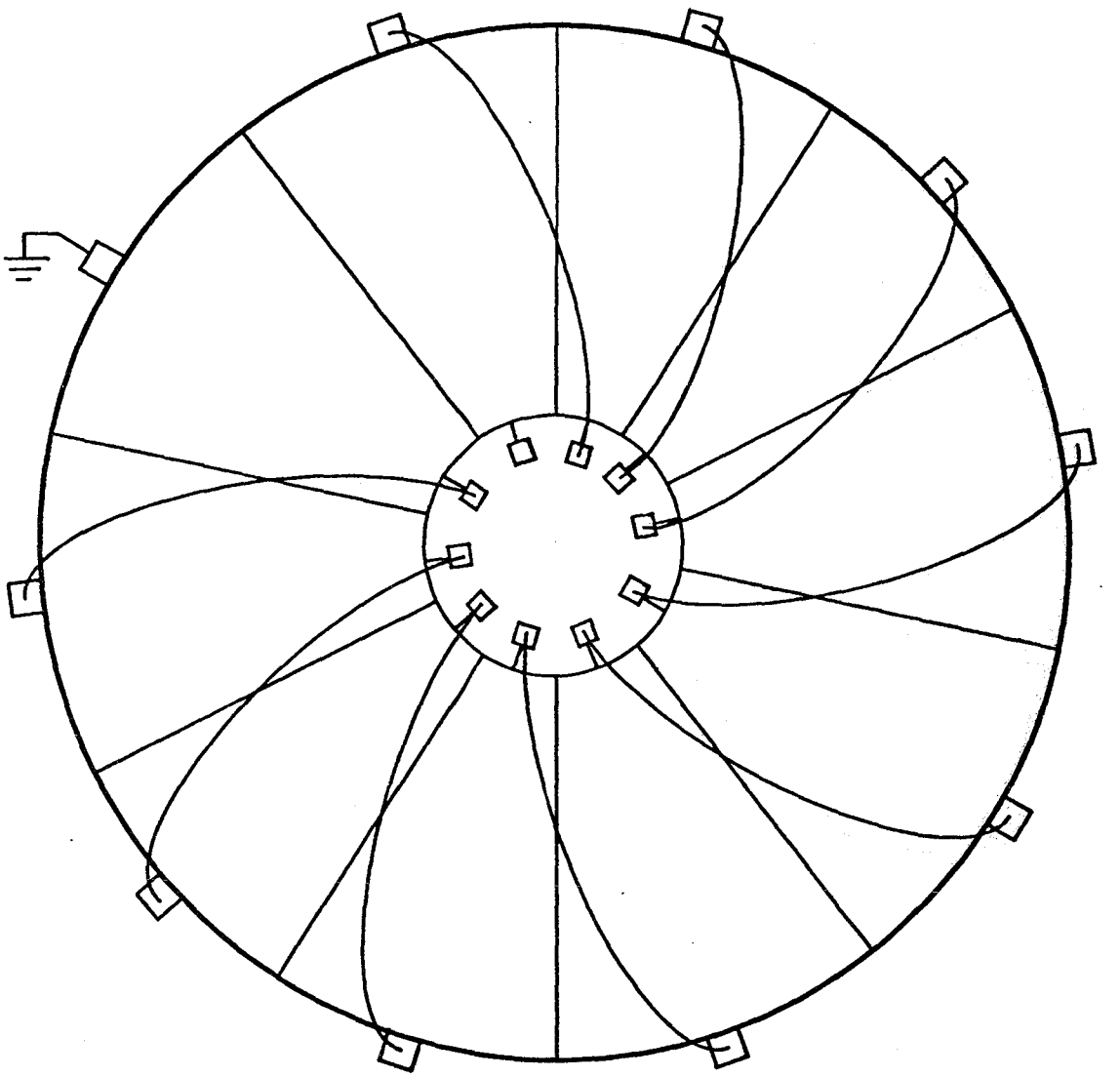

Figure 7.4 Current Sheet Chip Divided Into 10 Sections, Connected in Series by Wire Bonding.

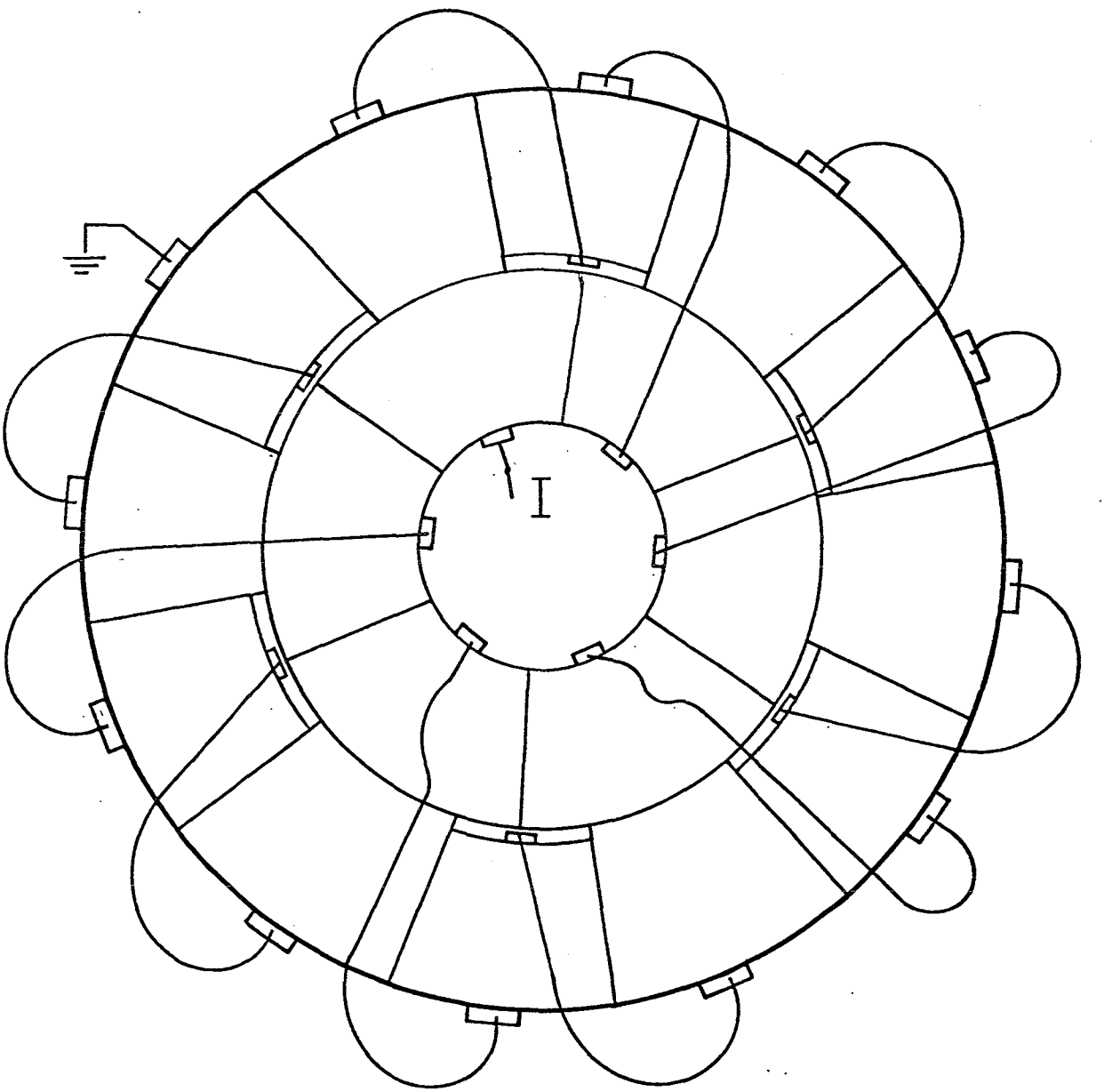

Figure 7.5 Current Sheet Chip Divided Into 18 Sections, Connected in Series by Wire Bonding.

In memory operation the current in the stripe propagation sheets is shut off when the I/O strip is used for inserting or removing a row of bubbles. If this chip is used as a data recorder for a satellite, there will be 1150 pulses on the I/O strip for every pulse on the stripe propagation sheets. Thus the average power from the stripe propagators in this situation is 2.5×10^{-5} watts, which is negligable.

7.3.5 Alternative Stripe Propagator

Figure 7.6 shows a current sheet in which the average current flow is circumferential rather than radial. This allows selection of just one track if one should want to do that. This configuration appears less attractive than that of figure 7.2.

7.3.6 Input/Output Tracks

There are many possible choices for I/O track designs. One choice is shown in figure 7.7. This track must be electrically separate from the stripe propagate sheets since the current for propagation is in the same direction for both. This can be done by having the I/O tracks in different layers than the stripe propagators, or by placing the I/O strip in a gap in the stripe propagation sheet as shown in figure 7.7. Here we rely on the repulsive force of the stripes to get domains past the gap.

Figure 7.8 shows another choice. Here the stripe propagation sheet is electrically connected to the I/O track. Bubbles will only propagate in that I/O track if the pulse pattern is a positive pulse 1+ in layer 1, then a negative pulse 1- in layer one, then a positive pulse 2+ in layer 2, then a negative 2- in layer 2. Stripes will not propagate with that pattern. To propagate stripes the pattern must be 1+, 2+, 1-, 2-. This pattern will not propagate bubbles on the I/O strip.

Figure 7.9 shows apertures that will propagate bubbles either vertically or horizontally depending on whether the current is horizontal or vertical. When that track is inserted into a stripe propagation sheet, the result is shown in figure 7.10. For stripe propagation the current is radial. For I/O, the applied current must be circumferential.

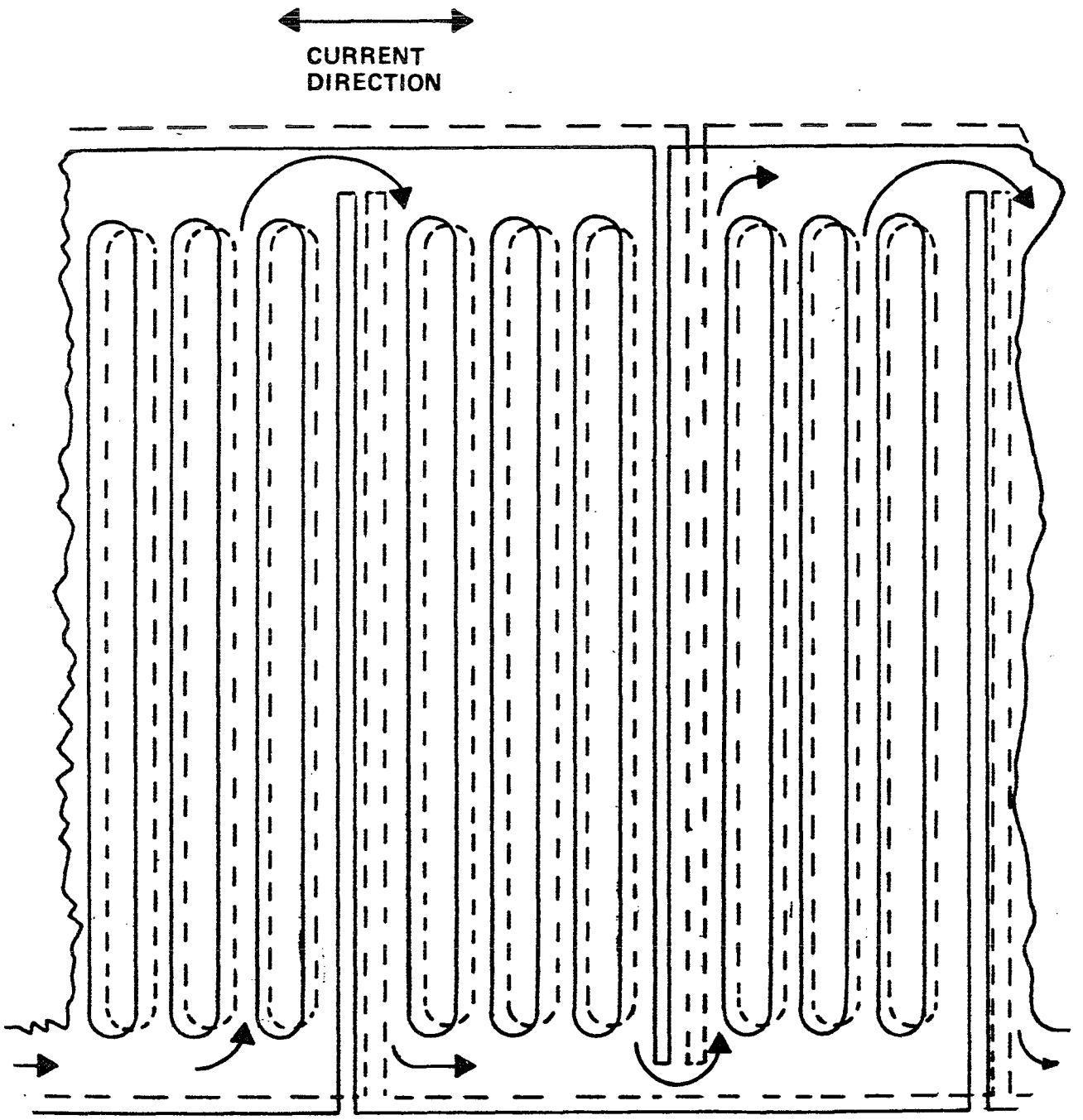

Figure 7.6 Slotted Stripe Domain Propagator in Which the Current Flows Along the Bubble Track.

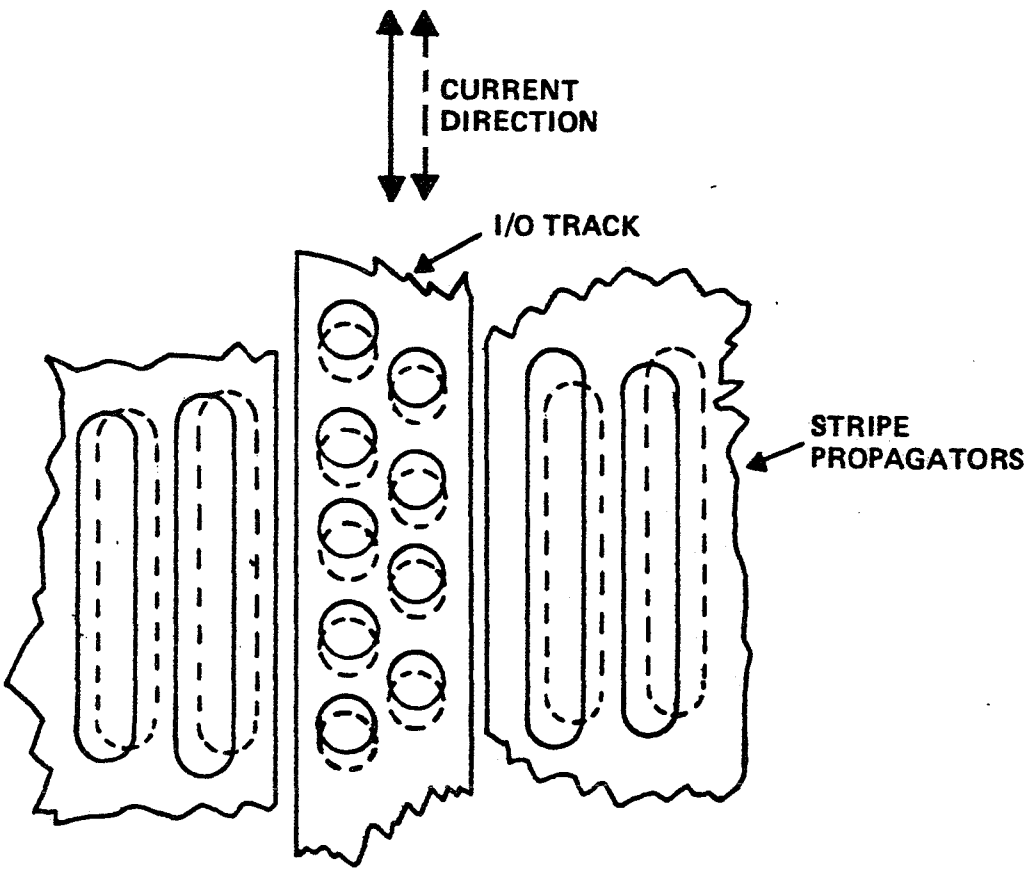

Figure 7.7 Current Sheet for an Input/Output Data Track. The Current is Parallel to the Bubble Motion.

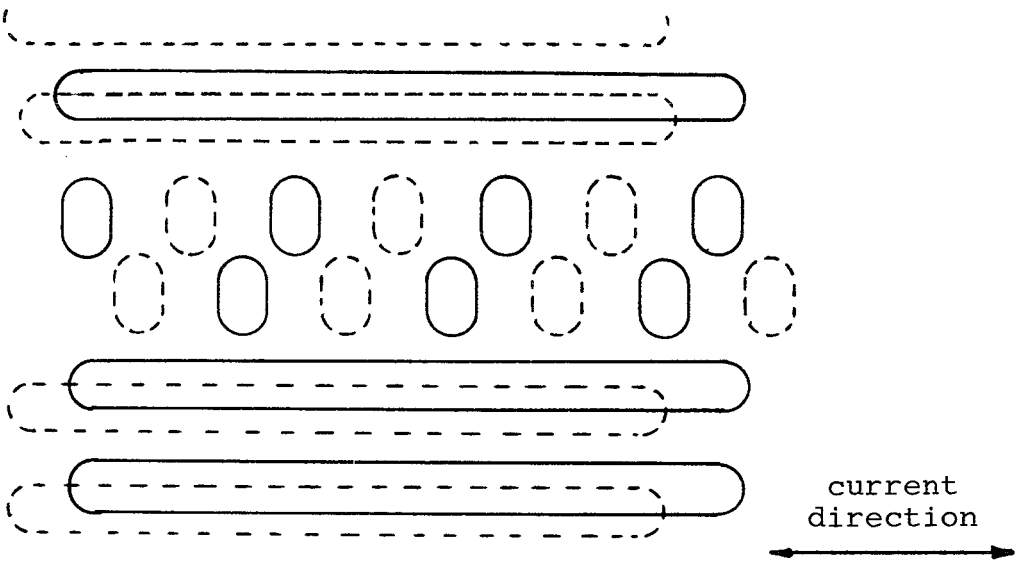

Figure 7.8 Stripe Propagators and Bubble Input/Output Track. For Stripe Propagation, the Pulse Pattern is 1+, 2+, 1-, 2-. For I/O, 1+, 1-, 2+, 2-.

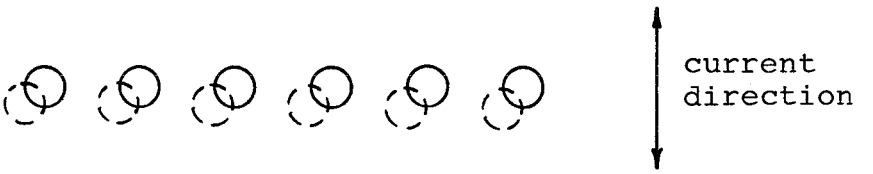

Figure 7.9 Current Sheet Input/Output Data Track, with Current Perpendicular to the Bubble Motion.

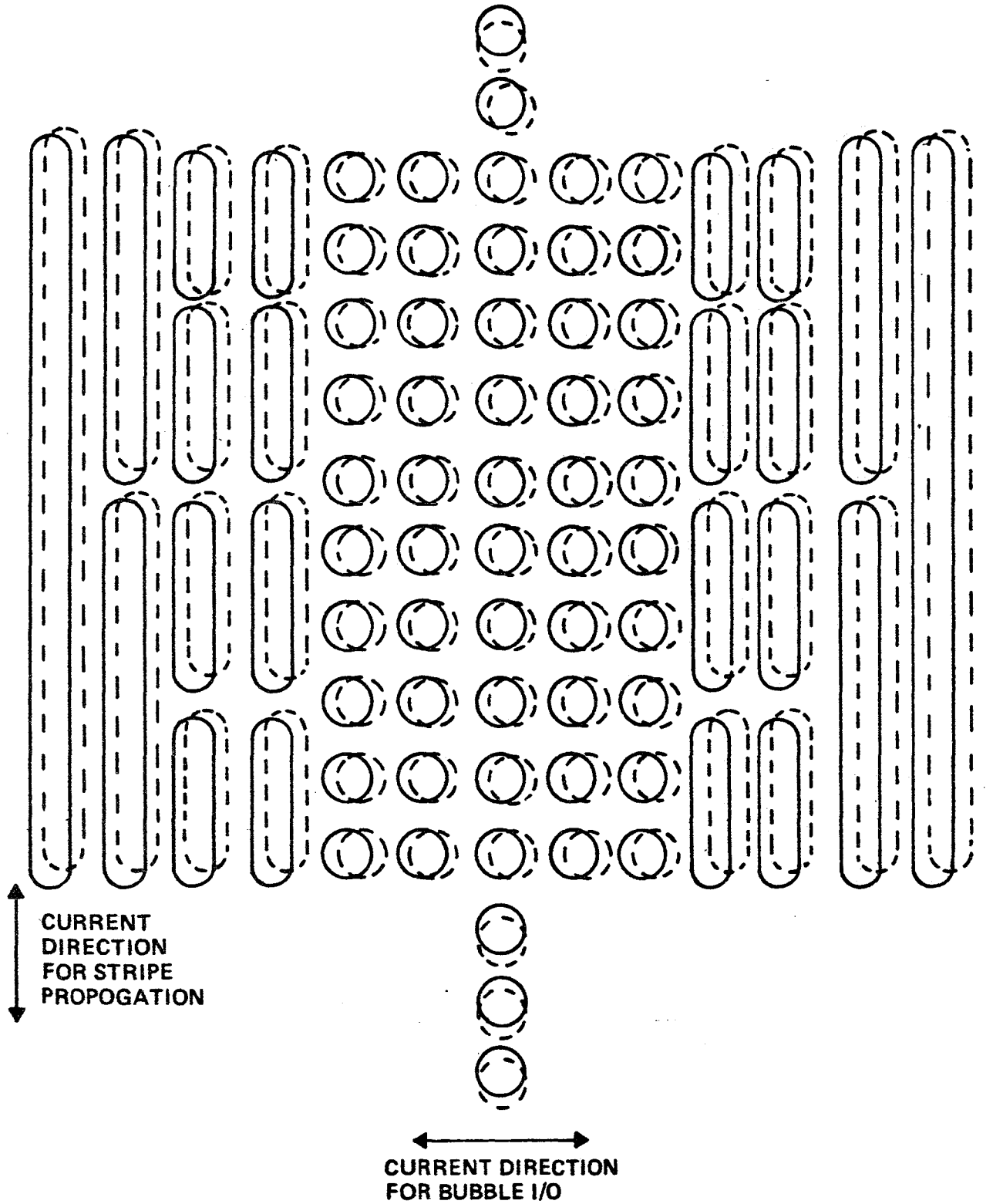

Figure 7.10 Stripe Domain Propagator with an Input/Output Track for a Row of Bubbles.

7.3.7 Advantages

There appear to be many advantages of this design over the present test vehicle design:

1) The concentric track current sheet design has fewer features, and the features are larger.

2) The current sheet stripe propagators of fig. 7.2 are "fail safe" with respect to random shorts or etch-outs. The stripe propagators of the present test vehicle are ruined by a single etch-out.

3) The current sheet propagators do not rely on permalloy features. These features make I/O difficult and a bad permalloy feature can trap a bubble.

4) The chip of fig. 7.3 requires few outside connections. Our present test vehicle has many.

5) The stripes do not curve or bow.

6) The coercivity does not have to be so very low in order to achieve stripe propagation.

7) The stripes do not have to be biased so very high. This means wider bias margins.

8) Stripe propagation can be must faster; viscous drag does not cause increased bowing and failure.

9) The pinning field can be lower. This will be helpful in getting bubbles past the pinning bar.

10) The closed loop geometry has much less waste space than straight track geometries.

11) No r.f. tickle field is required to reduce bowing.

12) No in-plane bias field coils are required.

13) A stripe array can be easily initialized with a single pulse. This is significant because initialization can be a problem with our present test vehicles.

14) A ground plane on top to reduce the normal field at the edges of the current sheets is not required.

At this writing it appears that a circular track current sheet design will solve the problems previously noted with the present test vehicle design. The next step should be experimental component evaluation.

8. Conclusions

As a result of the work performed under this contract, a multi-layer self-structured bubble memory appears to be very attractive. It has the advantages of higher data density and many fewer high resolution features than conventional bubble memories. Another advantage is current access, which saves weight and power, and is potentially much faster.

Of the large number of self structured configurations investigated, a three epi-layer configuration was found to be most advantageous. In this configuration, the layer next to the substrate contains data bubbles. The next layer is a non-magnetic G.G.G. spacer layer. The outer layer contains both stripe domains and carrier bubbles. The stripes are moved via current circuits at the stripe ends. The stripes move the carrier bubbles by magnetostatic repulsion. The carrier bubbles are magnetostatically coupled to data bubbles in the bottom layer.

A design was made of a memory with a single row of bubbles between stripes and having a density of 4×10^6 bits per square centimeter. The memory design has redundancy. All functions necessary to that memory have been demonstrated: Both the half lattice configuration (in which a single row of bubbles in the carrier layer exists between each pair of stripes in the carrier layer) and the full lattice configuration (in which multiple rows of bubbles exist between each pair of stripes) were demonstrated. These configurations, with both stripes and bubbles in the same magnetic layer were shown to be stable in the same bias field, provided that the stripe ends were pinned by permalloy features. It was demonstrated that the pinned stripes were stable even above the collapse field of the bubbles.

Current access stripe propagation was achieved by a variety of circuits. These were evaluated; the best was found to be a configuration in which the conductors are covered either with permalloy bars or chevrons. A curvature, or bowing of the propagating stripes was both calculated and measured as a function of bias field. The maximum track width is determined by that bowing, and for a typical film was found to be 1.5 mm. Propagation of bubbles was demonstrated by propagating stripes to which the bubbles were magnetostatically coupled. Triple epi-layer films were fabricated and found to have low defect density. Double bubbles and single bubbles were created in these films, using a current loop. The coupling between bubbles in different layers was both calculated and measured, as a function of applied bias field and thickness of the G.G.G. layer. This coupling was experimentally found to cause a difference in run-out threshold between double bubbles and single bubbles; this difference forms the basis of the readout method for detecting the presence or absence of a bubble in the buried data layer.

All the functions of the multilayer self structured memory have been demonstrated; however because of processing problems, the simultaneous operation of all functions on a single chip has not yet been demonstrated. This is planned for the next phase.

9. Acknowledgements

The authors wish to thank A.B. Smith and M. Kestigian of the Sperry Research Center in Sudbury, Mass. for their preparation of multi-layer epitaxial garnet materials, and S.J. Lins, R.H. Dean, R.J. Engfer, D.L. Fleming, W.A. Harvey, J.A. Krawczak, D.S. Lo, R.E. Lund, C.J. Nelson, G.L. Nelson, and D.E. Sutliff for their technical assistance.

REFERENCES

1. Y.S. Lin, J. Appl. Phys. 45, 4084 ('74).

2. H. Callen and R. M. Josephs, J. Appl. Phys. 42, 1977 ('71).

3. T. H. O'Dell, Magnetic Bubbles, Halsted Press, New York, 1974, p. 52.

4. H. Uchishiba, H. Tominaga, and K. Asama, IEEE Trans. Mag. 11, 1079 ('75).

5. C. Kooy, and U. Enz, Philips Research Reports 15 , 7 ('60).

6. T. H. O'Dell, op. cit., p. 35.

7. M. Kamin, J. A. Krawczak, S. J. Lins, E. J. Torok, and R. L. Stermer, J. Appl. Phys. 50, 2292 ('79).

8. E. H. L. J. Dekker, K.L.L. Van Mierloo, and R. DeWerdt, IEEE Trans. Mag. 13, 126 ('77).

9. E.H.L.J. Dekker, K.L.L. Van Mierloo, and R. DeWerdt, J. Appl. Phys. 49, 1927 ('78).

10. E.H.L.J. Dekker, N.J. Wiegman, K.L.L. Van Mierloo, and R. DeWerdt, J. Appl. Phys. 50, 2277 ('79).

11. M. Kestigian, A. B. Smith, and W. R. Bekebrede, Sperry Research Report SCRC-RP-77-79, ('77).

12. A. B. Smith, Sperry Research Report SCRC-74-21, ('74).

13. R. E. Lee, J. Vac. Sci. Technol. 16, 164 ('79).

14. T. W. Collins and R. W. Cole, IBM J. Res. Develop. 20, 132 ('76).

1. Report No.	2. Government Accession No.	3. Recipient's Catalog No.
NASA CR-165908		

4. Title and Subtitle	5. Report Date
Investigation of Multilayer Magnetic Domain Lattice File	August 1982
	6. Performing Organization Code

7. Author(s)	8. Performing Organization Report No.
E. J. Torok, M. Kamin, C. H. Tolman	
	10. Work Unit No.

9. Performing Organization Name and Address	11. Contract or Grant No.
Sperry Univac Corp. St. Paul, MN 55165	NAS1-15007
	13. Type of Report and Period Covered

12. Sponsoring Agency Name and Address	13. Type of Report and Period Covered
National Aeronautics and Space Administration Washington, DC 20546	Contractor Report
	14. Sponsoring Agency Code

15. Supplementary Notes

Langley Technical Monitor: Robert L. Stermer

16. Abstract

A theoretical and experimental investigation has determined that current accessed self structured bubble memory devices have the potential of meeting projected data density and speed requirements. Device concepts analyzed include multilayer ferrimagnetic devices where the top layer contains a domain structure which defines the data location and the second contains the data. Current aperture and permalloy assisted current propagation devices have been evaluated. Based on the result of this work more detailed device research has been initiated.

Detailed theoretical and experimental studies indicate that the difference in strip and threshold between a single bubble in the control layer and a double bubble which would exist in both the control layer and data layer is adequate to allow for detection of data. Detailed detector designs have been investigated.

17. Key Words (Suggested by Author(s))	18. Distribution Statement
Magnetic bubble memory Self structured Current access	Unclassified - Unlimited

19. Security Classif. (of this report)	20. Security Classif. (of this page)	21. No. of Pages	22. Price
Unclassified	Unclassified	160	A08

For sale by the National Technical Information Service, Springfield, Virginia 22161

End of Document